Philipps-Universität Marburg

Kumulative Dissertation

Development of a Short-Term Forecast System for Solar Surface Irradiance Based on Satellite Imagery and NWP Data

---

Zur Erlangung des Grades
Doktor der Naturwissenschaften
(Dr. rer. nat.)

im

Fachbereich Geographie
der Philipps-Universität Marburg

vorgelegt von
Isabel Urbich
aus Mainz

Marburg / Lahn, 2020

Vom Fachbereich Geographie der Philipps-Universität Marburg (Hochschulkennziffer 1180)
als Dissertation am 29.09.2020 angenommen.

Erstgutachter: Prof. Dr. Jörg Bendix
Zweitgutachter: Dr. Richard Müller

Tag der Disputation: 15.12.2020

Abstract

The increasing use of renewable energies as a source of electricity has lead to a fundamental transition of the power supply system. The integration of fluctuating weather-dependent energy sources into the grid already has a major impact on its load flows and associated with this economic effects. As a result, the interest in forecasting wind and solar radiation with a sufficient accuracy over short time periods (0–4 h) has grown. In this study, a novel approach for forecasting solar surface irradiance is developed which is based on the optical flow of the effective cloud albedo and SPECMAGIC NOW. This short-term forecast is combined seamlessly with the numerical weather prediction (NWP) to expand the forecast horizon up to 12 h. The optical flow method utilized here is TV-L^1 from the open source library OpenCV. This method uses a multi-scale approach to capture cloud motions on various spatial scales. After the clouds are displaced by extrapolating the optical flow into the future, the solar surface radiation will be calculated with SPECMAGIC NOW, which computes the global irradiation spectrally resolved from satellite imagery. Due to the high temporal and spatial resolution of satellite measurements, the effective cloud albedo and thus solar radiation can be forecasted from 15 min up to 4 h with a resolution of 0.05°. The combination of the displacement of clouds by TV-L^1 and the calculation of solar surface irradiance by SPECMAGIC NOW is innovative and promising. Finally, a procedure for a seamless blending between a NWP model and the presented nowcasting is developed. For this purpose the software tool ANAKLIM++ is utilized which was originally designed for the efficient assimilation of two-dimensional data sets using variational approach. ANAKLIM++ blends the nowcasting, ICON and IFS between 1–5 h in such a way that the combined forecast delivers a smaller forecast error than the individual forecasts for each lead time.

Kurzfassung

Die zunehmende Verwendung erneuerbarer Energien als Stromquelle hat zu einem fundamentalem Wandel des Energieversorgungssystems geführt. Die Integration fluktuierender wetterabhängiger Energiequellen in das Stromnetz hat bereits jetzt einen massiven Einfluss auf sämtliche Lastflüsse und damit einhergehend wirtschaftliche Auswirkungen. Infolgedessen ist das Interesse nach Vorhersagen des Windes- und der solaren Einstrahlung mit einer hohen Genauigkeit auf kurzen Zeithorizonten (0–4 h) gestiegen. In dieser Arbeit wird ein neuer Ansatz für die Vorhersage der solaren Einstrahlung am Boden entwickelt, welcher auf dem optischen Fluss der effektiven Wolkenalbedo und SPECMAGIC NOW basiert. Diese Kürzestfristvorhersage wird nahtlos mit der numerischen Wettervorhersage (NWV) verbunden, um den Vorhersagehorizont auf bis zu 12 h zu erweitern. Die hier verwendete Methode für die Berechnung des optischen Flusses ist TV-L^1 aus der Open-Source-Bibliothek OpenCV. Diese Methode verwendet einen Multi-Skalen-Ansatz zur Erfassung von Wolkenbewegungen auf verschiedenen räumlichen Skalen. Nachdem die Wolken durch Extrapolation des optischen Flusses in die Zukunft verlagert wurden, wird die solare Strahlung mit SPECMAGIC NOW berechnet. Dieser Algorithmus errechnet die globale Einstrahlung spektral aufgelöst aus Satellitenbildern. Aufgrund der hohen zeitlichen und räumlichen Auflösung von Satellitenmessungen kann die effektive Wolkenalbedo, und damit auch die solare Einstrahlung, von 15 min bis zu 4 h mit einer Auflösung von 0,05° vorhergesagt werden. Die Kombination der Wolkenverlagerung durch TV-L^1 und der Strahlungsberechnung durch SPECMAGIC NOW ist neuartig und sehr vielversprechend. Schließlich wird ein Verfahren für einen bruchlosen Übergang zwischen einem NWV Modell und dem vorgestellten Nowcasting entwickelt. Dazu wird das Softwaretool ANAKLIM++ verwendet, welches ursprünglich für die effiziente Assimilation von zweidimensionalen Datensätzen unter Verwendung eines Variationsansatzes konzipiert wurde. Mit ANAKLIM++ werden das Nowcasting, ICON und IFS für einen Vorhersagehorizont zwischen 1–5 h derart miteinander verbunden, dass die kombinierte Prognose für jede Vorhersagezeit einen kleineren Vorhersagefehler besitzt, als die Einzelprognosen vor der Kombination.

Contents

List of Figures

List of Tables

List of Abbreviations

AMV	Atmospheric Motion Vector
ANAKLIM++	Adjustment of assimilation software for the reanalysis of climate data
BMWi	Bundesministerium für Wirtschaft und Energie (Federal Ministry for Economic Affairs and Energy)
BSRN	Baseline Surface Radiation Network
CAL	Effective Cloud Albedo
Cb-TRAM	Tracking and monitoring severe convection from onset over rapid development to mature phase using multi-channel Meteosat-8 SEVIRI data
CERES	Clouds and the Earth's Radiant Energy System
CM SAF	Climate Monitoring Satellite Application Facility
CMV	Cloud Motion Vector
COSMO	Consortium for Small Scale Modeling
DNI	Direct Normal Irradiance
DSO	Distribution System Operator
DWD	Deutscher Wetterdienst (German Weather Service)
ECMWF	European Centre for Medium-Range Weather Forecasts
EUMETSAT	European Organization for the Exploitation of Meteorological Satellites
FAR	False Alarm Rate
Fraunhofer IEE	Fraunhofer Institute for Energy Economics and Energy System Technology
GHI	Global Horizontal Irradiance
HRV	High Resolution Visible
HSV	Hue Saturation Value
ICON	Icosahedral Non-Hydrostatic Model
IFS	Integrated Forecasting System
IPCC	Intergovernmental Panel on Climate Change
LUT	Hybrid Look-up Table
MACC	Monitoring Atmospheric Composition and Climate Project
MAE	Mean Absolute Error
MFG	Meteosat First Generation

MSG	Meteosat Second Generation
Meteosat	Meteorological Satellite
MVIRI	Meteosat Visible and Infrared Imager
NDFD	National Digital Forecast Database
NN	Neural Networks
NWC SAF	Nowcasting Satellite Application Facility
NWP	Numerical Weather Prediction
NWV	Numerische Wettervorhersage
OpenCV	Open Source Computer Vision
POD	Probability of Detection
POLARA	Polarimetric Radar Algorithms
PV	Photovoltaic
RMSE	Root Mean Square Error
RTM	Radiative Transfer Model
SARAH-2	Surface Solar Radiation Data Set - Heliosat
SARB	Surface Atmospheric Radiation Budget
SEVIRI	Spinning Enhanced Visible and Infrared Imager
SESORA	Seamless Solar Radiation
SIS	Surface Incoming Shortwave Radiation
SPECMAGIC NOW	Spectrally Resolved Mesoscale Atmospheric Global Irradiance Code for Nowcasting
TSO	Transmission System Operator
TV-L^1	Method based on Total Variation in Regularization Term and L^1-Norm in Data Fidelity Term
WRF	Weather Research and Forecasting
WRMC	World Radiation Monitoring Center

Chapter 1

Introduction

1.1 Motivation

The German grid is currently under a fundamental transition. Sources for electricity generation are changing towards more sustainable alternatives and the overall interest for renewable energies is growing. Not only in Germany but world wide, renewables rank among the fastest-growing sources for electricity generation (EIA, 2019). In 2019, 40% of Germany's entire electricity was already generated by renewable energy sources, mostly by solar power, wind and biomass (AGEB, 2020). An illustration of the development of the fraction of renewable energy sources in Germany is displayed in Figure 1.1.

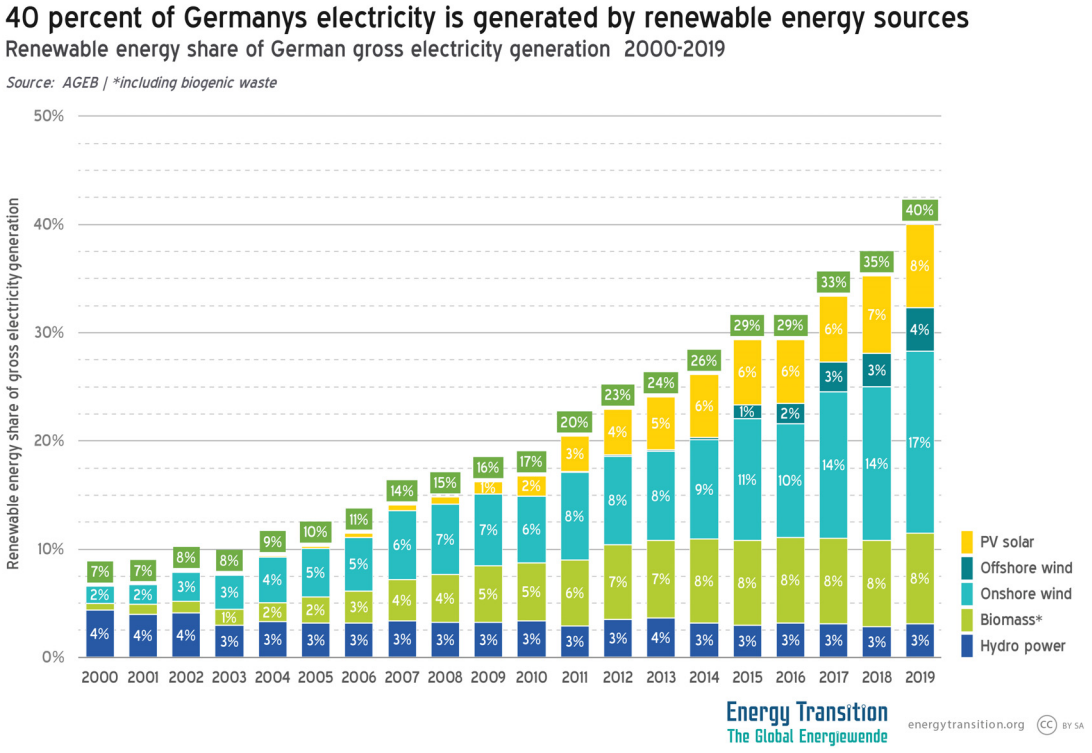

Figure 1.1: Share of renewable energies in Germany from 2000–2019 (Energy Transition, 2019).

Fighting climate change is only one of many reasons supporting the energy transition in Germany. The Intergovernmental Panel on Climate Change (IPCC) warned repeatedly in its latest assessment report about the fatal consequences of climate change (Pachauri et al., 2014). By using renewable energies as source of electricity, decarbonization will continue and the air pollution by coal plants can be further reduced (Energy Transition, 2019).

Currently, Germany imports about two third of its total energy including gas, oil, uranium and hard coal. In 2016, 76,000 Mio EUR were spent on energy imports in Germany which is around 7% of its expenses for imports in general. A transition to renewable energies would reduce German's dependency on energy imports which would make it less vulnerable to unpredictably fluctuating prices. Thus, by reducing energy imports the energy security in Germany could be increased and the political influence on the energy supply could be decreased. Hence, using renewable energies and improved energy conservation can reduce the dependency of countries that consume energy on countries that provide energy sources globally (Energy Transition, 2019).

Renewable energies are a save alternative to nuclear power. In Germany, nuclear phaseout is decided for 2022 and several nuclear power plants were already shut down because the risk of a nuclear disaster is by far too high (IAEA, 2020). Nuclear power is currently unbankable which means that banks will not finance the construction of new nuclear power plants. Thus, the costs of the maintenance of nuclear power plants are much higher than those of wind parks and solar power plants. Moreover, there is only a limited availability of uranium resources. Therefore, an alternative energy source is essential and political dependencies on account of energy imports should be averted. On top of that, there still exists an unsolved issue for nuclear waste. The risk of radiation from the storage of nuclear waste will not only affect us but it will be passed on to future generations (Energy Transition, 2019).

Due to the fluctuating and weather-dependent character of renewable energies the integration of photovoltaic power plants and wind parks into the grid is more challenging than that of conservative power plants. In an electrical power supply system, generation and consumption always need to be balanced (Bundesnetzagentur, 2020). Currently, only minimal amounts of energy can be accumulated by means of energy conversion. Smaller deviations between production and consumption can affect grid frequency or voltage. However, higher deviations could lead to large-scale blackouts. These variations have to be compensated by the use of an operating reserve to maintain a frequency of 50 Hz and hence grid stability. Further, system operators can instruct specific power plants to change their power output if the current load in a specific line of the grid is too high. These interventions by system operators are called redispatches and refer to measures in the generation capacity of power plants to protect sections of the grid from overloading. Due to the integration of renewable energies into the power supply system and the phaseout of nuclear power redispatch interventions have become a lot more frequent over the last decades (Bundesnetzagentur, 2020). Moreover, this integration led to an increased requirement of balancing power due to the fluctuation nature of wind and solar radiation. In 2006, these balancing costs together with the transaction costs amounted

to an additional 300–600 Mio EUR in Germany (Dürrschmidt and van Mark, 2007). Responsible for these higher costs in comparison to conventional plants are among others the errors of weather and power forecasts. Nevertheless, these costs can be decreased by the reduction of the respective forecast errors (Lenzi et al., 2013). Further, the current development of the power grid is a revolution regarding its structure. In addition to a small number of large, central power plants there are numerous, small private plants like PV (photovoltaic) systems on roof tops. Thus, power production and consumption are not one-way-streets anymore.

The work of system operators is challenging and highly dependent on accurate forecasts of weather and power. Especially with regard to the increasing share of renewable energies as a source of electricity, the need for better forecasts is growing. For this purpose, the German Weather Service (Deutscher Wetterdienst, DWD) and the Fraunhofer Institute for Energy Economics and Energy System Technology (IEE) cooperate in a research project funded by the Federal Ministry for Economic Affairs and Energy (Bundesministerium für Wirtschaft und Energie, BMWi) which is called Gridcast. The aim of this project is the development of new methods to improve the determination of the actual and the expected wind and PV power feed-in over the next few hours or days at any substation of the German grid (Gridcast, 2020).

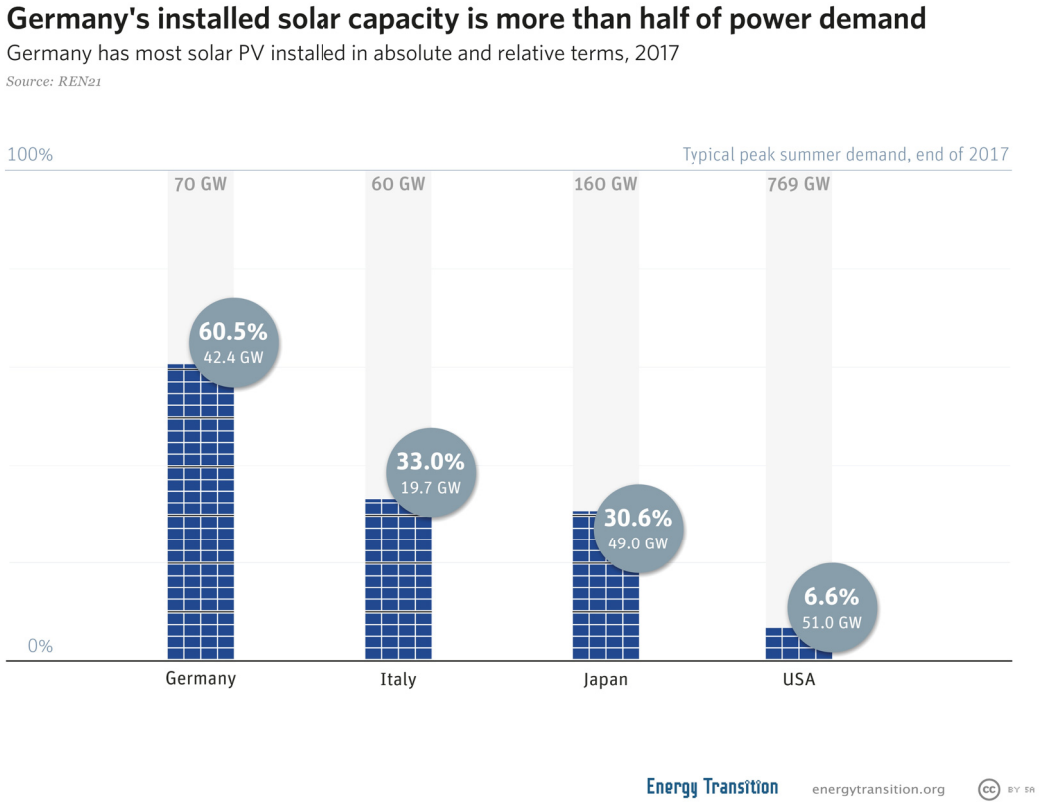

Figure 1.2: Installed solar capacity in Germany in comparison with Italy, Japan and USA in 2017 (Energy Transition, 2019).

In the last couple of years, the share of renewable energies for the generation of electricity grew continuously as well as the share of PV power itself (Figure 1.1). In 2017, the installed solar capacity of Germany covered more than half of the power demand on a typical summer day. This is more than Italy, Japan and the USA could cover although Japan and the USA have more installed solar capacity in absolute numbers (Figure 1.2). In this context it is important to indicate that the installed capacity is the intended full-load output of a power plant (Bundesnetzagentur, 2020). The actually generated power is usually lower e.g. due to nights and clouds in the case of photovoltaic plants. Considering this development, the need for more accurate forecasts of solar surface irradiance (SIS) is growing rapidly. System operators need a reliable and accurate forecast of solar power and solar surface irradiance for the next few hours up to the next day since the controlled shutdown of power plants requires a couple of hours. The most accurate forecast for the first few hours delivers the so called nowcasting. It is a short-term forecast based on satellite observations and the calculation of their inherent optical flow. Due to fast error growth nowcasting is usually the best choice up to 2–4 h depending on the weather situation. For longer forecast horizons numerical weather prediction (NWP) models deliver the best forecast results however not for the first few hours. This is a result of a coarser spatial and temporal resolution and limitations in the model physics induced by the chaotic and non-linear nature of weather. Eventually, the needs of distribution and transmission system operators can be fulfilled by merging nowcasting and numerical weather prediction models. The result of such a combination is a reliable, seamless near real-time prediction of solar surface irradiance for 0–12 h and beyond.

1.2 State of Research

In this study a novel approach for a nowcasting and a seamless prediction of solar surface irradiance is presented. In the following, the current state of research concerning methods for the prediction of SIS will be discussed.

Several studies have been published wherein neural networks (NN) were used for the detection of cloud motion vectors (CMV) in order to predict cloudiness (Nikitidou et al., 2019). However, the approach is a lot more common for the short-term forecast of SIS regarding its application for PV predictions (Aliberti et al., 2018; Voyant et al., 2017). NN are also widely used for seamless predictions of either solar irradiance (Mellit and Pavan, 2010; Marquez et al., 2013; Bosch et al., 2008) or PV power (Wolff et al., 2016). Due to a black-box-character of NN, a deeper understanding of the physics and physical reasons of the uncertainties occurring is difficult. Moreover, validation results reported in recent reviews by Antonanzas et al. (2016) or Barbieri et al. (2017) do not provide any hints that neural networks lead to significantly more accurate cloud motion vectors. Besides, neural networks are strictly speaking only valid for their training and validation periods and regions. Currently, an application to other regions, periods or satellite instruments requires extensive re-training. Other proposed methods for the development of a short-term forecast are cross-correlation methods (Schmetz et al., 1993) or gradient methods (Pereda, 2016). However, these methods lead to a low density of cloud motion vectors. Therefore, both methods are not appropriate for the usage in energy meteorology since

a high temporal and spatial resolution without data gaps is crucial. Another successful method is the use of a semi-Lagrangian scheme to calculate the advection of a flow (Turner et al., 2004; Lin et al., 2005; Berenguer et al., 2011). For this, the vectors for Lagrangian trajectories are iteratively determined for each time step to allow rotation of a flow (Germann and Zawadzki, 2002). This method only has an advantage over optical flow methods in small-scale rotations. Further, respective differences are small at the beginning of the forecast and grow with increasing lead time. Since a blending is performed after 1 h these differences will not have an impact on the accuracy of nowcasting. So far optical flow methods are hardly used in the scope of meteorology. An overview over different optical flow methods was given by Sonka et al. (2014). One of the first applications has been the utilization of the optical flow for radar images as described by Peura and Hohti (2004). Further studies presented cloud tracking methods with either geostationary satellites (Hammer et al., 2003; Hamill and Nehrkorn, 1993; Lorenz et al., 2004), total sky imagery (Cheng, 2017), or ground sensors (Bosch et al., 2013). Other authors successfully used cloud motion vectors for applications beyond the scope of energy meteorology like Guillot et al. (2012) for cloud tracking over complex terrain and Velden et al. (1998) for tracking tropical cyclones. There exist a couple of other studies in which cloud motion vectors are utilized for solar irradiance forecasts (Sirch et al., 2017; Gallucci et al., 2018; Nonnenmacher and Coimbra, 2014; Schroedter-Homscheidt and Gesell, 2016). However, they do not use the optical flow method TV-L^1 which is applied in this thesis. Yet, these studies will be used as benchmark for the results of this thesis. According to the knowledge of the author of this thesis, there is one publication within the scope of satellite-based solar irradiance forecasts in which a multiple-scale optical flow method is applied (Sirch et al., 2017). The utilized method was developed within the storm detection and nowcasting system Cb-TRAM (Tracking and monitoring severe convection from onset over rapid development to mature phase using multi-channel) (Zinner et al., 2008, 2013). However, due to a brief description and no further access to the software, the scientific benefit of this work is limited. Furthermore, the authors applied the CMV onto optical thickness and effective radius which is a lot more prone to uncertainties than the retrieval of the effective cloud albedo.

There are numerous approaches for seamless forecasts of SIS like fuzzy models (Boata and Gravila, 2012), adaptive neuro-fuzzy interference systems (Moghaddamnia et al., 2009), autoregressive models (Dambreville et al., 2014; Bacher et al., 2009), multiplicative autoregressive moving-average statistical models (Mora-Lopez and Sidrach-de Cardona, 1998), hidden Markov processes (Hocaoğlu, 2011), multi-dimensional linear predictions filters (Akarslan et al., 2014), multi-model-mix of diverse forecasting approaches (Sanfilippo et al., 2016), and using the Weather Research and Forecasting (WRF) model to advect and diffuse Meteosat Second Generation (MSG) cloud index values (Arbizu-Barrena et al., 2017), just to name a few. Another commonly used method for seamless prediction is a linear regression. Lorenz et al. (2012) and Kühnert (2016) presented two very similar methods for solar irradiance and PV power where they performed a linear regression of the COSMO (Consortium for Small Scale Modeling) from the DWD, IFS (Integrated Forecasting System) from the ECMWF (European Centre for Medium-Range Weather Forecasts) and a nowcasting (Baldauf et al., 2018; ECMWF, 2019). Furthermore, Haupt et al. (2016) worked on a blending system which performs a bias correction of the used

models in a first step. After that, the developed system optimizes the weights for the blending for each lead time in respect of their historical performance. With an optimum conglomeration of several observation-based forecasts and NWP models, Perez et al. (2014) presented an approach where the forecast performance determines the weights for the blending as well.

The forecast system developed within the scope of this thesis combines cloud motion vectors derived from the effective cloud albedo (CAL), a calculation of SIS by SPECMAGIC NOW (Spectrally Resolved Mesoscale Atmospheric Global Irradiance Code) and a blending method called ANAKLIM++ (Adjustment of Assimilation Software for the Reanalysis of Climate Data) (Müller et al., 2012; Groß et al., 2014a). For the derivation of CMV the optical flow between two consecutive images of CAL is estimated by the method TV-L^1 from the open source library OpenCV (Open Source Computer Vision) (OpenCV, 2020). It is particularly suited for the application in the scope of meteorology since it uses a multi-scale approach and is therefore able to capture cloud motions on various spatial scales. After the displacement of clouds, SIS is calculated by SPECMAGIC NOW which computes global irradiation spectrally resolved from satellite imagery. In order to obtain a seamless forecast of SIS a blending of the developed nowcasting and two NWP models is performed. For this purpose, a software tool called ANAKLIM++ is utilized which uses methods from data assimilation to merge two-dimensional data sets and fill data gaps in satellite measurements. ANAKLIM++ provides the option to give each data set global and regional weights whereby the consistency of the merged product is ensured by a variational approach and the constraint of mass conservation. Therefore, ANAKLIM++ is assumed to be a rather useful tool for a blending of nowcasting and NWP. In this thesis, ANAKLIM++ is utilized, optimized and evaluated for the first time in the scope of the seamless prediction of solar surface irradiance.

1.3 Aim

The aim of this thesis is the development of a seamless forecast system of solar surface irradiance for 0–12 h. This time period is crucial for transmission and distribution system operators to balance the power supply and act on potential grid instabilities. Besides, more accurate weather forecasts lead to smaller forecast errors and therefore to less balancing costs. However, for this time period there exist two different forecast approaches, numerical weather prediction and nowcasting, which differ in horizontal and temporal resolution, area of interest and as a consequence they also differ in the resulting prediction. Usually, for the first few hours an observation-based nowcasting is used because the forecast is available near real-time and it is temporally and spatially high resolved. Since these predictions are only based on cloud motion vectors and run without any physical simulations their error growth rate is rather high. Therefore, numerical weather prediction is used after a few hours. However, their spatial and temporal resolution is lower than those of the nowcasting owing to a very high complexity of these models and limited computing capacity. Both forecast products have their weaknesses and do not fulfill the needs of a system operator individually. However, combined they can overcome each other's shortcomings and complement positively in a seamless prediction system and

provide better forecasts for a longer time period. For this reasons, a seamless forecast for solar surface irradiance has to be developed which combines the advantages of a high resolved, near real-time forecast with an extensive and reliable numerical weather prediction model.

In the process of developing a seamless forecast system there appear a list of research questions (Q) like:

- **Q1** How can satellite imagery be used for a forecast of solar surface irradiance?
- **Q2** How well performs an observation-based nowcasting of SIS?
- **Q3** After which forecast time does NWP deliver better results than nowcasting?
- **Q4** How can nowcasting and numerical weather prediction be combined?

By answering these questions this thesis will contribute to a development of a novel forecast approach of solar surface irradiance using satellite imagery and NWP data. Moreover, this work will improve the understanding of physical processes in the atmosphere regarding solar irradiance and its prediction. A seamless forecast system like the one presented in this thesis will simplify the work of transmission and distribution operators as well as direct marketers.

1.4 Outline

A scheme of the structure and outline of this thesis is depicted in Figure 1.3. This scheme visualizes the temporal and textual procedure of the work packages of this thesis. They are built upon the results of the previous work package which is depicted by arrows in the scheme. Thus, the order of the following chapters is adapted from the process of the development of the resulting forecast system.

The aim of this thesis is to develop a seamless forecast system for solar surface irradiance. For this purpose, a short-term forecast has to be designed first which is based on satellite imagery from MSG. Work package 1 (WP), which is further described in chapter 3, covers the development of this observation-based short-term forecast, also known as nowcasting, of the effective cloud albedo. The optical flow of CAL is being estimated by calculating cloud motion vectors between two consecutive satellite images. The resulting cloud motion vectors are thereafter applied to the latter of these images to extrapolate the cloud motion into the future. In order to evaluate the morst appropriate optical flow method for the estimation of cloud motion vectors based on CAL two established methods, namely TV-L^1 and Farnebäck (Zach et al., 2007; Farnebäck, 2003), are implemented and their results are compared to each other. Both algorithms come with a set of parameters that needs to be adjusted and optimized for the specific utilization of CAL because both have not been used for this purpose so far. This step was needed to gain the optimal accuracy for the nowcasting of the effective cloud albedo and has therefore been an essential issue of this study. Finally, these two optimized optical flow methods

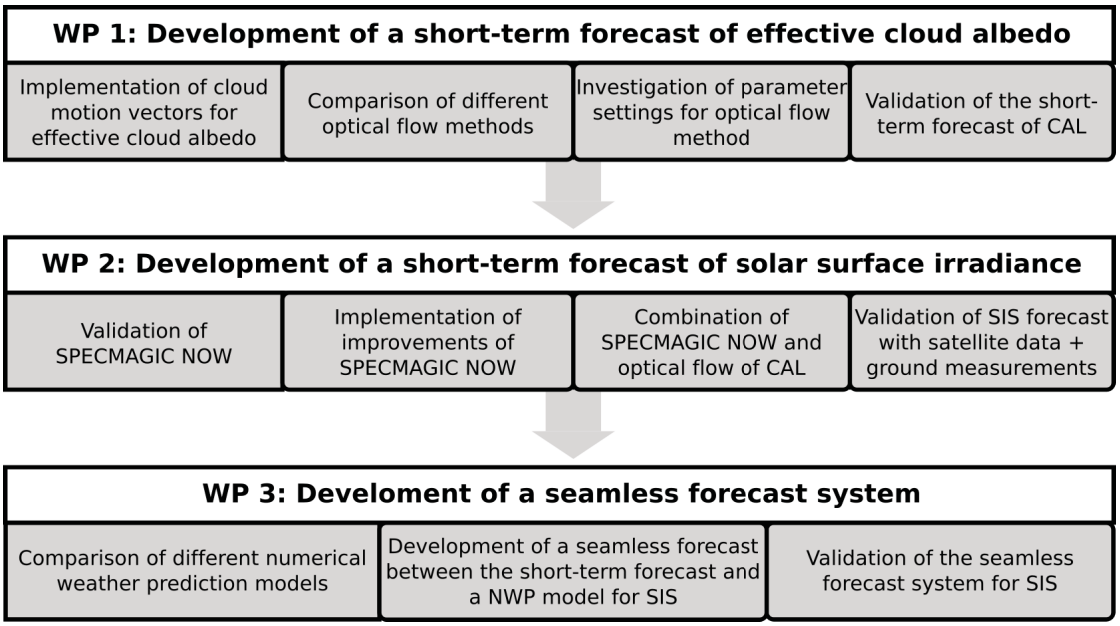

Figure 1.3: Scheme of the outline of this thesis.

are extensively validated by computing the absolute difference between the measured effective cloud albedo and the corresponding short-term forecast for each pixel of the satellite image. Additionally, the bias, mean absolute bias and RMSE (root mean square error) are calculated for a list of cases with different weather situations in the months of August, September and October 2017.

Work package 2, which is covered in chapter 4, deals with the development of a short-term forecast of solar surface irradiance, hence the current nowcasting of the effective cloud albedo is being extended. For this purpose, the software SPECMAGIC NOW by Müller et al. (2012) which computes global radiation spectrally resolved from satellite imagery is used. At first, the existing algorithm is evaluated by means of SARAH-2 (Surface Solar Radiation Data Set - Heliosat) data (Pfeifroth et al., 2017). Since SPECMAGIC NOW has been modified for the utilization in a nowcasting a first analyzation of errors is crucial. Later, improvements are implemented and the updated version of SPECMAGIC NOW is combined with the algorithm of the optical flow estimation of WP 1. Thus, the merged algorithm takes two consecutive satellite images and computes the cloud motion vectors which describe the motion of clouds in the corresponding time period. The resulting vectors are applied to the latter of the satellite images as often as desired for the nowcasting. All resulting CAL data arrays resulting from the optical flow estimation are utilized to compute solar surface irradiance with SPECMAGIC NOW. An extensive validation of the short-term forecast of solar surface irradiance is performed for the list of cases from WP 1 using satellite-derived data and pyranometer measurements. Further, the bias, MAE (mean absolute error) and RMSE are determined and a linear regression is done. By specifying a threshold for CAL, the validation can be separated into cloud and clear sky results. That way, the elements of the contingency table can be analyzed and plotted on a map. By doing this, the validation can reveal error sources due to

wrong advection or overestimation of solar radiation. All results are also normalized by the mean solar irradiance to obtain relative error measures additionally. Moreover, WP 2 addresses the answers to research questions **Q1** and **Q2**.

Chapter 5 describes the results of work package 3 which deals with the final development of a seamless forecast system for solar surface irradiance. The SIS nowcasting that was topic of the first two work packages and two NWP models are combined to obtain a seamless forecast for 0–12 h. In a first step, two NWP models are compared using the same error measures that where mentioned in WP 1 and WP 2 to evaluate their quality in dependency of their lead time and day time. The error measures for all forecast approaches are calculated in reference to analysis data from SARAH-2. Several studies have already shown that observation-based short-term forecasts perform better for the first few hours of forecast while NWP models deliver better results after approximately 2–4 h (Lorenz et al., 2012; Wolff et al., 2016; Kilambi and Zawadzki, 2005; Perez et al., 2010; Nonnenmacher and Coimbra, 2014). However, the point of intersection depends on the weather situation and the chosen nowcastings method and NWP models. To evaluate this statement the nowcasting and the NWP models are contrasted for different weather situations. With the knowledge about the performance of each individual forecast an approach for a blending is designed using a software tool called ANAKLIM++. It was originally developed for the assimilation of satellite images and other two-dimensional data sets to obtain a product without data gaps. In order to make use of this special feature some intentional gaps are made by cutting out areas of potential error growth in the nowcasting. These data gaps can be filled with NWP data by using ANAKLIM++. The blending with ANAKLIM++ is performed for 1–5 h of forecast time using ICON (Icosahedral Non-Hydrostatic Model) (Reinert et al., 2018), IFS and the nowcasting of solar surface irradiance. The resulting blending and the input data sets are validated with SARAH-2 data and the already mentioned error measures bias, MAE and RMSE are determined. For comparison, a simple blending approach with a linear transition is presented and validated as well. The answers to the research questions **Q3** and **Q4** are given in WP 3.

The results of the mentioned work packages can be found in the corresponding chapters and a summary of the most important results and a conclusion will follow in chapter 6.

Chapter 2

Data

In the following chapter, an overview over the data sets which are used for this thesis is given and a list of the data sets can be found in Table 2.1.

Var	Data Set	Operator	Type	Horizontal Resolution	Temporal Resolution
CAL	SPECMAGIC NOW	DWD	Sat-derived Analysis	5 km	15 min
SIS	SARAH-2	CM SAF	Sat-derived Analysis	5 km	30 min
SIS	Nowcasting	DWD	Short-term Forecast	5 km	15 min
SIS	Pyranometer	DWD	Measurement	–	1 min
SIS	Pyranometer	BSRN	Measurement	–	1 min
SIS	ICON	DWD	NWP	13 km	1 h
SIS	IFS	ECMWF	NWP	9 km	1 h

Table 2.1: Overview over the data sets which are used in this thesis. For further information the reader may refer to section 3.2.2, section 4.2 and section 5.2.

As already mentioned in chapter 1, the overall importance for high quality forecasts of solar surface irradiance is still increasing. For a spatially and temporally high resolved short-term forecast of solar surface irradiance satellite-derived data is the first choice. Utilizing the effective cloud albedo derived from MSG for the optical flow estimation has many advantages like the linear relation to solar surface irradiance for values up to 0.8. Besides that, CAL can be directly observed from space without the need of an additional model and the reflection of the earth's surface is already filtered. The effective cloud albedo is a product of SPECMAGIC NOW (Müller et al., 2012). The area covered by MSG expands from -80° to +80° in latitude and longitude with a horizontal resolution of approximately 5 km for central Europe and a temporal resolution of 15 min.

After the extrapolation of the cloud movement into the future to obtain an effective cloud albedo nowcasting, SPECMAGIC NOW is used for the calculation of solar surface irradiance. Thus, the nowcasting is also available every 15 min with a resolution of 5 km. The nowcasting of SIS is being validated with satellite-derived data from the Climate Monitoring Satellite Application Facility (CM SAF) and additionally with stationary measurements by the Baseline Surface Radiation Network (BSRN) and the DWD (BSRN, 2020). SARAH-2 is the latest CM SAF climate data record of solar surface irradiance based on the Meteosat satellite series (Pfeifroth et al., 2017). This data set is available

every 30 min with a horizontal resolution of 5 km for the area from -65° to +65° in latitude and longitude. SARAH-2 is a reasonable choice as reference data since its quality is well documented by Pfeifroth et al. (2017). It was found a positive bias of 2 W/m^2 and the absolute bias equals 5 W/m^2 for the monthly mean SARAH-2 data.

Further validation was performed with ground station measurements of pyranometers. For this purpose, the stations from the DWD were used due to their large occurrence. Additionally, the measurements from the BSRN were utilized because of their high accuracy. All the data from the pyranometer from the BSRN are controlled twice, once at the stations and once at the World Radiation Monitoring Center (WRMC) (Ohmura et al., 1998). There were used 4 stations from the BSRN thereof 2 in France, 1 in the Netherlands and 1 in Spain. Their high quality is reflected in a low standard deviation of 5 W/m^2 for solar surface irradiance. From the DWD 34 stations were taken whereof all are located in Germany. The standard deviation of those pyranometers equals 3% of the respective total daily radiation. All pyranometer measurements have a temporal resolution of 1 min.

Eventually, a combination of the developed nowcasting and two NWP models is performed. For this purpose, the global and regional model ICON from the DWD is used. The horizontal grid consists of a set of spherical triangles that seamlessly span the entire globe (Reinert et al., 2018). Main runs are initialized four times a day at 00, 06, 12 and 18 UTC for the entire region up to 120 h and additional four times at 03, 09, 15 and 21 UTC with the EU (Europe) nest up to 30 h. The horizontal resolution of the grid of ICON (global) equals 13 km and the grid of ICON-EU equals 6.5 km. For this thesis only ICON global is used because the higher resolved ICON-EU did not lead to better validation results particularly in comparison to IFS (Arndt, 2019). Furthermore, for the sake of comparability the global version of ICON is used since the IFS is a global model too. From this point on, the term ICON stands for the global version of the ICON model, if not stated otherwise. The temporal resolution of solar surface irradiance is 1 h. However, the output of ICON is accumulated over several hours, depending on the initialization time of the run and given in W/m^2. For this thesis, these values are transformed into hourly averages.

The global model of the ECMWF is represented by the IFS. The main runs of the IFS come with a horizontal resolution of 9 km and are performed twice daily with initial times 00 and 12 UTC (ECMWF, 2019). Its temporal resolution is as well 1 h. The irradiance values are available as hourly accumulated values in J/m^2. For a forecast blending those values are being recalculated into hourly averages. In order to obtain hourly averages the accumulated values have to be divided by 3600 s which finally leads to a unit of W/m^2. For the nowcasting and the combination of those two NWP models only those model runs are used that would be available in an operational service hence the runtime was considered for the selection of the forecast. Thus, the 06 UTC run from ICON and the 00 UTC run from IFS are utilized for this study.

Chapter 3

A Novel Approach for the Short-Term Forecast of the Effective Cloud Albedo

Isabel Urbich[1], Jörg Bendix[2] and Richard Müller[1]

[1] Deutscher Wetterdienst, Frankfurter Straße 135, 63067 Offenbach, Germany
[2] University of Marburg, Faculty of Geography, Deutschhausstraße 12, 35032 Marburg, Germany

This chapter was published in
Remote Sensing, Vol. 10, No. 6, 955, DOI: 10.3390/rs10060955;
Received: 27 April 2018;
Revised: 23 May 2018;
Accepted: 8 June 2018;
Published: 15 June 2018

Abstract

The increasing use of renewable energies as a source of electricity has led to a fundamental transition of the power supply system. The integration of fluctuating weather-dependent energy sources into the grid already has a major impact on its load flows. As a result, the interest in forecasting wind and solar radiation with a sufficient accuracy over short time periods (<4 h) has grown. In this study, the short-term forecast of the effective cloud albedo based on optical flow estimation methods is investigated. The optical flow method utilized here is TV-L^1 from the open source library OpenCV. This method uses a multi-scale approach to capture cloud motions on various spatial scales. After the clouds are displaced, the solar surface radiation will be calculated with SPECMAGIC NOW, which computes the global irradiation spectrally resolved from satellite imagery. Due to the high temporal and spatial resolution of satellite measurements, the effective

cloud albedo and thus solar radiation can be forecasted from 5 min up to 4 h with a resolution of 0.05°. The validation results of this method are very promising, and the RMSE of the 30-min, 60-min, 90-min and 120-min forecast equals 10.47%, 14.28%, 16.87% and 18.83%, respectively. The paper gives a brief description of the method for the short-term forecast of the effective cloud albedo. Subsequently, evaluation results will be presented and discussed.

Zusammenfassung

Die Arbeit an einer Kürzestfristvorhersage der solaren Einstrahlung am Boden ist durch eine steigende Nutzung erneuerbarer Energien als Stromquelle begründet, die zu einem fundamentalen Wandel des Energieversorgungssystems geführt hat. Die Integration fluktuierender, wetterabhängiger Energiequellen in das Stromnetz hat bereits jetzt einen enormen Einfluss auf dessen Ladungsflüsse. Als Folge dessen stieg das Interesse an präziseren und kurzfristigeren Vorhersagen des Windes und der solaren Einstrahlung. In dieser Arbeit wird die Kürzestfristvorhersage der effektiven Wolkenalbedo basierend auf der Berechnung des optischen Flusses untersucht. Die hier verwendete Methode für diese Berechnung ist TV-L^1 aus der freien Programmbibliothek OpenCV. Diese Methode verwendet einen Multi-Skalen-Ansatz, um Wolkenbewegungen auf unterschiedlichen räumlichen Skalen zu erfassen. Nach der Wolkenverlagerung wird die solare Einstrahlung am Boden mit Hilfe des Programms SPECMAGIC NOW berechnet, welches die Globalstrahlung spektral aufgelöst aus Satellitenbildern erstellt. Durch eine hohe zeitliche und räumliche Auflösung der Satellitenmessungen kann die effektive Wolkenalbedo und somit auch die solare Einstrahlung von 5 min bis zu 4 h mit einer Auflösung von 0.05° vorhergesagt werden. Im Folgenden wird es eine kurze Beschreibung der Methode der Kürzestfristvorhersage der effektiven Wolkenalbedo geben. Ferner werden Ergebnisse der Evaluierung gezeigt und diskutiert. Schließlich wird ein Ausblick auf zukünftige Entwicklungen gegeben.

3.1 Introduction

The power supply system is under fundamental transition. The replacement of fossil fuels by renewable energy is progressing rapidly. Weather-dependent energy sources such as wind and solar radiation play a major role within the transition. The integration of wind and solar energy into the grid has a huge impact on the load flows. For this reason, the forecasts of solar radiation and wind have to be more precise with particular regard to the short-term forecast for up to 3–4 h. Thus, a forecast based on satellite observations, also referred to as nowcasting, is of priority choice for this issue. It shows better results for the first few hours of photovoltaic power forecasts (PV forecasts) in comparison to numerical weather prediction models (NWP) (Wolff et al., 2016). Further, NWP runs with data assimilation need usually 3–6 h of computation time. Thus, the results of the

numerical weather prediction model are only available with a time delay of several hours, whereas satellite-based forecasts are available in near real time.

The temporal short-term variation of the solar surface irradiance in Central Europe is predominantly related to cloud occurrence. Thus, an accurate short-term forecast of relevant cloud properties is of high importance. The main challenge is to properly forecast the location and the shape of clouds for the next few hours from satellite data. For the forecast of clouds, we use the optical flow methods TV-L^1 and Farnebäck provided by the OpenCV library through calculating cloud motion vectors (OpenCV, 2020). Optical flow is a widely-used and well-established technique for image pattern recognition in the fields of traffic, locomotion and face re-detection. An overview of different optical flow methods and their application is given by Sonka et al. (2014). So far, however, TV-L^1 and other optical flow methods are hardly used for the calculation of cloud motion vectors in meteorology. To our knowledge, one of the first applications has been the utilization of the optical flow for radar images as described by Peura and Hohti (2004). Optical flow has been recently implemented for the short-term forecast of radar reflectivity at the German Weather Service ("Deutscher Wetterdienst"), as well. The success of the estimation of the optical flow of radar images indicates that the method could be transferred to the forecast of clouds and their properties. A promising candidate for the forecast of cloud properties is the effective cloud albedo (CAL). CAL is derived from the reflectivity measured in the visible bands of satellites. The advantages of the effective cloud albedo are manifold. For instance, CAL can be directly observed from space, without the need for any additional model or information (Müller et al., 2011). For CAL values up to 0.8, the cloud transmission for solar radiation is simply defined by $1-\mathrm{CAL}$ (Müller et al., 2011). Thus, the effective cloud albedo includes the required information about the cloud effect on the solar surface irradiance. Further, the reflection of the Earth's surface is already filtered, allowing optical flow to focus on clouds. As a result, satellite observations enable the retrieval of the CAL and solar radiation at the ground, with high spatial and temporal resolution and a large areal coverage. For further information on the retrieval of the effective cloud albedo, the reader is referred to Müller et al. (2011). In our study, the effective cloud albedo of two subsequent images is used as the input for the estimation of the optical flow method. The estimated cloud motion vectors are then applied on the latter of these two images to extrapolate the observed cloud albedo into the future. Further details on this topic are given in Section 3.2.1.

Straightforward methods for the calculation of cloud motion vectors are based on the minimization of the root mean square error (RMSE) or the absolute difference between a shifted image in the x-y direction and the subsequent image. The cloud motion is defined by its shift in the x-y direction, which minimizes the RMSE or absolute difference between the images. This can be applied to various spatial scales and thus is called the multi-scale approach. Multiple scales lead to a dense vector field; however, more scales also increase the computation time needed. The cloud motion vectors applied for the satellite weather at the German Weather Service (Rosenow et al., 2001) are an example of a straightforward multi-scale approach, which is based on the above-described minimization of the absolute differences. Another example is the method of Schmetz et al. (1993). Here, a cross-correlation method is used for the cloud motion vectors. In this method, image filtering, also known as slicing, is applied to enhance the highest cloud

tracer suitable for tracking. This filtering leads to a relative low density of cloud motion vectors, which is a significant disadvantage for energy meteorology applications. The Nowcasting Satellite Application Facility (NWC SAF) uses a similar approach, namely a gradient method, to define the cloud edges and cross-correlation for the calculation of the motion vectors (Pereda, 2016). This method also leads to a low density of cloud motion vectors and is therefore not appropriate for energy meteorology. Originally, the main application of satellite-derived cloud motion vectors was the use of wind fields in the data analysis for numerical weather prediction where a dense field might be less important (Schmetz et al., 1993). However, only a dense field of cloud motion vectors enables a forecast with large geographical coverage and high temporal resolution without data gaps.

In the last few years, cloud motion vectors have gained significantly in importance within the scope of PV forecasts, and recently, their relevance has also been recognized for short-term forecasts of wind energy. However, a dense vector field of cloud motion vectors is a precondition for energy meteorology applications. Neural networks (NN) are therefore widely used to gain a dense vector field from high resolution satellite images with the advantage of a low computation time. Voyant et al. (2017) provide a review of neural network methods applied to the forecast of solar surface radiation. A disadvantage of neural networks is their black box character. A neural network is, strictly speaking, only valid for the training framework, as only the behavior of the training datasets can be reproduced. An application to other regions, periods or satellite instruments typically requires extensive re-training. Further, the black box character hampers a deeper understanding of the involved physics and physical reasons of the uncertainties occurring.

Thus, optical flow methods might be a good alternative for the estimation of cloud motion vectors. However, they are not mentioned neither in the review of photovoltaic power forecasting performed by Antonanzas et al. (2016), nor by the review of very short PV forecasting with cloud modeling by Barbieri et al. (2017). Other leading experts, for example Raza et al. (2016), Perez et al. (2014) or Wolff et al. (2016), do not mention optical flow methods provided by OpenCV as an option for cloud forecasting. However, the optical flow of satellite images has been used for the Geometric Accuracy Investigations of the Spinning Enhanced Visible and Infrared Imager (SEVIRI) High Resolution Visible (HRV) Level 1.5 Imagery (Aksakal, 2013). Further, Simonenko et al. (2017) discussed the optical flow method TV-L^1 concerning the interpolation between observed cloud images, in order to improve the temporal information about convective volcanic ash plumes. However, neither the short-term forecast of solar surface irradiance, nor its application were addressed. As a consequence, only a few works about the application of optical flow methods for the forecast of cloud motion vectors from satellite imagery and practically no works on satellite based short-term forecast of solar surface irradiance exist. Yet, the authors are aware of only one publication in which a multiple-scale optical flow method is applied within the scope of satellite-based solar irradiance forecasts (Sirch et al., 2017). The respective method is developed within the storm detection and nowcasting system Cb-TRAM (Tracking and monitoring severe convection from onset over rapid development to the mature phase using multi-channel Meteosat-8 SEVIRI data) (Zinner et al., 2008, 2013). Unfortunately, the details of the method are not well

described, and the software is not available in open access, which limits the scientific benefit of the work. Further, the authors applied the cloud motion vectors to cloud optical thickness and effective radius, but not to CAL. For the correct retrieval of cloud optical depth and effective radius r_{eff}, accurate information of the surface albedo and the atmospheric composition is needed. Furthermore, simplifications in the radiative transfer are typically applied within the retrieval of the cloud optical depth and r_{eff}. These items induce uncertainties in the estimation of the solar surface irradiance, which can be avoided if the satellite-observable CAL is used.

Thus, to the knowledge of the authors, the optimization of the recent TV-L^1 method and its application to the effective cloud albedo for the forecast of solar surface irradiation is a novel approach within energy meteorology. Furthermore, this work is one of the first in which the two optical flow methods of the OpenCV library (TV-L^1, Farnebäck) are evaluated and compared in the context of cloud albedo forecasting. The authors believe that the combination of the effective cloud albedo with TV-L^1 and SPECMAGIC NOW (Müller et al., 2012) delivers a new powerful method for the short-term forecast of solar surface irradiance.

3.2 Materials and Methods

3.2.1 Optical Flow Method

Optical flow is a pattern of apparent motion of image objects between two sequential frames caused by either the movement of the object or the camera (Burton and Radford, 1978). Three-dimensional motion of objects can be projected onto a two-dimensional plane by calculating the optical flow. Its result is a vector field where each vector is a displacement vector showing the movement of pixels from the first frame to the second (Beauchemin and Barron, 1995). Once computed, the optical flow can be used for a wide range of tasks (Barron et al., 1994). It may be applied for motion detection, object segmentation, motion compensated encoding and stereo disparity measurements. On top of that, it can be used to reconstruct the three-dimensional motion of visual sensors and surface structures (Beauchemin and Barron, 1995).

The optical flow works on two major assumptions, which are (1) that the pixel intensities of an object do not change between consecutive frames and (2) that neighboring pixels have similar motion. The assumption of constant intensity $I(x(t), y(t), t)$ between two consecutive frames is valid for all of the following methods. $I(x(t), y(t), t)$ can be expressed as follows (Sánchez et al., 2012):

$$\frac{d}{dt} I(x(t), y(t), t) = 0 \tag{3.1}$$

where $(x(t), y(t))$ represents the trajectory of a point in the image and t is the time. Applying the chain rule results in the following functional:

$$\nabla I \cdot (\dot{x}, \dot{y}) + \frac{\partial}{\partial t} I = 0 \tag{3.2}$$

which is equivalent to the following linear condition called the optical flow constraint equation (Horn and Schunck, 1981):

$$\nabla I \cdot \mathbf{u} + \frac{\partial}{\partial t} I = 0. \tag{3.3}$$

This equation alone is not sufficient for the estimation of the optical flow though, because there are twice as many variables as equations because this linear equation is dependent on x and y. This linear system is therefore undetermined. At this point, many methods for the determination of the optical flow were found to solve the problem by adding various conditions, as for instance block-based methods, discrete optimization methods and differential methods (Baker et al., 2011). The latter offers some more options, for instance the Lucas–Kanade method or the Horn–Schunck method (Zhang and Chanson, 2018; Horn and Schunck, 1981), which were the first to extend the problem with additional conditions. Both are based on partial derivatives of the image signal or the sought flow field and higher-order partial derivatives. The most common algorithms for meteorological purposes concerning optical flow are by Farnebäck (2003) and the duality-based approach of the method TV-L^1 (Sánchez et al., 2012; Zach et al., 2007).

The optical flow estimation by Farnebäck (2003) is the older method. It uses two frames to estimate the flow. In a first step, the neighborhood of both frames has to be approximated by quadratic polynomials. This can be efficiently done by using the polynomial expansion transform. In a second step, the displacement has to be estimated with the help of the coefficients of the polynomial expansion:

$$f(x) \sim x^T \mathbf{A} x + \mathbf{b}^T x + c \tag{3.4}$$

where $\mathbf{A}$ is a matrix, $\mathbf{b}$ is a vector and c is a scalar. These coefficients are calculated from a weighted least squares fit to the signal value in the neighborhood. Typically, the center point has the highest weight, while the surrounding weights decrease radially. Large displacements can cause large errors in the estimated motion because the general assumption of Farnebäck is that the local polynomials at the same coordinates in the two images are identical except for a displacement. This issue can be solved by a multiscale approach, which means that the algorithm starts at a coarse scale to get a rough displacement estimate and continues with finer scales to obtain a more accurate estimate (Farnebäck, 2003).

TV-L^1 is a variational method based on the method by Horn and Schunck (1981), however using other data and smoothness terms (Zach et al., 2007). Like the Farnebäck method, TV-L^1 uses two frames to estimate the optical flow. The TV-L^1 method is based on the minimization of a functional containing a data term using the robust L^1-norm in the data fidelity term and a regularization term using the total variation (TV) of the flow (Sánchez et al., 2012). The method is based on the minimization of the following image-based error criterion:

$$\int_\Omega \Big\{ \lambda \phi \left(I_0(\mathbf{x}) - I_1(\mathbf{x} + \mathbf{u}(\mathbf{x})) \right) + \psi(\mathbf{u}, \nabla \mathbf{u}, \dots) \Big\} \, d\mathbf{x}. \tag{3.5}$$

In this formula, I_0 and I_1 denote the two image frames and $\mathbf{u} : \Omega \to \mathbb{R}^2$ denotes the disparity map, which should be found with this method. Further, the disparity map $\mathbf{u}$ is the minimizer of the above-mentioned criterion (Equation (3.5)). The term $\phi(I_0(\mathbf{x}) - I_1(\mathbf{x} + \mathbf{u}(\mathbf{x})))$ describes the image data fidelity, and $\psi(\mathbf{u}, \nabla\mathbf{u}, \dots)$ represents the regularization term. Moreover, λ works as a weighting factor between the data fidelity and the regularization term. If one selects $\phi(x) = x^2$ and $\psi(\nabla\mathbf{u}) = |\nabla\mathbf{u}|^2$, the result will be the Horn–Schunck method. As the algorithm by Farnebäck, the TV-L^1 method uses scale-space approaches and, on top of that, coarse-to-fine warping to provide solutions for optical flow estimations with large displacements. Because the algorithm contains discontinuities, it is more robust against noise than the classical approach by Horn and Schunck (1981).

In the numerical implementation of both algorithms, there are several parameters to adjust the estimation of the optical flow to the sort of data with which one is working. This can range from the number of scales for the multi-scale approach to smoothing factors and the number of iterations (see Section 3.3.2). However, the amount of parameters differs, as well as the type of parameters of the two algorithms. The algorithm of Farnebäck uses 8 parameters, while the TV-L^1 method by Zach et al. uses 10, when settings for the inner and outer iterations are considered separately (Farnebäck, 2003; Zach et al., 2007). For further information on the technique, the reader may refer to the website of OpenCV (2020).

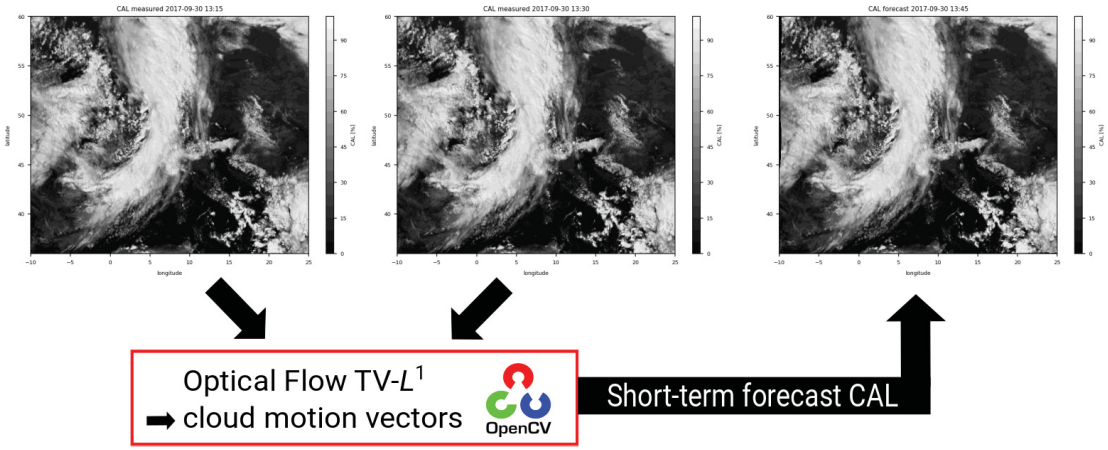

Figure 3.1: Scheme of the optical flow method. Two images of the effective cloud albedo serve as input for the TV-L^1 method. The estimated cloud motion vectors are then applied to the latter of the consecutive images to extrapolate the cloud motion into the future.

After the calculation of the motion vectors for the optical flow estimation, they need to be applied to a data field to achieve the forecast. A schematic diagram of the forecasting process is given in Figure 3.1. In a first step, two subsequent images of the effective cloud albedo are used as input for the TV-L^1 method (or Farnebäck method) to estimate the optical flow. TV-L^1 (Farnebäck) estimates the optical flow, which results from the differences between the two subsequent images induced by the movement of the clouds. The so-derived cloud motion vectors are then applied to the latter of the two observed CAL images in order to extrapolate the variation in CAL induced by the movement of

the clouds into the future. This process can be repeated as often as desired until a certain forecast time is reached at which the NWP delivers better results than the satellite-based short-term forecast.

3.2.2 The Heliosat Method

The effective cloud albedo can be derived from geostationary satellites by using the observed reflectances from the visible bands without the need for any further information. The effective cloud albedo is also referred to as the cloud index by other authors (Cano et al., 1986; Beyer et al., 1996; Hammer et al., 2003). Here, the visible channel at 600 nm from SEVIRI on board the Meteosat Second Generation (MSG) is used for the calculation of the effective cloud albedo. The data are provided by the European Organization for the Exploitation of Meteorological Satellites (EUMETSAT) as rectified images of digital counts, capturing the signal of the reflection of the Earth's atmosphere and surface.

The location of the geostationary satellites is over the Equator at 0° longitude with a field of view up to 80°N/S and 80°E/W, respectively. An example of the full disk is illustrated in Figure 3.2 for a clear sky reflection and effective cloud albedo case. The effective cloud albedo can be defined as the normalized difference between the all-sky and the clear-sky reflection in the visible range observed by the satellite. One minus the effective cloud albedo defines the cloud transmission for values of the albedo between 0 and 0.8. For effective cloud albedo values above 0.8, this relation will be modified in order to consider the saturation and absorption effects in optically thick clouds (Müller et al., 2011). Due to the fact that illumination conditions may vary because of the Sun-Earth distance and the solar zenith angle, the effective cloud albedo has to be corrected. Furthermore, the dark offset of the instrument has to be subtracted from the satellite image counts. The observed reflections are therefore normalized by applying the following equation:

$$\rho = \frac{D - D_0}{f \cos(\theta)} \tag{3.6}$$

Here, D is the observed digital count including the dark offset of the satellite instrument. D_0 is the dark offset, which is the baseline value of the instrument in the absence of irradiance, and therefore, it has to be subtracted. The Sun-Earth distance variation is taken into account by the factor f. Finally, the cosine of the solar zenith angle corrects the different illumination conditions at the top of the atmosphere introduced by different solar elevations.

The effective cloud albedo can be derived from the normalized pixel reflection ρ, the clear sky reflection ρ_{cs} and the maximal cloud reflection $\rho_{\max}$ as follows:

$$\mathrm{CAL} = \frac{\rho - \rho_{\mathrm{cs}}}{\rho_{\max} - \rho_{\mathrm{cs}}} \tag{3.7}$$

Here, ρ is the observed reflection for each pixel and time, and ρ_{cs} is the clear sky reflection, which is calculated according to an approach of Müller et al. (2012) within the scope of spectral clear-sky reflectance. The maximum reflection $\rho_{\max}$ is determined by the 95th percentile of all reflection values ρ at local noon in a target region. It is characterized

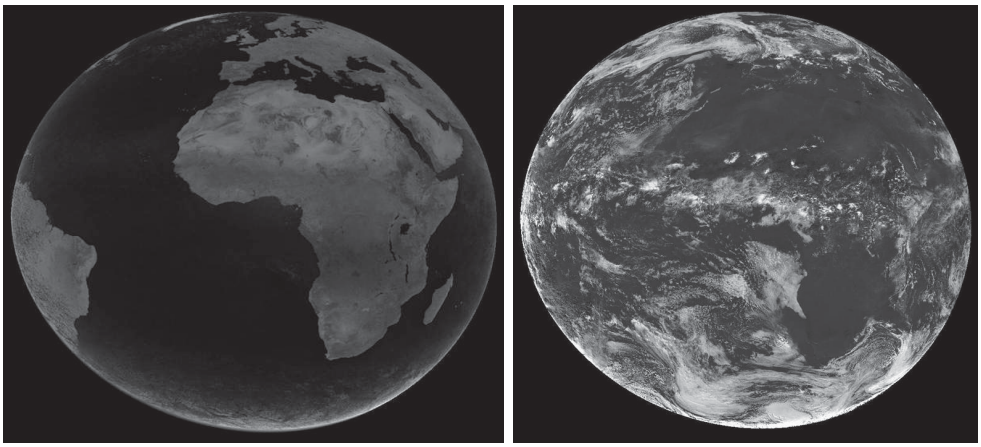

Figure 3.2: Example of the clear sky reflection ρ_{cs} (left) and effective cloud albedo CAL (right) for an 11 UTC slot in June 2005.

by a high frequency of cloud occurrence for each month. Thus, changes in the satellite brightness sensitivity are accounted for. All reflection types were corrected in the same manner using Equation (3.6).

Only the observed reflections are needed to derive the effective cloud albedo with the application of Equation (3.7). As a result, the effective cloud albedo is completely defined by the satellite observation with only one broadband visible channel needed. The accuracy and limitations of the method are discussed in Müller et al. (2011).

The aim of the application of the optical flow onto the effective cloud albedo is to obtain a short-term forecast of the solar surface irradiation. First of all, the optical flow of the effective cloud albedo is used to displace the clouds, and after that, the solar surface radiation can be calculated. The solar surface irradiance is retrieved using the well-established Heliosat relation between the effective cloud albedo and the solar irradiance, which is based on the law of energy conservation (Hammer et al., 2003; Cano et al., 1986). As a consequence, the basic relation between the solar irradiance and the effective cloud albedo is predominantly a linear relation. This relation and the method to estimate the solar surface irradiation using CAL as the input is described in the work of Müller et al. (2012). For effective cloud albedo values above 0.8, the above equation is modified in order to consider the saturation and absorption effects in optically-thick clouds. The modification of the equation for small and large values of the effective cloud albedo is based on ground measurements and is described in more detail in Hammer et al. (2003). The forecast of solar surface irradiance relies on the accuracy of the forecasted effective cloud albedo. As the clear-sky variables are not forecasted, it is the only quantity of interest for the present forecast study and thus for the following results and discussion.

3.2.3 Verification

For the purpose of verifying the optical flow results, we calculated the absolute difference of the optical flow estimate and the measured satellite image. The unit of this result is %, as it is the unit of the effective cloud albedo, as well. This was done for all investigated

cases. On top of that, three different error measures were calculated on the bases of the absolute difference. These are the bias, the absolute bias and the root mean square error. The exact calculation of the error measures is as follows (3.8)–(3.10):

$$\text{bias} = \frac{1}{n}\sum_{i=1}^{n}(x_i - y_i) \tag{3.8}$$

$$\text{absolute bias} = \frac{1}{n}\sum_{i=1}^{n}|x_i - y_i| \tag{3.9}$$

$$\text{RMSE} = \sqrt{\frac{1}{n}\sum_{i=1}^{n}(x_i - y_i)^2} \tag{3.10}$$

3.3 Results

3.3.1 TV-L^1 Versus Farnebäck

As mentioned in Section 3.2.1, there were two prominent methods to estimate the optical flow for meteorological purposes. We calculated the absolute difference of the optical flow estimate and the measured satellite image as described in Section 3.2.3 to decide whether the Farnebäck or the TV-L^1 method performed better for the effective cloud albedo. The parameter settings for the comparison were done by eye, which is sufficient because differences can become small when setting the parameter values. The absolute difference is shown in Figure 3.3, and the absolute bias for this case and for another 10 exemplary cases can be found in Table 3.1.

First of all, the higher absolute difference of the optical flow calculated with the method by Farnebäck is obvious. Moreover, the absolute bias is 5.43% for the Farnebäck method, and it is 4.37% for the TV-L^1 method. Furthermore, the RMSE is higher for the Farnebäck method (9.53%) compared to 7.59% with TV-L^1. Beyond this single event, the TV-L^1 method shows better results for all examined cases, so that this method is used to estimate the optical flow with the effective cloud albedo.

There are 10 different parameters in the TV-L^1 method DualTVL1OpticalFlow from OpenCV, which can be modified to influence the result of the optical flow estimation. Some parameters like the stopping criterion ϵ, the time step τ, as well as the inner and outer iterations can affect the speed of the algorithm. ϵ must be selected as a compromise between precision and running time. A small ϵ value gives a more accurate solution, but at the cost of a slower convergence. The time step τ is responsible for the stability of the algorithm. Chambolle (2004) showed that the numerical scheme converges for values of $\tau < 0.125$. However, its value can also be set to 0.25 for a faster convergence, which was found out empirically by Sánchez et al. (2012). For the multi-scale approach mentioned in Section 3.1, the method needs the number of scales N_{scales} and the downscaling factor or so-called scale step, which is used to divide the original data to create a pyramidal structure. The value of the downscaling factor can range between zero and one. Other

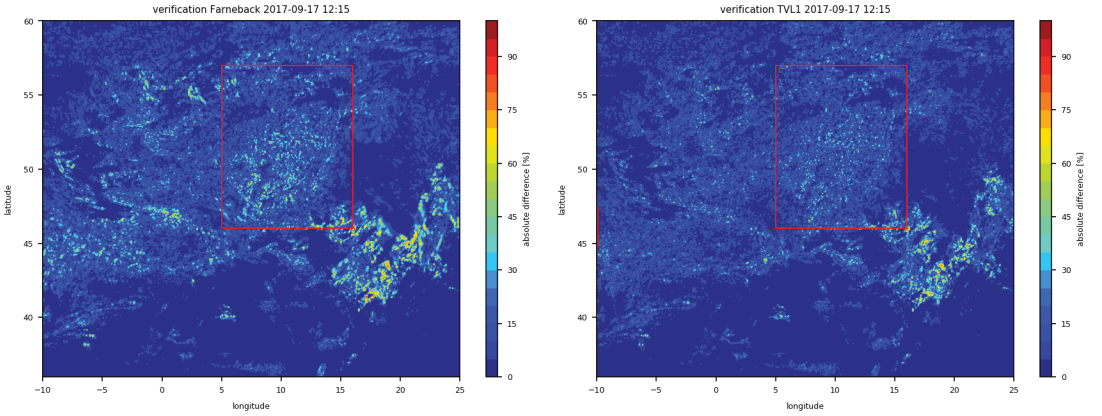

Figure 3.3: Plots of the verification of the optical flow estimate with the method by Farnebäck (left) and the TV-L^1 method (right) for a 15-min forecast. The area of Germany is marked by the red frame.

Day	Time	Farnebäck		TV-L^1	
		Abs. Bias	RMSE	Abs. Bias	RMSE
7 August 2017	09:00	5.07	9.19	3.87	7.03
11 August 2017	15:00	7.4	12.81	5.54	9.81
15 August 2017	15:00	6.67	12.22	4.83	8.96
1 September 2017	12:00	6.36	11.29	4.67	8.46
17 September 2017	12:00	5.43	9.53	4.37	7.59
22 September 2017	09:00	6.82	11.24	5.25	8.82
30 September 2017	13:00	7.19	11.68	5.31	8.75
1 October 2017	09:00	7.25	11.19	5.57	8.73
3 October 2017	13:00	9.34	14.76	6.79	10.78
4 October 2017	12:00	7.62	12.18	5.94	9.57

Table 3.1: Calculated absolute bias and RMSE for both optical flow methods, the one by Farnebäck and with TV-L^1. The error measures were calculated for a 15-min forecast over the area of Europe. The unit of the error measures is %. These are 10 exemplary cases because the superiority of TV-L^1 can be clearly seen already, and these values are sufficient to see the difference between the performance of the methods.

parameters have an influence on the shape of the forecasted clouds, for instance the data attachment weight λ and the tightness parameter θ. λ is the most important parameter because it determines the smoothness of the result. θ serves as a link between the attachment and the regularization terms. If the value of θ is small, the correspondence of both terms can be maintained. For our data, two of the parameters were less sensitive to the data: the illumination parameter γ and the number of warpings N_{warps}. Consequently, the setting of these parameters hardly affected the results. γ represents an additional illumination term, which can affect the tracking of clouds, but did not in the current analysis. Finally, N_{warps} describes the number of times that the specific terms were computed per scale. The choice of its value is a compromise between speed and accuracy of the calculations. For further information on the parameters, the reader may refer to Sánchez et al. (2012).

3.3.2 Parameter Optimization

The first task when estimating the optical flow is to change the parameters of the algorithm in a way that the optical flow for the type of data is optimal. For the short-term forecast of solar surface irradiance, we used the effective cloud albedo as the variable for the calculation. To optimize the parameters of the optical flow algorithm, we calculated the bias, absolute bias and RMSE as error measures over the area of Europe (−10–25°N, 36–60°E). The results of the absolute bias for the forecast times from 15 min–120 min are shown in Figure 3.4. It is shown that the error of the forecast increases non-linearly with the forecast time. The error growth rate decreases with time, which leads to a root-function-shaped graph. This shape can be more or less bent, as can be seen in Figure 3.4 in the left plot, but the function never reaches linearity.

To choose the optimal value for each parameter of the TV-L^1 method, the values had to be changed several times. The optical flow estimate with the parameter value that corresponds to the lowest absolute bias is the most optimal one. However, this is not always as easy as it sounds. For some cases, the parameter values have to be changed for each forecast time. Because this would be difficult to declare for every single case, there should be a better solution. As the differences between a case with optimal and second best values are small, the solution was to calculate the integral of the function seen in Figure 3.4 with the composite trapezoidal rule to get the overall optimum for the whole forecast. This was done for all 21 cases with a variety of weather situations between August and October 2017 (see Table A.1 in the Appendix A). Despite the fact that different weather situations were analyzed, the choice of the parameter values was quite clear, and therefore, it was valid for all short-term forecasts of the effective cloud albedo. Again, the differences of the bias values for optimal and second best parameter values were small, but not negligible. The results of this optimization can be seen in Table 3.2.

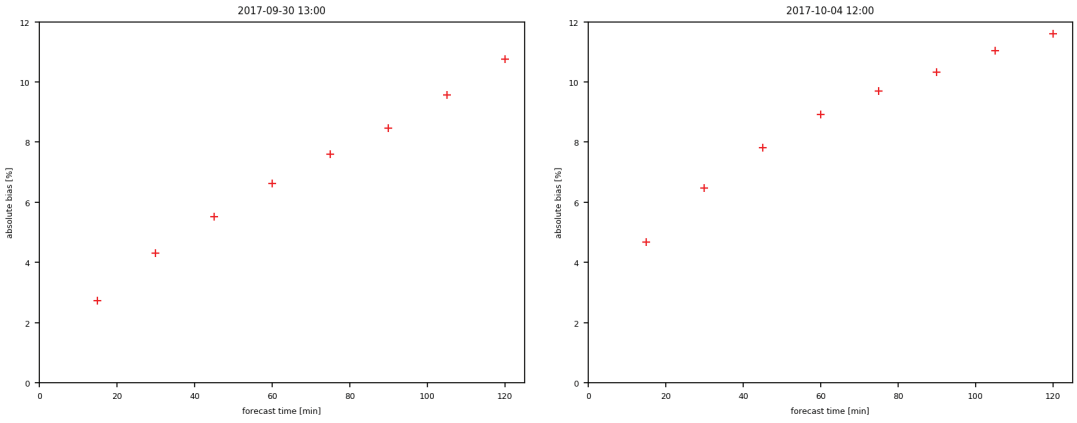

Figure 3.4: Plots of the absolute bias of the effective cloud albedo against the forecast time for the cases of 30 September 2017 at 13:00 UTC (situation with convection behind a front over Germany) and 4 October 2017 at 12:00 UTC (stratiform situation). The unit of the absolute bias is %.

Parameter	Value	Parameter	Value
γ	0.1	outer iterations	2
τ	0.1	inner iterations	10
λ	0.03	N_{warps}	3
θ	0.3	N_{scales}	3
ϵ	0.01	scale step	0.5

Table 3.2: List of parameter settings for the TV-L^1 method in the DualTVL1OpticalFlow algorithm by OpenCV.

A common approach for numerical models, as well as short-term forecasts is to choose the parameter values in dependence of the spatial scales. In this study, we examined the choice of the parameter value again, but for shorter time periods concerning smaller spatial scales. The result was that the values presented in Table 3.2 perfectly fit for all forecast times. As can be seen in Figure 3.4, the plots do not show two or more different regimes, which proves the good choice of the parameters. In other words, the function of the absolute bias against the forecast time is continuous and linearly growing. Moreover, it does not show jumps or features that would differ greatly from the observed shape. The number of cases where this separate choice of parameter values would be successful was too small to be efficiently implemented in the algorithm. On top of that, the achieved effect would be very small.

3.3.3 One Hundred Twenty-Minute Forecast

In the following subsection, we present two examples of a 120-min forecast based on the optical flow of the effective cloud albedo. The utilized algorithm is DualTVL1OpticalFlow from OpenCV with the parameter values listed in Section 3.3.2. The two examples were already introduced in the previous subsection.

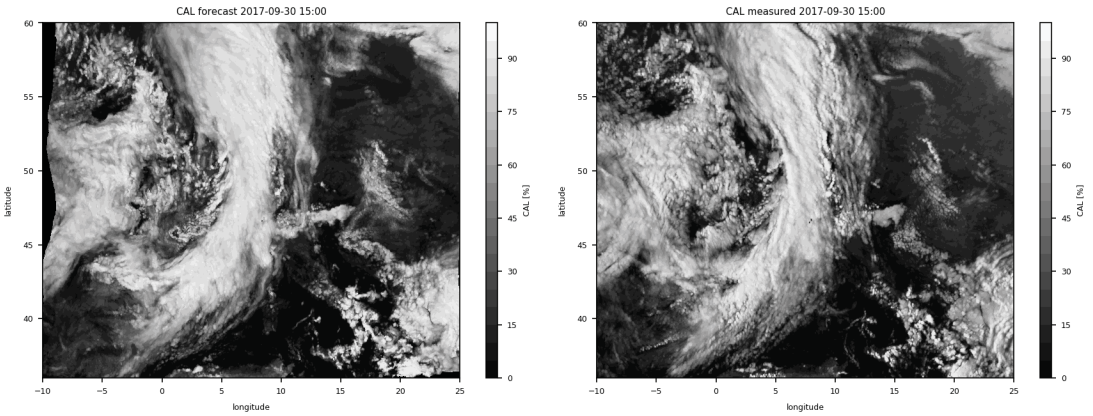

Figure 3.5: A short-term forecast for 120 min of the effective cloud albedo for 30 September 2017 at 15:00 UTC can be seen in the left figure. The satellite image by MSG with the effective cloud albedo depicted for comparison is shown in the right image.

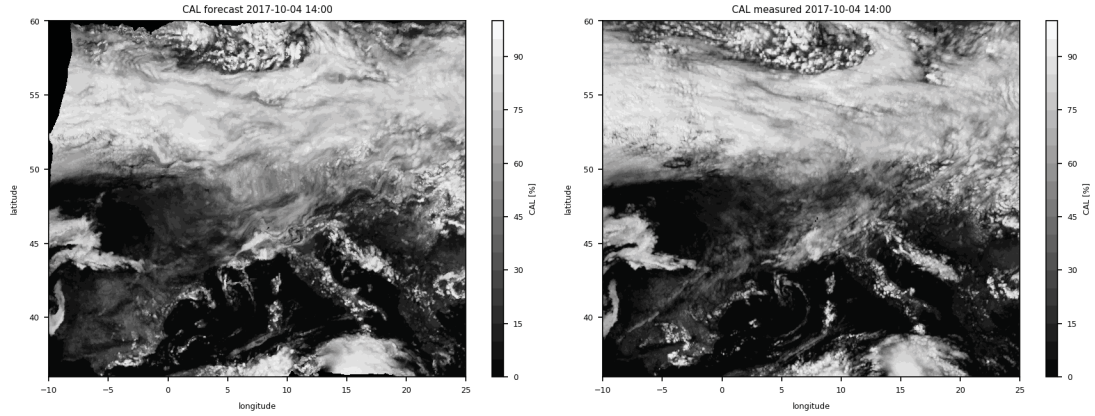

Figure 3.6: A short-term forecast for 120 min of the effective cloud albedo for 4 October 2017 at 14:00 UTC can be seen in the left figure. The satellite image by MSG with the effective cloud albedo depicted for comparison is shown in the right image.

The first case (see Figure 3.5) shows a quasi-stationary front over Central Europe and post-frontal convective clouds in the west. The front extends from north to south and moves towards the east. Additional convective clouds can be seen over southern Italy and the surrounding ocean.

The forecast figure can be easily recognized by its inward moving edge (Figure 3.5, left). Due to the given dataset to which the optical flow is added, there is no new information after shifting these cloud pixels to its calculated position. In other words, in an optical flow estimation, all boundary conditions are set to zero. Besides that, the figure depicts a 120-min-forecast, so the clouds usually move further than in a shorter time period. Moreover, the forecast figure can be identified by inspecting the cloud top structure. Due to the fact that a new formation or dissipation of clouds cannot be reproduced with the optical flow estimate, the visual surface structure of the clouds is softer. In the observed satellite image, the cloud tops especially in the area of the front are more structured and show many small details (Figure 3.5 right). All in all, the position and spatial extent of the cloud formation in the forecast fits quite well to the observations.

The second case shown here is a different weather situation. Stratiform clouds extend over large parts of Central Europe in the northern part of the chosen area (see Figure 3.6). Again, convective clouds over southern Italy and the Balkans can be detected. Compared with the observations (Figure 3.6, right), the surface structure of the simulated cloud area looks quite similar. Nevertheless, the extension to the south is larger in the forecast because over the area of Austria and Switzerland, the clouds dissipated in the time period of 120 min. Furthermore, a few new clouds that cannot be seen in the forecast are formed on the southern tip of Italy.

To verify these short-term forecast results of the effective cloud albedo, we calculated the absolute difference between the simultaneous forecast and satellite image. The verification results for the above discussed cases (see Figures 3.5 and 3.6) can be seen in Figure 3.7.

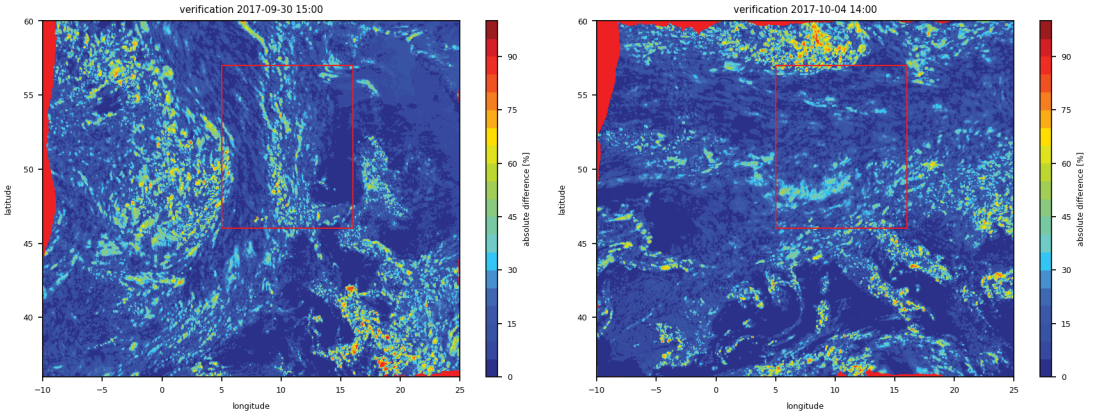

Figure 3.7: Verification plots of the optical flow method for the cases of 30 September 2017 at 15:00 UTC and 4 October 2017 at 14:00 UTC. The absolute difference between the effective cloud albedo from satellite imagery and the effective cloud albedo from the short-term forecast for 120 min in % is shown.

Forecast Time (Min)	Bias (%)	Absolute Bias (%)	RMSE (%)
30	0.11	5.95	9.49
60	-0.37	8.68	13.40
90	1.55	10.77	15.77
120	1.98	12.99	18.16

Table 3.3: Values of the bias, absolute bias and RMSE for the case of 30 September 2017. The basis for the calculation is the area of Europe.

Forecast Time (Min)	Bias (%)	Absolute Bias (%)	RMSE (%)
30	0.85	6.02	9.57
60	1.48	8.24	12.85
90	1.93	9.61	14.69
120	1.84	10.78	16.21

Table 3.4: Values of the bias, absolute bias and RMSE for the case of 4 October 2017. The basis for the calculation is the area of Europe.

On 30 September, the verification confirms the above-mentioned quality of the forecast. Higher deviations can be seen in areas with the formation of convective clouds, for example over the Mediterranean Sea near the southern tip of Italy or in the area west of the front. Here, the absolute difference can reach values up to 80% in small areas. Moreover, the change of the cloud top structure of the front seems to cause trouble for the algorithm, as well. This can be explained through the changing intensity of each pixel throughout the forecast time. The bias is small for the whole area with 1.98% after 120 min. The other error measures are higher (absolute bias = 12.99%, RMSE = 18.16%) than the bias, which shows that positive and negative deviations are canceled out in the short-term forecast, which is generally the case. All error measures for this case can be found in Table 3.3.

The bias for the 120-min forecast (bias = 1.84%) is also quite low for 4 October 2017. The other error measures are higher, as well, so that the positive and negative deviations are canceled out, as well (see Table 3.4). Most of the clouds, especially in the stratiform precipitation area, were forecasted very well, and the verification shows only small deviations. Areas with high absolute differences can be found north of the stratiform clouds and in the south. Both situations can be explained through the formation of new clouds and the changing intensity of cloud pixels. This behavior violates the criterion for the optical flow estimation, which states that the intensity of the pixels has to be constant over time. This is, however, not fulfilled in all cases. Therefore, weather conditions where cloud formation or dissipation occurs pose a problem for the optical flow estimation.

3.4 Discussion

The applications of optical flow estimates are diverse. As shown in Section 3.3.3, the utilization of the optical flow estimation for a short-term forecast of the effective cloud albedo and hence of the solar surface irradiance shows promising results. Validation results reported in recent review publications by Voyant et al. (2017), Antonanzas et al. (2016) or Barbieri et al. (2017) and publications by other leading experts (Raza et al., 2016; Wolff et al., 2016; Cros et al., 2014) do not provide any hints that the application of the widely-used neural networks leads to a significantly better accuracy for cloud motion vectors. In Cros et al. (2014), for example, the RMSE of the 30-min forecast of the effective cloud albedo was about 30% for a neural network approach and a phase correlation method. Thus, the discussed optical flow method might be among the best approaches for cloud motion vector estimation. Moreover, the big advantage of the TV-L^1 approach, which has been optimized here for the effective cloud albedo, is the free access and the comprehensive documentation of the method. However, no matter which satellite-based method for cloud motion vectors is used, the limit of a good short-term forecast compared to NWP is approximately between 120 and 240 min because the forecast is only based on the optical displacement of pixels. The method does not lead to good forecast results after a certain time threshold. Comparisons with the numerical weather prediction models will be conducted in the future to provide more detailed information about the time when the accuracy of the NWP matches that of TV-L^1. Further, we plan to investigate the benefit of rapid scan imagery, which are available every 5 instead of 15 min.

A currently known problem of satellite imagery methods is the formation or dissipation of clouds in the forecast, which can be caused for example by fast processes such as convection. This is confirmed by our verification results (see Figure 3.7). As mentioned above, one criterion of the optical flow is that the intensity of image pixels has to stay constant between two consecutive frames. Due to the fact that convective clouds form very fast, this is clearly not fulfilled. Nevertheless, these areas where convection can be found are very small in comparison to stratiform clouds or fronts and, thus, are rather negligible for renewable energy forecasts. A common approach for short-term forecasts is the separation into sub-scales. Convection is a fast small-scale process, while pressure systems with fronts can extend up to 1000 km and exist for days. To cover both regimes,

the optimization process can be done for the first 60 min and the second 60 or more minutes. This was already conducted for the 21 cases mentioned, but it did not improve the forecast. From 21 cases, there were only four in which a separate optimization would be useful. Besides, the differences between the optimal and the second best parameter value are in the range of hundredths and thus negligible. The implementation of such a parameter change would just be too costly.

3.5 Conclusions

The demand for more precise short-term forecasts for wind and solar irradiance over shorter time horizons is growing as a consequence of the increasing use of renewable energies. A short-term forecast of solar surface irradiance can be obtained via optical flow estimation of the effective cloud albedo. For this purpose, we used the TV-L^1 algorithm by Zach et al. available from OpenCV (Zach et al., 2007; OpenCV, 2020). As is shown in Figure 3.3 and Table 3.1, the method by Zach et al. for the estimation of the optical flow delivers better results than the method by Farnebäck, a short-term forecast of the effective cloud albedo. The presented experiments show that the use of TV-L^1 for the estimation of the optical flow works well for the short-term forecast of the effective cloud albedo and thus for the solar surface irradiance. Due to the high temporal and spatial resolution of satellite measurements, the short-term forecast of solar surface irradiance can cover a period of 5 min up to 4 h with a spatial resolution of 0.05°. The calculated RMSE for the 30-min, 60-min, 90-min and 120-min forecast equals 10.47%, 14.28%, 16.87% and 18.83%, respectively (see Table A.2 in the Appendix A for more error measures). Overall, the error measures are small for the examined cases, although the formation and dissipation of clouds pose problems for the optical flow estimation in general. One of the major assumptions for the optical flow estimation is that the intensity of pixels remains similar between two consecutive time frames. However, this is not fulfilled when new clouds occur or grow. This is the case because the newly-formed top of the cloud consists of smaller droplets, and thus, the effective cloud albedo is higher because more light is reflected. Moreover, larger clouds or clouds at other positions can be formed in the time between the two frames. Nevertheless, these issues normally take place on small scales and do not influence the regional forecast too much. In general, the results show that the approach is very promising.

Acknowledgments

We thank Manuel Werner and Stephane Haussler for sharing their experience in optical flow estimation with us. Thanks to Markus Kunert, Michael Mott, Nils Rathmann and Manuel Werner for the introduction and support regarding the POLARA framework, which was developed by the department of radar meteorology at the German Weather Service. We also thank Matthias Jerg for the cross-reading of the manuscript.

Chapter 4

The Seamless Solar Radiation (SESORA) Forecast for Solar Surface Irradiance—Method and Validation

Isabel Urbich[1], Jörg Bendix[2] and Richard Müller[1]

[1] Department for Research and Development, Deutscher Wetterdienst, Frankfurter Straße 135, 63067 Offenbach, Germany
[2] Faculty of Geography, University of Marburg, Deutschhausstraße 12, 35032 Marburg, Germany

This chapter was published in
Remote Sensing, Vol. 11, No. 21, 955, DOI: 10.3390/rs11212576;
Received: 11 September 2019;
Revised: 29 October 2019;
Accepted: 29 October 2019;
Published: 2 November 2019

Abstract

Due to the integration of fluctuating weather-dependent energy sources into the grid, the importance of weather and power forecasts grows constantly. This paper describes the implementation of a short-term forecast of solar surface irradiance named SESORA (seamless solar radiation). It is based on the optical flow of effective cloud albedo and available for Germany and parts of Europe. After the clouds are shifted by applying cloud motion vectors, solar radiation is calculated with SPECMAGIC NOW (Spectrally Resolved Mesoscale Atmospheric Global Irradiance Code), which computes the global irradiation spectrally resolved from satellite imagery. Due to the high spatial and temporal

resolution of satellite measurements, solar radiation can be forecasted from 15 min up to 4 h or more with a spatial resolution of 0.05°. An extensive validation of this short-term forecast is presented in this study containing two different validations based on either area or stations. The results are very promising as the mean RMSE (Root Mean Square Error) of this study equals 59 W/m^2 (absolute bias = 42 W/m^2) after 15 min, reaches its maximum of 142 W/m^2 (absolute bias = 97 W/m^2) after 165 min, and slowly decreases after that due to the setting of the sun. After a brief description of the method itself and the method of the validation the results will be presented and discussed.

Zusammenfassung

Durch die Integration fluktuierender wetterabhängiger Energiequellen in das Netz, nimmt die Bedeutung von Wetter- und Leistungsprognosen stetig zu. Dieses Paper beschreibt die Implementierung eines Nowcastings der solaren Einstrahlung mit dem Namen SESORA (seamless solar radiation). Sie basiert auf dem optischen Fluss der effektiven Wolkenalbedo und ist für Deutschland und Teile Europas verfügbar. Nachdem die Wolken durch die Anwendung von Wolkenbewegungsvektoren verschoben wurden, wird die Sonnenstrahlung mit SPECMAGIC NOW (Spectrally Resolved Mesoscale Atmospheric Global Irradiance Code) berechnet, welcher die Globalstrahlung spektral aufgelöst aus Satellitenbildern berechnet. Aufgrund der hohen räumlichen und zeitlichen Auflösung der Satellitenmessungen kann die Sonneneinstrahlung von 15 min bis zu 4 h oder mehr mit einer räumlichen Auflösung von 0.05° vorhergesagt werden. Eine umfassende Validierung dieser Kurzfristvorhersage wird in dieser Studie vorgestellt, die zwei verschiedene Validierungen enthält, die entweder auf dem Gebiet oder auf Stationen basieren. Die Ergebnisse sind sehr vielversprechend, da der durchschnittliche RMSE (Root Mean Square Error) dieser Studie nach 15 min 59 W/m^2 (absoluter Bias = 42 W/m^2) beträgt, nach 165 min sein Maximum von 142 W/m^2 (absoluter Bias = 97 W/m^2) erreicht und danach aufgrund des Sonnenuntergangs langsam abnimmt. Nach einer kurzen Beschreibung der Methode selbst und der Methode der Validierung werden die Ergebnisse vorgestellt und diskutiert.

4.1 Introduction

Over recent decades the overall need for an accurate spatiotemporal nowcasting of weather has increased due to the rising importance of renewable energies and the fluctuating energy supply due to the short-term variation in the governing atmospheric elements (e.g., clouds and solar radiation) (Aliberti et al., 2018; Wolff, 2017; Hammer et al., 2003). Particularly if renewable energies are integrated into the grid it is very important to correctly forecast the weather, as well as power needs, to prevent grid instabilities. Instabilities may occur as solar energy and wind energy have a major impact on the load flows and for this reason, forecasts have to become more precise, especially in the short-term range of 0–4 h (Vrettos and Gehbauer, 2019; Raza et al., 2016; Inman et al., 2013;

Barbieri et al., 2017). A merge between the numerical weather prediction (NWP) model and nowcasting will deliver a seamless product of the highest quality at any time. The main cause for instabilities in Germany, for instance, is the inhomogeneous distribution of wind turbines and photovoltaic systems, which often leads to capacity overloads. As a consequence, a forecast for solar irradiation as the basis of solar energy based on observations, also called nowcasting, will be developed in this work. As has been shown before, nowcasting with satellite data delivers better results for the first few hours compared to numerical weather prediction (NWP) models, due to its higher temporal and spatial resolution (Lorenz et al., 2012; Wolff et al., 2016; Kurz, 2018). Moreover, NWP model runs usually need 3–6 h of computation time, depending on the model, as a consequence of the data assimilation. Satellite measurements and derived nowcasting products, on the other hand, are available in near real time with a spatial resolution of 0.05°.

A common and frequently used approach to forecast solar surface irradiation is a neural network (Aliberti et al., 2018; Nikitidou et al., 2019). However, it has not yet been shown that neural networks have a higher forecast quality than cloud motion vectors or optical flow methods (Urbich et al., 2018). Another successful method is the use of a semi-Lagrangian scheme to calculate the advection of a flow (Turner et al., 2004; Lin et al., 2005; Berenguer et al., 2011). In contrast to a constant vector, as used in optical flow methods, the vectors for Lagrangian trajectories are iteratively determined for each time step to allow rotation of a flow (Germann and Zawadzki, 2002). Nevertheless, the differences between constant vectors and Lagrangian trajectories only stand out when there is rotation. Furthermore, especially at the beginning, differences are small and grow with increasing forecast time or distance (Germann and Zawadzki, 2002). Since we foresee a merge with an NWP model in our algorithm after about 4 h, differences will most likely stay small. Moreover, additional features, like the use of a history of satellite images instead of only two frames, or the enabling of curved trajectories where the past movement of a pixel will be taken into consideration, will be included in the algorithm of the SESORA forecast in the near future. Another great advantage of the optical flow method is that the algorithm of TV-L^1 (Method based on total variation in the regularization term and the L^1-norm in the data fidelity term) is open source and a large community is constantly working on improving this and other methods by OpenCV (2020) (Open Source Computer Vision). There are many successful solar radiation forecasts that have been published in recent years that use cloud tracking methods with either geostationary satellites (Hamill and Nehrkorn, 1993; Hammer et al., 2003; Lorenz et al., 2004; Harty et al., 2019), total sky imagery (Cheng, 2017), or ground sensors (Bosch et al., 2013). One method of cloud tracking is to derive cloud motion vectors (CMV) from satellite imagery. The general use of cloud motion vectors for nowcasting is widespread and many approaches have been proposed so far. Their application is not limited to forecasts in the scope of energy meteorology. In Guillot et al. (2012) cloud motion vectors were derived from satellite imagery and utilized to forecast cloud displacement over complex terrain. Velden et al. (1998) used atmospheric motion vectors (AMV) to better forecast the track of tropical cyclones. These vectors are derived from the infrared channel of MSG (Meteosat Second Generation) and since they do not only display the motion of the top of clouds they are called AMVs. In the field of solar radiation forecasts the use of cloud motion vectors is very common (Escrig et al., 2013; Nonnenmacher and Coimbra,

2014; Schroedter-Homscheidt and Gesell, 2016). Comparable studies from Gallucci et al. (2018) or Sirch et al. (2017) used cloud motion vectors from MSG/ SEVIRI (Spinning Enhanced Visible and Infrared Imager) to forecast solar surface radiation for up to 2 h. Due to different error measures and different study areas, a direct comparison of the quality reported in both studies is not possible. However, despite these small differences in validation method, the results are comparable and reported uncertainties are in a similar order. Gallucci et al. (2018) presented an RMSE (Root Mean Square Error) of 147 W/m^2 over Italy after 2 h of forecasting and Sirch et al. (2017) have found a correlation of 0.7 between the forecast and the observation after 2 h over Europe. Both studies reported higher errors due to convective clouds, which is a common problem in the scope of motion vectors since the method is not able to consider the formation and dissipation of clouds (Urbich et al., 2018; Gallucci et al., 2018).

The here presented solar radiation nowcasting is based on the optical flow of effective cloud albedo (CAL) (Urbich et al., 2018). CAL can be retrieved from the reflectivity measured in the visible channel of MSG and is therefore available every 15 min (Müller et al., 2011). The biggest advantage of using CAL for the optical flow estimation is that CAL has a direct connection to the cloud transmission and thus to the cloud effect on the solar surface irradiance. Apart from the effective cloud albedo, none of the other input parameters are forecasted. The reason for this is that SPECMAGIC NOW (Spectrally Resolved Mesoscale Atmospheric Global Irradiance Code) uses the same clear sky input data as in the Heliosat method used in SARAH-2 (Surface Solar Radiation Data Set - Heliosat). Forecasting only CAL therefore enables a clear separation of the errors induced by the CAL nowcasting since it represents the dominant error source for short-term fluctuations of solar irradiance in Central Europe. A list of further input parameters can be found below. For further information about the retrieval of CAL and the below listed input data the reader may refer to Müller et al. (2011); Müller et al. (2015); Mueller et al. (2015); Richard Müller (2014) or Trentmann (2014).

1. Aerosol is based on the Monitoring Atmospheric Composition and Climate Project (MACC) (Bellouin et al., 2013).

2. H_2O is taken from the European Centre for Medium-Range Weather Forecasts (ECMWF) (ECMWF, 2019).

3. Surface albedo is based on 20 different land-use types originating from the NASA CERES/SARB (Clouds and the Earth's Radiant Energy System / Surface Atmospheric Radiation Budget) Surface Properties Project (Loveland and Belward, 1997; Brown et al., 1993).

The optical flow requires two subsequent satellite images as input for the calculation of cloud motion vectors. The resulting motion vectors are then applied to the latter of these two images to extrapolate the observed clouds into the future. Additional information about the optical flow method and the effective cloud albedo nowcasting can be found in Section 4.2.2. After the propagation of the cloud is determined, solar surface radiation is calculated with SPECMAGIC NOW, which computes the global radiation, spectrally

resolved from satellite images in the visible channel (Müller et al., 2012). A detailed description of the algorithm will follow in Section 4.2.3.

The results of the CAL nowcasting were very promising, as the error measures of the forecast clearly showed (Urbich et al., 2018). The results were verified with satellite data from MSG for the area of Europe and the same error measures as in this publication were used (Section 4.2.4). A validation of the SESORA forecast is nevertheless necessary because of the integration of SPECMAGIC NOW. New features like the variability of the solar zenith angle and an all sky consideration may lead to other errors than in Urbich et al. (2018). Moreover, the errors of solar surface irradiance are very important for the application in the scope of PV (Photovoltaic) systems because the errors of solar irradiance and photovoltaic power have an almost linear relation (Lalouni et al., 2009; Islam et al., 2013). This can be derived from the performance curve of photovoltaic systems considering that the errors grow proportional to their associated values. This linear relation is a huge advantage concerning error growth over the cubical relation between wind and power for wind turbines (Kusiak and Verma, 2012; Albadi and El-Saadany, 2009). This information could significantly improve proper management of the grid loads.

4.2 Materials and Methods

The following section describes the validation data that were provided by the Satellite Application Facility on Climate Monitoring (CM SAF), the Baseline Solar Radiation Network (BSRN), and the German Weather Service. These data are now being used for the validation of the SESORA forecast. The methods of the optical flow and SPECMAGIC NOW will be presented and explained. The CAL data used for the here presented solar radiation nowcasting is one of the products of SPECMAGIC NOW and for further information the reader may refer to Urbich et al. (2018). Moreover, the utilized error measures of Sections 4.3.1 and 4.3.2 will be listed and described at the end of this section.

4.2.1 Validation Data

SARAH-2

For the area based validation of our SESORA forecast we used SARAH-2 data from the CM SAF. The solar surface irradiance data from the SARAH-2 data set is the latest CM SAF climate data record of surface radiation based on the geostationary Meteosat satellite series (Pfeifroth et al., 2018). In addition to solar surface radiation, the SARAH-2 dataset offers other global and direct radiation parameters but without a forecast. SARAH-2 covers the area of -65° to $+65^\circ$ in latitude and longitude with a spatial resolution of 0.05° (Pfeifroth et al., 2018) . The quality of the SARAH-2 data set in reference to BSRN data is well documented in Pfeifroth et al. (2017). A positive bias of 2 W/m^2 has been found and the absolute bias equals 5 W/m^2 for the monthly mean SARAH-2 data.

Ground Stations

We used ground stations for the validation of the SESORA forecast. To ensure a high coverage of ground stations for our validation we wanted to use the pyranometers from the BSRN as well as the pyranometer set from the German Weather Service. The data from the BSRN are known for their high quality standards as the data is quality controlled twice, at the stations and at the World Radiation Monitoring Center (WRMC) (Ohmura et al., 1998). The high quality is reflected in the low standard deviation of 5 W/m^2 for the global irradiance. The BSRN stations used and further information are depicted in Table A.3.

Additionally, we used a set of pyranometers from the German Weather Service. The data set consists of 34 stations and delivers global radiation at a temporal resolution of 1 min. These stations are located in Germany only. Their standard deviation equals 3% of the respective total daily radiation. Corresponding information about these stations is listed in Table A.4.

4.2.2 Optical Flow Method

In general, the optical flow describes the motion pattern between two sequential image frames of the same area. The result is a vector field where each vector is showing the movement of pixels from the first frame to the second (Beauchemin and Barron, 1995).

We generally use the optical flow of Horn and Schunck (1981) in a modification by Zach et al. (2007) (Urbich et al., 2018). The following constraint equation is the basis of all optical flow methods:

$$\nabla I \cdot \mathbf{u} + \frac{\partial}{\partial t} I = 0. \tag{4.1}$$

This equation describes a linear condition of the optical flow where $I(x(t), y(t), t))$ is the constant intensity between the two consecutive frames and $\mathbf{u}$ describes the two-dimensional velocity $(\dot{x}, \dot{y})$. A constant intensity is one of two major assumptions for the optical flow estimation. The second one is that neighboring pixels have to have similar motion (Beauchemin and Barron, 1995). The violation of these assumptions can lead to inconsistency and high, locally limited errors. An example for such a violation is the rapid formation of convective clouds between two consecutive frames. Thus, the first criterion, the intensity criterion, cannot be met because the reflectivity of the cloud top and its surrounding area is changing. The same effect can be seen when clouds or fog are dissolving as the value of CAL is changing in the opposite direction. An example case and further explanation about this topic can be found in Urbich et al. (2018).

A scheme of the application of the optical flow is shown in Figure 4.1. The first step of the algorithm takes two subsequent satellite images of the effective cloud albedo as input data for the optical flow method. Here, we use the TV-L^1 method from the open source library OpenCV (2020), as it is superior to the well known Farnebäck optical flow method (Farnebäck, 2003; Urbich et al., 2018). The algorithm computes the estimated flow between the two frames, which is induced by the movement of clouds. The result is a vector field with a cloud motion vector for each pixel in the area. In the second step, the

derived vectors are applied to the latter of the two observed CAL images to extrapolate the cloud movement into the future. In doing so, every pixel will be shifted, maintaining its original intensity. Thus their CAL value stays the same while their position can change. The step of applying the motion vectors to the satellite image can be repeated as often as required. In that case the vectors are applied to the latest forecast available in order to create a new one.

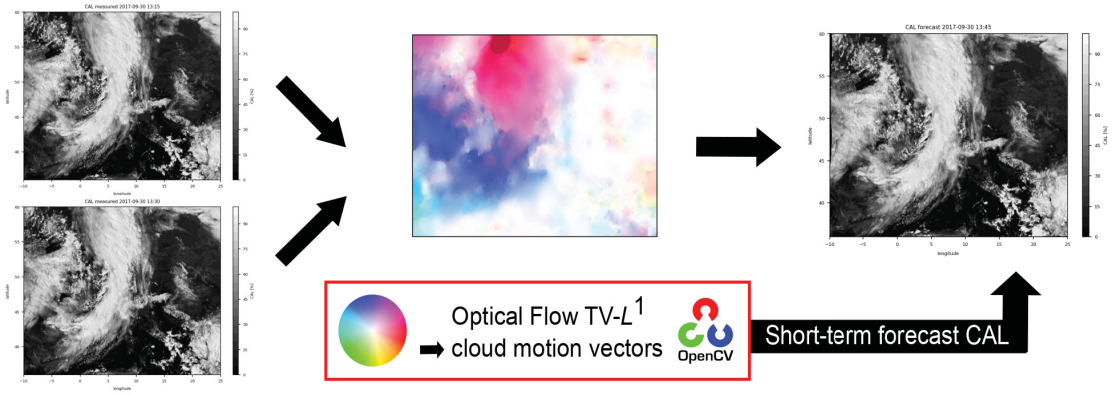

Figure 4.1: Scheme of the optical flow method TV-L^1 (Method based on total variation in the regularization term and the L^1-norm in the data fidelity term). Two subsequent images of the effective cloud albedo represent the input of the algorithm. The calculated motion vectors are then applied to the latter of the two images to extrapolate cloud albedo (CAL) into the future. For the sake of clarity the motion vectors are displayed with the help of the HSV (hue saturation value) color spectrum.

4.2.3 SPECMAGIC NOW

The SPECMAGIC NOW method is used in order to estimate the solar surface irradiance (SIS). In a first step the effective cloud albedo is being retrieved. It is derived from the geostationary satellite MSG by the reflectivity in the visible channel (Müller et al., 2011). The visible channel at 600 nm from SEVIRI on board of MSG is used for the calculation of CAL. The location of MSG is over the Equator at 0° latitude and longitude with a field of view from 80° S up to 80° N and from 80° E to 80° W. CAL is defined as the normalized difference between the all sky and clear sky reflectance in the 600 nm-visible channel of the satellite. The effective cloud albedo is equal to one minus the cloud transmission for values of CAL between 0 and 0.8 (Urbich et al., 2018). Above 0.8, this relation will be modified to consider the saturation and absorption effects in optically thick clouds. The effective cloud albedo is derived from the normalized pixel reflectance, ρ, the clear sky reflectance, ρ_{cs}, and the maximal cloud reflectance, ρ_{max} as follows:

$$\mathrm{CAL} = \frac{\rho - \rho_{\mathrm{cs}}}{\rho_{\mathrm{max}} - \rho_{\mathrm{cs}}}. \tag{4.2}$$

Here, ρ is the observed reflectance for each pixel and time, and ρ_{cs} is the clear sky reflectance, which is originally calculated according to an approach of Amillo et al. (2014). However, in this study, the original Heliosat approach is not used for the estimation of ρ_{cs},

instead it is derived from a database for spectral reflectance, as described in Müller et al. (2012). The maximal reflectance, max, is determined by the mean of the reflectance, ρ above the 95th percentile and below the 99th percentile in the target region.

The effective cloud albedo is derived from satellite observations and is therefore a satellite-derived variable. This observable defines the cloud transmittance. For clouds with CAL in the range from 0 to 0.8, the following relation between CAL and the solar surface irradiance (SIS) is used:

$$\mathrm{SIS} = (1 - \mathrm{CAL}) \cdot \mathrm{SIS}_{\mathrm{clear}}. \tag{4.3}$$

Here, $\mathrm{SIS}_{\mathrm{clear}}$ is the clear sky irradiance at surface, which is calculated by a hybrid look-up table (LUT) approach. It is based on radiative transfer modeling and is described in detail in Müller et al. (2012). Equation (4.3) is used to estimate the satellite based solar surface irradiance for the observed CAL images as well as for the CAL nowcasting. For the CAL nowcasting the optical flow method described in Section 4.2.2 is applied to the observed CAL images. The optical flow method could also be applied to raw images followed by the estimation of CAL. However, this would lead to additional uncertainties induced by the surface reflectance. These effects are diminished by the application of the optical flow to the CAL images directly.

4.2.4 Error Measures

The solar surface irradiance nowcasting was verified in two different manners. The first part was done with SARAH-2 data, which enables a validation of every pixel of the whole given area. For this purpose we calculated the absolute difference between the forecast and the SARAH-2 data field for each pixel. On the basis of that we calculated three different error measures, which are used in the scope of energy meteorology as standard. The equations are as follows:

$$\mathrm{bias} = \frac{1}{n} \sum_{i=1}^{n} (x_{\mathrm{forecast}} - x_{\mathrm{observation}}) \tag{4.4}$$

$$\text{absolute bias} = \frac{1}{n} \sum_{i=1}^{n} |x_{\mathrm{forecast}} - x_{\mathrm{observation}}| \tag{4.5}$$

$$\mathrm{RMSE} = \sqrt{\frac{1}{n} \sum_{i=1}^{n} (x_{\mathrm{forecast}} - x_{\mathrm{observation}})^2}. \tag{4.6}$$

Thus, we used the bias, absolute bias, and root mean square error for our validation. These errors were calculated for every examined case of this study. A list of all examined cases and their absolute bias can be found in Table A.5. The table with the RMSE values can be found in the Appendix (Table A.6). Further, we plotted the absolute difference, which is depicted in Section 4.3.1. Moreover, on the basis of the previously mentioned

error measures we calculated relative errors as follows:

$$\text{relative bias} = \frac{1}{n}\sum_{i=1}^{n}\left(\frac{x_{\text{forecast}} - x_{\text{observation}}}{\overline{x}_{\text{observation}}}\right) \tag{4.7}$$

$$\text{relative absolute bias} = \frac{1}{n}\sum_{i=1}^{n}\left|\frac{x_{\text{forecast}} - x_{\text{observation}}}{\overline{x}_{\text{observation}}}\right| \tag{4.8}$$

$$\text{relative RMSE} = \sqrt{\frac{1}{n}\sum_{i=1}^{n}\left(\frac{x_{\text{forecst}} - x_{\text{observation}}}{\overline{x}_{\text{observation}}}\right)^2}. \tag{4.9}$$

Here, $\overline{x}$ represents the mean of x.

The second part of the validation was performed with ground station data from BSRN and the German Weather Service (DWD). In that case we calculated the absolute difference between the observed radiation of the ground stations and the forecasted radiation of the nearest pixel to each corresponding station. Overall this results in 38 used pixels. The absolute bias and RMSE were calculated in the same way as above, however, on the basis of 38 single pixels. The results were plotted against the forecast time, together with the results of the nowcasting and the measurements of the stations (Section 4.3.2).

Based on the effective cloud albedo we determined a cloud mask where CAL = 0.025 marks the threshold between cloud and clear sky pixels. This value is similar to the usually used one in the literature, which equals 0.027 (Matsuoka et al., 2016). We found that for CAL = 0.025, the results were the most promising in reference to a significant distinction between cloud and clear sky pixels. Furthermore, the probability of detection was higher and the false alarm rate was lower with CAL = 0.025. This cloud mask was then used for verification with the SARAH-2 data to find the cause for high errors.

On the basis of this cloud mask we calculated the elements of the contingency table for the forecast and the observation, which are hit, missed, false alarm, and correct negative (Table 4.1). These elements were furthermore displayed in a map, which can be seen in Section 4.3.1. The elements were also used to calculate the probability of detection (POD) (Equation (4.10)) and the false alarm rate (FAR) (Equation (4.11)) as follows:

$$\text{POD} = \frac{a}{a+c} \tag{4.10}$$

$$\text{FAR} = \frac{b}{a+b}. \tag{4.11}$$

4.3 Results

Seventeen different cases were examined in this study based on different weather situations for the months of August until October, in 2017. The same cases have been already examined in Urbich et al. (2018) concerning the effective cloud albedo. A list of all cases and their error measures can be found in Tables A.5 and A.6. More cases in different

		Observation	
		Cloud	**No Cloud**
Forecast	Cloud	a = hit	b = fa
	No Cloud	c = miss	d = cn

Table 4.1: Contingency table with the elemtents hit, missed, false alarm (fa) and correct negative (cn).

seasons or years may not deliver additional information, as clouds play a dominant role in solar radiation forecasts. Therefore, we assume that the diversity of weather situations in this study should cover all relevant cloud types for a solar radiation forecast. In the following section two particular cases out of 17 in total will be discussed for the sake of clarity. The following cases show different weather situations and should be seen as representatives for the remaining cases.

4.3.1 SARAH-2

In Figure 4.2 the solar surface radiation is depicted for two different cases. The first case (Figure 4.2(a,b)) is 29 August 2017. The general weather situation was a high pressure system over central Europe. The second case (Figure 4.2(c,d)) is 30 September 2017 and in that case there was a low pressure system over western Europe and a front was passing Germany during the day. These cases were selected due to their different occurrence of clouds and solar radiation. A 255 min (4 h 15 min) forecast is shown in Figure 4.2(b,d) with the corresponding estimated SARAH-2 data set in Figure 4.2(a,c).

The forecasted radiation for the first case shows promising results compared to the SARAH-2 data. All in all, general structures are well met, as well as the height of the values themselves. The cloud structure over the North Sea is also shown by the nowcasting, however with less detail and a light displacement. This nowcasting consists of the optical flow of effective cloud albedo and the calculation of the radiation with SPECMAGIC NOW. Therefore, errors can be caused by two separate sources. That the cloud structure shows less details is probably caused by the effective cloud albedo nowcasting. Further, the broken clouds over Spain are displaced in the nowcasting. In particular, smaller clouds are more affected by the algorithm, as the fraction of cloud edges in relation to the inner part of the cloud is larger. Cloud borders can cause errors due to wrong advection and cloud dissipation or formation. Since the nowcasting works without any kind of boundary conditions or data beyond the depicted area there will always be some part of the plot with no data. This part is displayed in black. It grows with increasing forecast time because the edge is moving inwards. However, this is not a problem for the application of the SESORA forecast since the distribution (DSO) and transmission system operators (TSO) who will use the forecast only need the area of Germany and the surrounding regions.

Similar results can be observed in the second case. Except for smaller details, the position of clouds and the height of the radiation values are comparable. The structure of the

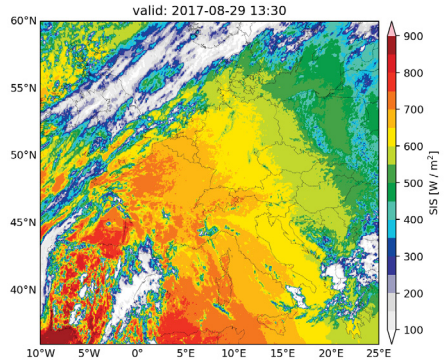

(a) SIS by SARAH-2 for 29 August 2017.

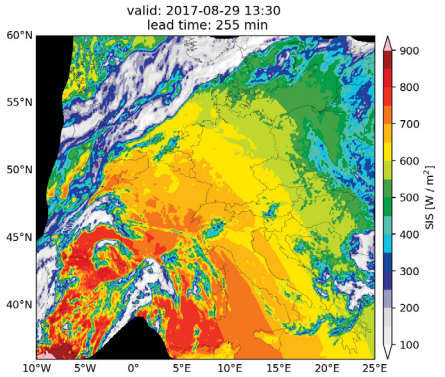

(b) SIS by SESORA forecast for 29 August 2017.

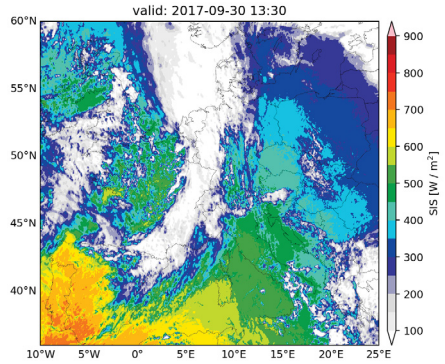

(c) SIS by SARAH-2 for 30 September 2017.

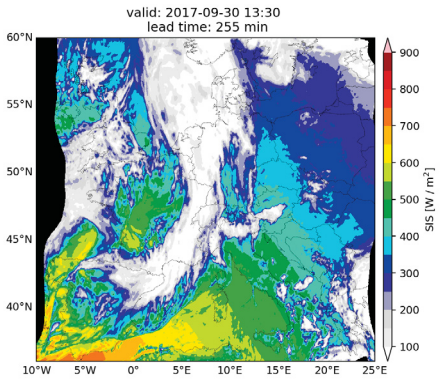

(d) SIS by SESORA forecast for 30 September 2017.

Figure 4.2: Plot of solar surface irradiation for 29 August 2017 (upper) and 30 September 2017 (lower). (a,c) show the estimated SIS by SARAH-2 and (b,d) show the forecasted SIS by SESORA after 255 min of forecast time.

front in the SARAH-2 data consists of more small clouds, which may have blurred out due to the long forecast time and the southern end of the front advecting too slowly in the nowcasting. Moreover, there is a cloud hole over southern Germany with higher radiation values than in the nowcasting, which is a result of an optically too thick cloud calculated by SPECMAGIC NOW. In general, one can say that cloud borders pose the biggest problem to the radiation forecast, as has been discussed before. Thus, the more small clouds, the higher the incidence of problematic edge regions, and the higher the errors will be.

To prove and visualize the previously seen differences, the absolute bias was calculated according to Equation (4.5), between the solar surface radiation nowcasting and the SARAH-2 data set. The results are displayed in Figure 4.3. The regions with higher errors correspond to the above mentioned regions. The cause of these errors are missing cloud structures, for instance over Austria, as well as incorrectly forecasted cloud edges,

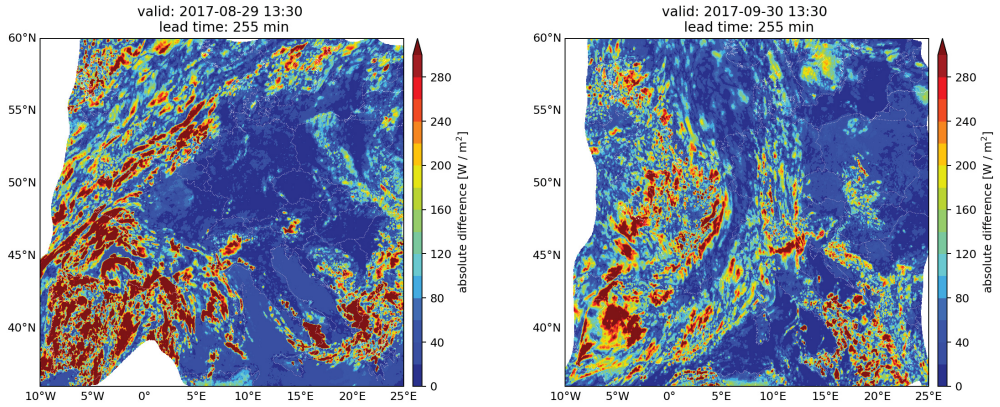

(a) Validation for 29 August 2017. **(b)** Validation for 30 September 2017.

Figure 4.3: Validation of the solar surface irradiation nowcasting with SARAH-2 data for 29 August 2017 (a) and 30 September 2017 (b). Depicted is the absolute difference between the SIS nowcasting and the SARAH-2 data set for a 255 min forecast.

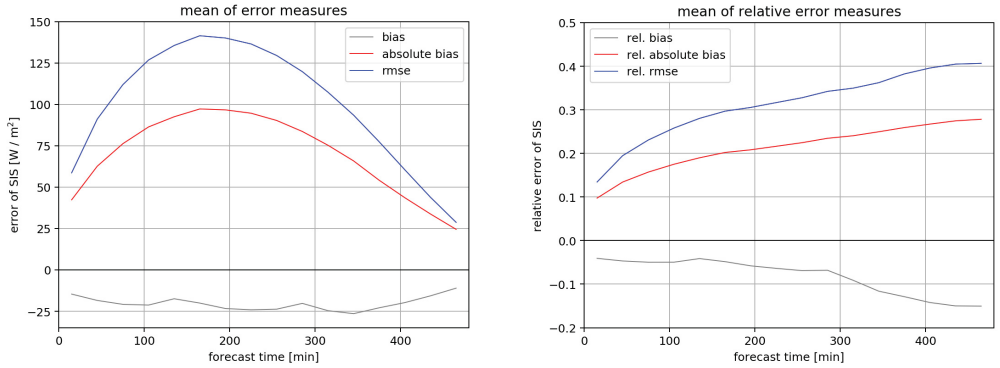

(a) Mean of absolute errors of SIS. **(b)** Mean of relative errors of SIS.

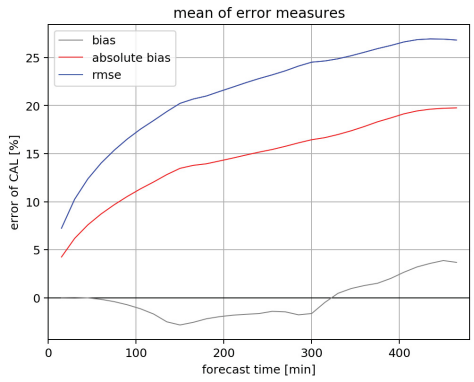

(c) Mean of absolute errors of CAL.

Figure 4.4: Plots of the mean error measures of all cases against forecast time for absolute (a) and relative errors (b) of SIS as well as the absolute errors of CAL (c). The validation of the solar surface irradiance was performed with SARAH-2 data by the CM SAF and the validation of the effective cloud albedo was done with the effective cloud albedo itself.

as can be seen over the North Sea and Spain (Figure 4.3(a)). These errors grow as usual with increasing forecast time. The absolute bias for 255 min equals 92 W/m^2 and the RMSE equals 143 W/m^2. As this is a nowcasting of solar surface irradiance, the values, and also the errors, decrease when the sun sets. This effect cannot be seen at this stage of the forecast, however it can be observed in Figure 4.4.

In the case of 30 September 2017 the validation appears different (Figure 4.3(b)). One of the issues in the nowcasting was the broken prefrontal clouds. Due to a generally less detailed effective cloud albedo, nowcasting the structure of these clouds looks different. This led to a slightly incorrect nowcasting of solar radiation between the clouds. Another problem is the back of the front. Smaller cloud structures are missing as well. What can be observed in Figure 4.3(b) are many smaller regions of errors over Germany, which are not as big as the error behind the front over France. An absolute bias of 79 W/m^2 and a RMSE of 112 W/m^2 have been found for this case.

In Figure 4.4 the mean of all error measures for all cases is plotted against forecast time. In Figure 4.4(a) there are the absolute measures and in Figure 4.4(b) there are the relative error measures. A list of all cases examined can be found in Tables A.5 and A.6. All forecasts were initiated at 09:15 UTC and the maximum forecast time was 480 min. Depicted are the bias (gray), the absolute bias (red), and the root mean square error (blue), respectively. What can be observed in Figure 4.4(a) is that the absolute bias and RMSE grow with increasing forecast time until approximately 180 min. After that, both error measures decrease again due to sunset. The behavior of the bias looks different because it does not represent an absolute error but rather a tendency. Therefore, one can say that for all times the nowcasting underrates solar irradiation, thus the estimated solar radiation by SARAH-2 delivers higher SIS values (Equation (4.4)). This is a result of SPECMAGIC NOW, which currently calculates the optical thickness of clouds higher than it should, due to ρ_{cs} being too low (Equation (4.2)). In fact, this kind of error can be fixed quite quickly, and an update of SPECMAGIC NOW is already planned, where ρ_{cs} will be adapted to reduce the bias. The relative errors show, as expected, a different behavior. As the errors are normed by the mean of the observed SIS values, the sunset does not play a role in this case (Equations (4.7)–(4.9)). The relative absolute bias and the relative RMSE rise with increasing forecast time. The slope of these two curves decreases with increasing forecast time, which results in a slower growth of the relative errors. The maximum of the RMSE is 0.41 and the maximum value of the relative absolute bias is 0.28. For the sake of a forecast validation without the influence of the solar altitude the mean of all error measures of the effective cloud albedo is depicted in Figure 4.4(c). The absolute bias and RMSE show the same behavior as the absolute bias and RMSE of the relative errors of SIS. The bias is negative for the first 300 min and turns positive afterwards.

Another method of verifying the quality of the SESORA forecast is a linear regression for all examined cases. Therefore the forecasted values of solar radiation were plotted against the observed radiation with the help of the SARAH-2 data set for each pixel in every frame and for each case dependent upon the forecast time. The results are shown in Figure 4.5. Moreover, a standardized regression was done where the solar zenith angle of the forecasted and observed solar radiation was corrected. Thus, sunset is less important

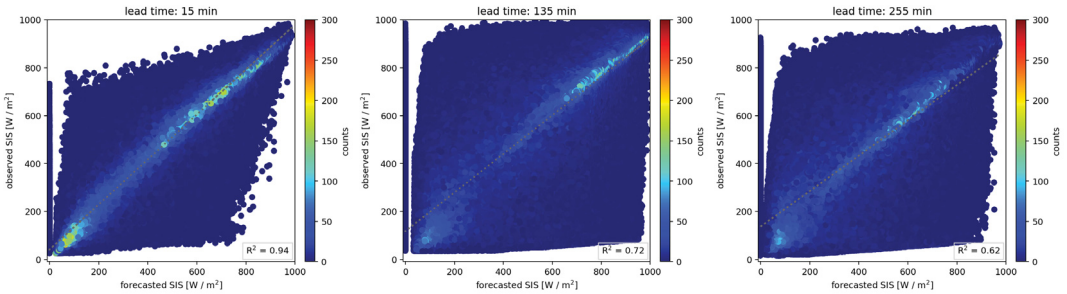

(a) Linear regression for 15 min. **(b)** Linear regression for 135 min. **(c)** Linear regression for 255 min.

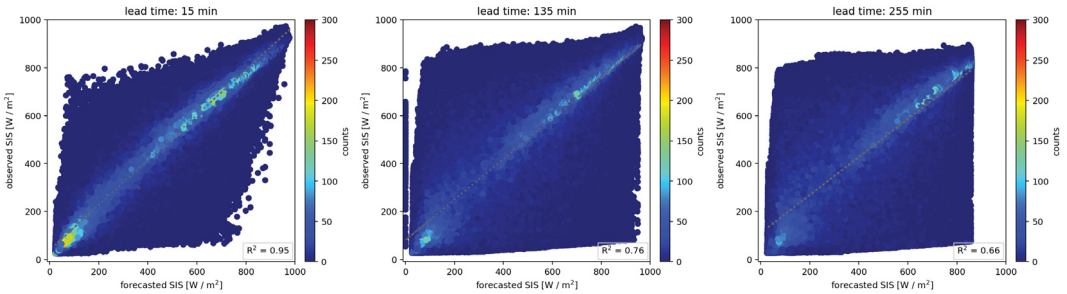

(d) Standardized linear regression for 15 min. **(e)** Standardized linear regression for 135 min. **(f)** Standardized linear regression for 255 min.

Figure 4.5: Linear regression of the forecasted and observed absolute solar surface irradiation and standardized solar surface irradiation. Depicted are the results for 15 min (a,d), 135 min (b,e), and 255 min (c,f) of forecast time respectively. R^2 is printed in the lower right corner of every figure.

for the quality of the forecast. As expected the distribution in Figure 4.5(a–c) gets broader with increasing forecast time and the values of SIS get smaller in the observation as well as in the nowcasting because of the sunset. Most of the data points are lying on the diagonal whereby the distribution is split into a maximum for smaller and a maximum for higher values of solar irradiance. This behavior remains unchanged throughout the forecast. The slope is smaller than 1 for all forecast times, which underlines the negative bias found in Figure 4.4. As can be seen in Figure 4.5 for the forecast times 135 min and 255 min, the observed values are higher than the forecasted SIS values especially for small values. As a comparison, the bias for all forecast times until 400 min was ≈ -25 W/m^2. Looking at the spread we can see that there are more small values of solar radiation, and therefore the linear regression does not begin at the origin as it is shifted upwards. That is also the reason for general slope values below 1 for all forecast times. The quality of the linear regression is represented by the R^2-value, which is displayed in the lower right corner of each linear regression plot. After 15 min the R^2 remains quite high with a value of 0.94. After 135 min we found a R^2 of 0.72. A forecast time of 2 h is a typical length for nowcasting, thus it is a common forecast time for comparisons with other publications. Sirch et al. (2017) found a R^2-value of 0.71 for a DNI (Direct Normal Irradiance) nowcasting after 120 min in March and a value of 0.64 in July (Sirch et al., 2017). It can be observed that the forecast quality improves when the angle of the sun

is being corrected. This underlines the fact that the bias of ≈ -25 W/m^2 found in the validation with the SARAH-2 data arises from a systematic error in SPECMAGIC NOW. The p-value for all forecast times was smaller than $1 \cdot 10^{-300}$, which shows the high significance of the distribution. It also proves that the distribution of the data is non-normal thus we can reject the null hypothesis.

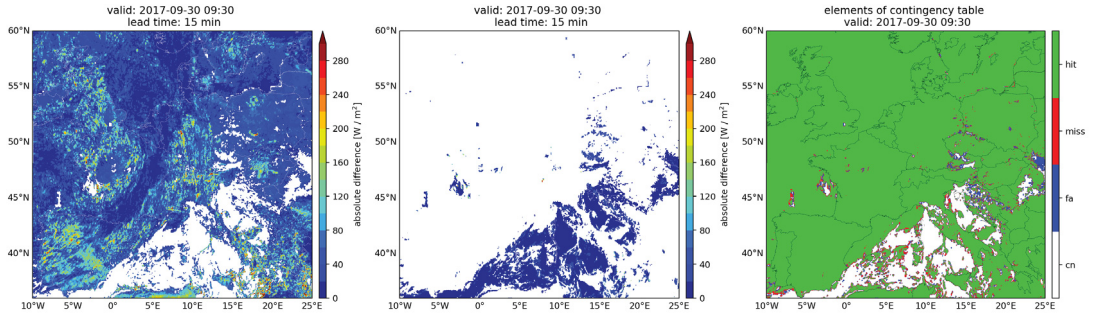

(a) Absolute difference of cloud area for 15 min. **(b)** Absolute difference of clear sky area for 15 min. **(c)** Elements of contingency table for 15 min.

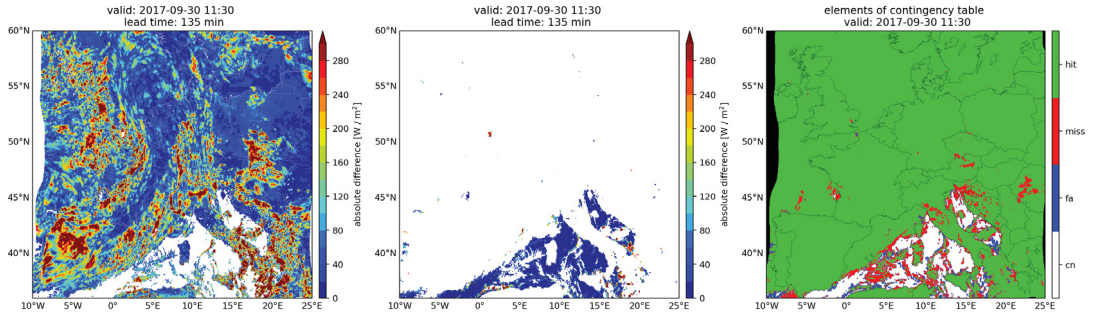

(d) Absolute difference of cloud area for 135 min. **(e)** Absolute difference of clear sky area for 135 min. **(f)** Elements of contingency table for 135 min.

Figure 4.6: Results of the validation for 30 September 2017 with SARAH-2 and an additional cloud mask. Depicted are the absolute difference between the nowcasting and the SARAH-2 data (a,b,d,e), as well as a map of the elements of the contingency table (c,f). These results are shown for 15 (upper) and 135 min (lower), respectively.

It is essential to distinguish between different error sources in a nowcasting, for the improvement of the algorithm, however, the more steps of computation are involved, the more complications may be found. For the SESORA forecast we found a systematic error in the calculation of the solar surface irradiance, which can be clearly seen in the constant bias in Figure 4.4. This bias can be corrected by adjustments in SPECMAGIC NOW and it is not related to TV-L^1. For the remaining part of our algorithm, which is the nowcasting of the effective cloud albedo, we divided the errors into cloudy pixels and clear sky pixels (Section 4.2.4). The idea is to detect errors resulting from convection or advection separately. The results are shown in Figure 4.6.

In Figure 4.6(c,f), the errors that are marked miss and false alarm (fa) mostly arise from wrong advection of the optical flow algorithm. When the TV-L^1 method calculates a cloud motion too slowly or too quickly, this leads to errors at the edge of the clear

sky area. In the cloudy area this error can occur as well, however we cannot find them with our analysis. If our algorithm calculates the cloud motion too slowly we will get a miss and if the motion is calculated too quickly we will get a false alarm. However, in general we detect more misses than false alarms. Moreover, the errors rise with increasing forecast time as can be seen in Figure 4.6(f). The magnitude of errors cannot be extracted from this graphic, although when we take Figure 4.6(b) into account we can see that the errors due to wrong advection are rather small. The errors in Figure 4.6(b,e) are small in general. Thus, the errors with the highest magnitude are caused by clouds. These kind of errors can be detected in Figure 4.6(a,d) and they all are caused by a change of intensity of the effective cloud albedo over time. As was already mentioned in Urbich et al. (2018), the change of the pixel intensity over time is a major issue for the optical flow. These errors have the highest magnitude and appear more frequently than errors due to wrong advection. As usual, all errors grow with increasing forecast time (Figure 4.6(d–f)).

4.3.2 Ground Stations

In Figure 4.7(a) the nowcasting for 255 min of the solar surface irradiance is displayed for 29 August 2017. Overall, the measurements of the ground stations show agreement with the nowcasting in this case. For this type of validation we must keep in mind that the geometry of these two measurements is completely different. MSG is located at 0° longitude and latitude, and thus its viewing angle to the surface in the area of Europe is slant. In contrast, pyranometers are standing at the surface and only measure the radiation above them. Furthermore, we are comparing point observations with area integrals of approximately 16 km^2 (in the area of Germany). This is especially difficult if there are sub-pixel scattered clouds. These effects add uncertainties that are not caused by shortcomings of the nowcasting method. So, in some cases the value of the ground station does not seem to fit to the forecasted radiation but this could be either an artifact of the geometry of the satellite or the comparison of point observations with areas.

Figure 4.7(b) shows the same content as in Figure 4.7(a) for 30 September 2017. Again, the inward moving edge on the left side of the figure can be observed. The agreement of the stations and the nowcasting is not as good as in the Figure 4.7(a) of 29 August 2017. The station of Palaiseau (marked by a red circle) shows higher values than the nowcasting. Even in the surrounding area such high values between 600 and 650 W/m^2 cannot be found. The same can be observed for the station of Arkona (marked by a red circle), which also measured values between 400 and 450 W/m^2 however the nowcasting shows values below 350 W/m^2.

The error measures of the validation with ground stations are depicted in Figure 4.8. Displayed is the mean of all 17 cases against forecast time for the area of Europe. The corresponding solar surface irradiance value of the nowcasting (red), as well as the one of the ground stations (blue) is plotted against forecast time for overall 480 min. We only selected the satellite pixels of the nowcasting that corresponded to a pixel of a ground station. Although it is a common approach to take the mean of a 3×3 pixel area around the pixel of the ground station, we decided to take only one pixel to achieve a realistic error measure for the purpose of PV systems. This nowcasting aims to warn PV system

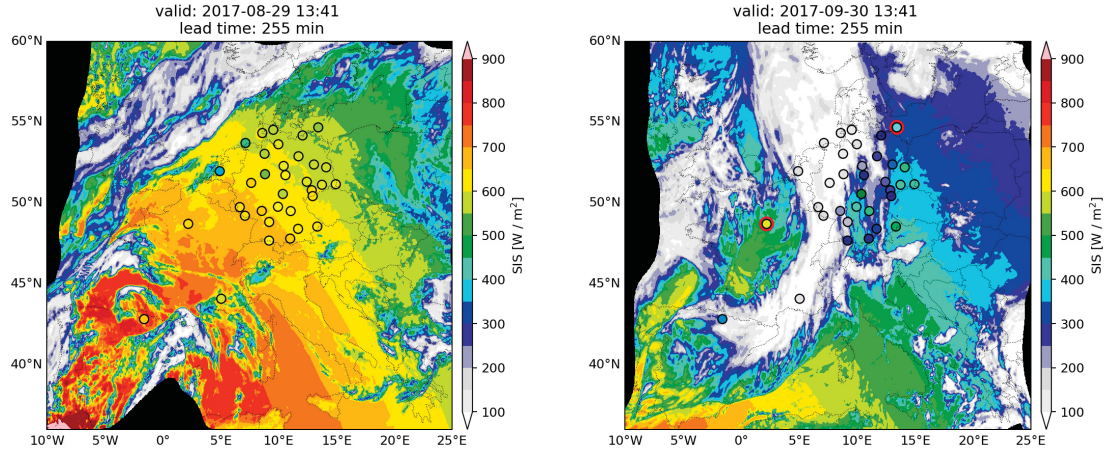

(a) Validation for 29 August 2017.

(b) Validation for 30 September 2017.

Figure 4.7: Validation of the solar surface irradiance nowcasting with ground stations by BSRN and DWD for 29 August 2017 (a) and 30 September 2017 (b). Depicted is the nowcasting of SIS as contour plot and the measured value of the ground stations is given in the black circles. The colorbar matches both figures. The forecast time equals 255 min. The red circles in (b) mark the stations Arkona and Palaiseau.

operators of grid instability and a realistic measure of the uncertainty of our forecast is essential. With the absolute difference of the nowcasting and the observation the root mean square error (black) and absolute bias (gray) were calculated (Figure 4.8(a)). We also calculated the respective relative errors by normalizing the absolute errors with the mean of the observed solar radiation at the surface that was measured by the pyranometers (Figure 4.8(b)).

The solar radiation of the nowcasting shows smaller values than the ground stations until approximately 250 min. Nevertheless, both the nowcasting and the observation show a similar behavior and a decrease of solar irradiance with increasing forecast time. The decrease of SIS can be observed due to the sunset and due to the fact that we work with products from the visible channel. The curves do not significantly differ from each other, which also results in small errors for the whole nowcasting. Furthermore the RMSE does not exceed 200 W/m^2. A slight maximum can be observed between 100 min and 200 min forecast time. The behavior of the error curves differs slightly from the RMSE and absolute bias in Figure 4.4 where the maximum is more distinct. Furthermore, the curve in Figure 4.4 shows less fluctuations but the height of the errors is on a comparable level. Nevertheless, the visual validation that can be seen in Figure 4.7 shows that the solar irradiation nowcasting matches most of the pyranometers. The relative errors in Figure 4.8(b) show the same behavior as the relative errors calculated for the validation with the SARAH-2 data in Figure 4.4. Until approximately 400 min, both the relative absolute bias and the relative RMSE increase with increasing forecast time. The relative RMSE reaches higher values after 400 min of forecast time because the majority of the stations measured 0 W/m^2, and certain stations did not measure any data at all. As a consequence, the stations that did measure solar radiation at the surface have a higher

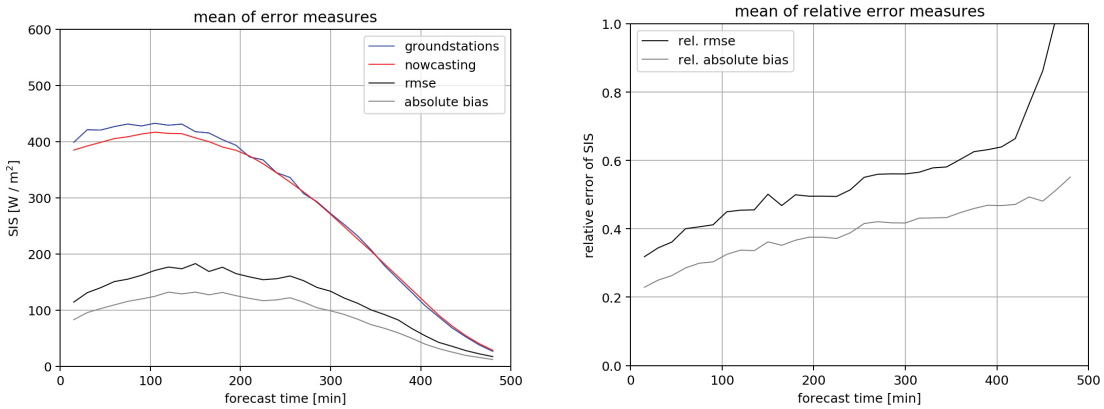

(a) Mean of absolute errors.

(b) Mean of relative errors.

Figure 4.8: Plots of the mean error measures of all cases against forecast time for absolute (a) and relative errors (b). The validation of the solar surface irradiance was performed with ground stations by BSRN and DWD.

impact on the result. This led to a higher difference between the nowcasting and the observation, which, after Equation (4.9), results in a higher relative RMSE, or even in values above 1. In addition to the rising errors after 400 min of forecast time, the height of the relative errors is in the same order as the relative errors from the SARAH-2 validation, which are displayed in Figure 4.4.

4.4 Discussion

In this work we presented many different validation methods to prove the quality of the SESORA forecast and to find out more about the errors that occur in our nowcasting.

The use of the visible channel of MSG leads to the issue that we cannot calculate motion vectors during the night. Since the SESORA forecast calculates the solar surface irradiance we are not interested in the night itself, however, it would be useful to be able to give a forecast for the early morning hours when the sun rises. This problem may be solved by a combination of the visible with the infrared channel. An advantage of the solar zenith angle dependency of SIS is that the SESORA forecast improves quantitatively when the sun sets because as the values of SIS decrease the errors of the nowcasting decrease as well. Due to this fact, NWP does not necessarily deliver better results after 4 h, when one looks at the results in the evening hours. Thus, the point of interception gets shifted back to longer forecast times. For 13 of the 17 cases discussed in this study, a comparison of the SESORA forecast with different NWP models and persistence has been performed within a master's thesis (Arndt, 2019). In this thesis it is shown that the point of intersection between our solar surface irradiance nowcasting and the IFS model forecast by the ECMWF (European Centre for Medium-Range Weather Forecasts) is 2:45 h with a deviation of 17 min for the RMSE (ECMWF, 2019). However, the intersection point with the NWP depends largely on the used model. For the ICON model by

the German weather service the intersection point is 4:32 h with a standard deviation of 58 min (Arndt, 2019). The nowcasting performs significantly better than persistence for all forecast scales, the margin rising with increasing forecast time. Figure 4.9 contains the results of the RMSE of the different forecasts averaged over 13 of the investigated test cases in this study. The relative errors of SIS increase with increasing forecast time, which is an expected behavior of all forecasts. This is of course important to evaluate the quality of the forecast however for the end users an absolute error is more useful. The users of the SESORA forecast are transmission and distribution system operators as well as direct marketers, and they may use it for trading and grid security, and in this case absolute errors are useful as they are more direct. All in all, both errors have advantages and disadvantages for each specific application.

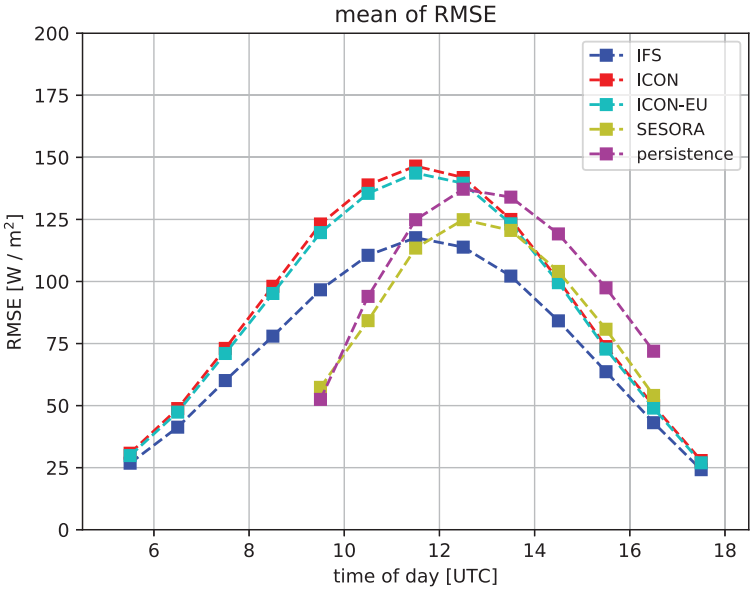

Figure 4.9: Plot of the mean of RMSE of SIS for 13 cases against the time of day. The comparison is shown for IFS by the ECMWF, ICON and ICON-EU by the German Weather Service, SESORA and persistence. The validation was performed with SARAH-2 data by the CM SAF. For SESORA and persistence the forecast was initiated at 09:15 UTC. They have a maximum lead time of 8 h. IFS is available every 12 h, ICON/ICON-EU every 3 h. It was taken from the model run, which would be available in reality, thus initiation time plus the time for the model run to finish (IFS takes 6 h; ICON/ICON-EU takes 3 h). Image adapted from Arndt (2019).

In the literature there are many possibilities of validating a solar irradiance nowcasting. Many approaches for such a nowcasting with the use of cloud motion vectors have been proposed (Escrig et al., 2013; Nonnenmacher and Coimbra, 2014; Schroedter-Homscheidt and Gesell, 2016; Gallucci et al., 2018; Sirch et al., 2017). A comparison with other studies is not always simple, as the region or the validation method can differ. Schroedter-Homscheidt and Gesell (2016) for example proposed a nowcasting for DNI over Spain and validated it by calculating the bias. After approximately 5 h the bias equaled 130 W/m^2. Nonnenmacher and Coimbra (2014) as well as Gallucci et al. (2018) used the RMSE as their validation method for the region of San Diego and Italy. After 2 h Nonnenmacher

and Coimbra (2014) got a RMSE of approximately 145 W/m^2 and Gallucci et al. (2018) mention a RMSE of 147 W/m^2. For the SESORA forecast we found a RMSE of 136 W/m^2 after 135 min over the area of Europe. In this comparison the area and the season play a major role so the three nowcastings are probably of similar quality. Another way of validating a nowcasting can be the probability of detection for a cloud mask. In our case we only distinguished between cloud and clear sky however Sirch et al. (2017). proposed a differentiation of upper and lower clouds (Sirch et al., 2017). They found a POD of 85–90% in dependency of the cloud type after 2 h over the area of Spain. The POD of the SESORA forecast after 135 min equals 84%, though our cloud mask is simply based on a effective cloud albedo threshold. Further, Sirch et al. (2017). performed a linear regression for DNI for the months March and July. R^2 equals 0.71 and 0.64 after 2 h while for our study R^2 is 0.72 after 135 min for SIS. Again, these comparisons are difficult and can only serve as a point of reference. All of the above discussed results can be found in Table 4.2.

Author	**Variable**	**Area**	**Measure**	**Lead Time**	**Value**
Schroedter-Homscheidt and Gesell (2016)	DNI	Spain	Bias	300 min	130 W/m^2
Nonnenmacher and Coimbra (2014)	GHI	San Diego	RMSE	120 min	145 W/m^2
Gallucci et al. (2018)	SIS	Italy	RMSE	120 min	147 W/m^2
this study	SIS	Europe	RMSE	135 min	136 W/m^2
Sirch et al. (2017)	DNI	Spain	POD	120 min	85–90%
this study	SIS	Europe	POD	135 min	84%
Sirch et al. (2017)	DNI	Spain	R^2	120 min	0.71
this study	SIS	Europe	R^2	135 min	0.72

Table 4.2: List of comparable results (DNI, GHI, SIS) with different error measures (RMSE, POD) from other publications and this study.

4.5 Conclusions and Outlook

In this work we presented a validation of a short-term forecast, also called nowcasting, based on the optical flow of effective cloud albedo for solar surface irradiance. The basis of our nowcasting works with the optical flow method TV-L^1 by OpenCV. The effective cloud albedo that can be retrieved by the reflectivity of the visible channel of MSG serves as input for our algorithm. As a result we have a field of cloud motion vectors that describe the apparent motion between two consecutive satellite images. These vectors are applied to the latter of the satellite images to create the first forecast step. The stage of applying the motion vectors can be repeated as often as desired to generate another forecast step. In that case the vectors are being applied to the latest available forecast step. Finally, by means of SPECMAGIC NOW the solar surface irradiance is calculated for every CAL forecast step to create the final SIS nowcasting.

We performed the validation with SARAH-2 data as well as with ground stations from the BSRN and the DWD. In both cases we calculated three different error measures, namely the bias, absolute bias, and root mean square error (Section 4.2.4) These error measures were calculated as absolute and relative errors respectively. All nowcastings shown in this study had a maximum forecast time of 480 min, which conflicts with the sunset. As a consequence the values of the solar surface irradiance, their absolute errors decreased with increasing forecast time. The maximum of the absolute bias and the RMSE can be found approximately after 180 min of forecast time if one considers Figure 4.4. If we look at the calculated values, which are available every 30 min due to the validation with the SARAH-2 data set we find the highest errors for 165 min. The absolute bias for 165 min equals 97 W/m^2 and the RMSE equals 142 W/m^2 for the same time. Relative errors are shown to grow with increasing forecast time and the maximum of the relative RMSE equals 0.41 after 480 min. A large issue with relative errors is high background radiances. As a consequence, resulting errors could be higher than large relative errors of low background radiances. Thus, even a small relative error could have an impact on the grid stability in that case where the forecast error affects a large number of photovoltaic systems. However, the SESORA forecast works best for high pressure system situations when there are only a few clouds and the solar irradiance is high (Figure 4.3). Therefore, the risk of providing a bad forecast for the TSOs and DSOs is rather small. Moreover, the biggest errors are caused by convection but convective cells are rather local phenomena and it is very unlikely that enough photovoltaic systems are simultaneously affected by this type of error in Germany, that they would induce grid instability. Furthermore, after the SPECMAGIC NOW update the constant bias of solar irradiance should be significantly lower due to corrections in the clear sky calculation. For the upcoming merge with the NWP, a quality check is planned to determine the intersection point with the nowcasting. Thus, if the errors of the nowcasting will actually rise too quickly the merge with the NWP will be performed earlier to prevent large forecast errors and as a consequence of grid instability. Absolute errors of the effective cloud albedo rise as well as the relative errors of solar irradiance with increasing forecast time. The results for the validation with ground stations showed similar results with slightly higher errors (relative RMSE ≈ 0.6 after 480 min). The linear regression proved the bias of ≈ -25 W/m^2 found in the validation with the SARAH-2 data. There is a planned update of SPECMAGIC NOW that should reduce this bias by adapting the optical thickness of clouds. By reducing the systematic error of the SESORA forecast the overall results will improve. Errors that occur due to the optical flow method TV-L^1 cannot be corrected as easily. The effect of growing errors with increasing forecast time is represented by the spread of the data points in the regression. Furthermore, the effect of the sunset can be corrected by the cosine of the solar zenith angle. This correction also improved the quality of the forecast as can be seen in the increased R^2 value. Overall, the results appear promising and the errors of the examined cases are small. The largest errors occur at cloud edges or in the case of formation or dissipation of clouds. Since the algorithm of our nowcasting is built on extrapolation it neglects convective or dissipative processes.

Future work can implement features that allow curved trajectories for cloud pixels. Moreover these features could allow the formation and dissipation of clouds by taking into

account changing intensities in the optical flow estimation. For both additions it is necessary that the optical flow method uses more than two satellite images. Therefore, we will adjust the algorithm such that multiple frames will serve as import data in the optical flow method to allow a longer history of cloud movements. Another aim of ours is the use of the NWP for later hours of our nowcasting where a merge between these two is planned in the range of an intersection point. The transition of the higher forecast quality from the nowcasting to NWP depends on the weather situation, initiation time and maybe other parameters. However, in our opinion the point of intersection between the sinking quality of the nowcasting and the increasing quality of the NWP would probably lie between 3 to 4 h. After that, the loss of details due to the optical flow method becomes too high and the NWP might deliver better results. With a merge between the nowcasting and the NWP we would develop a seamless product that always uses the best available forecast at each time step for a 12 h solar surface irradiance forecast. Some leading experts like Lorenz and Wolff have already shown that seamless products deliver even better results than the NWP after the point of intersection as the combination leads to an improvement of the forecast quality (Lorenz et al., 2012; Wolff et al., 2016). Thus, the final product would not only be seamless but it would also show a higher quality than single forecast products.

The software of SPECMAGIC NOW, as well as the optical flow method TV-L^1, are both open source. This validation study works as an indication for future works of other scientists to use one or both parts for their own research. This way, PV forecasts can simply be constructed out of smaller software blocks and adjusted to the needs of the operator.

Funding

This research was funded by Gridcast, a project by the Federal Ministry for Economic Affairs and Energy (Bundesministerium für Wirtschaft und Energie, BMWi).

Acknowledgments

We thank Jörg Trentmann and Uwe Pfeifroth for providing the SARAH-2 and BSRN data for our validation. Thanks to Michael Mott, Manuel Werner and Nils Rathmann for the introduction and support regarding the POLARA framework, which was developed by the department of radar meteorology at the German Weather Service.

Chapter 5

Development of a seamless forecast for solar surface irradiance using ANAKLIM++

Isabel Urbich[1], Jörg Bendix[2] and Richard Müller[1]
[1] Deutscher Wetterdienst, Frankfurter Straße 135, 63067 Offenbach, Germany
[2] University of Marburg, Faculty of Geography, Deutschhausstraße 12, 35032 Marburg, Germany

This chapter was submitted to Solar Energy,
Received: 29 September 2020;

Abstract

A novel approach for a blending between nowcasting and numerical weather prediction (NWP) for the solar surface irradiance (SIS) for a forecast horizon of 1–5 h is presented in this study. The blending is performed with a software tool called ANAKLIM++ (Adjustment of Assimilation Software for the Reanalysis of Climate Data) which was originally designed for the efficient assimilation of two-dimensional data sets using a variational approach. A nowcasting for solar surface irradiance was already presented and validated in earlier publications as seamless solar radiation forecast (SESORA). For our blending two NWP models namely the ICON (Icosahedral Non-hydrostatic model) from the German weather Service (DWD) and the IFS (Integrated Forecasting System) from the European Centre for Medium-Range Weather Forecasts (ECMWF) were used. The weights for the input data for ANAKLIM++ vary for every single forecast time and pixel depending on the error growth of the nowcasting. The results look promising since the root mean square error (RMSE) and mean absolute error (MAE) of the blending are smaller than the error measures of the nowcasting or NWP models, respectively.

Zusammenfassung

In dieser Studie wird ein neuartiger Ansatz für eine Kombination aus Nowcasting und numerischer Wettervorhersage (NWV) für die solare Einstrahlung am Boden für einen Vorhersagehorizont von 1–5 h vorgestellt. Das Blending wird mit einem Software-Tool namens ANAKLIM++ (Adjustment of Assimilation Software for the Reanalysis of Climate Data) durchgeführt, das ursprünglich für die effiziente Assimilation zweidimensionaler Datensätze unter Verwendung eines Variationsansatzes entwickelt wurde. Ein Nowcasting für die Globalstrahlung wurde bereits in früheren Publikationen als SESORA vorgestellt und validiert. Für unser Blending verwendeten wir zwei NWV-Modelle, nämlich das ICON (Icosahedral Non-hydrostatic model) des Deutschen Wetterdienstes (DWD) und das IFS (Integrated Forecasting System) des Europäischen Zentrums für mittelfristige Wettervorhersagen (ECMWF). Die Gewichte für die Eingangsdaten für ANAKLIM++ variieren für jede einzelne Vorhersagezeit und jedes einzelne Pixel in Abhängigkeit vom Fehlerwachstum des Nowcastings. Die Ergebnisse sehen vielversprechend aus, da der mittlere quadratische Fehler (RMSE) und der mittlere absolute Fehler (MAE) des Blendings kleiner sind als die Fehlermaße des Nowcastings bzw. der NWV-Modelle.

5.1 Introduction

The contribution of photovoltaic (PV) power to the electricity mix increased significantly over the last decades in accordance with the overall importance of renewable energies (Lorenz et al., 2012; Fraunhofer ISE, 2020). Due to the rapid installation of solar power worldwide and the integration of fluctuating PV power into the grid, spatially and temporally high resolved solar irradiance forecasts are strongly required (Huang et al., 2018). It is therefore essential for management and operation strategies that solar irradiance forecasts deliver reliable predictions of the expected PV power for the next 0–12 h. (Lorenz et al., 2012; Raza et al., 2016; Inman et al., 2013; Vrettos and Gehbauer, 2019; Barbieri et al., 2017).

Usually, a nowcasting (NWC) covers the first few hours of forecast due to its higher temporal and spatial resolution (Lorenz et al., 2012; Wolff et al., 2016; Kurz, 2018; Arndt, 2019). However, observation based forecasts are known for their rapid error growth (Huang et al., 2018; Kilambi and Zawadzki, 2005; Yang et al., 2019). Therefore, numerical weather prediction (NWP) is used after the first couple of hours because of their ability to explicitly and systematically simulate atmospheric processes and their evolution at larger scales (Perez et al., 2010; Aguiar et al., 2016; Nonnenmacher and Coimbra, 2014). Thus, to enable a seamless solar radiation forecast for transmission and distribution system operators as well as direct marketers it is crucial to design a suitable blending of NWP and nowcasting. For renewable energies in general, blendings of different forecasts have been identified as a great possibility for improving the forecast quality for wind velocity as well as solar radiation (Huertas-Tato et al., 2020; Tascikaraoglu and Uzunoglu, 2014; Tuohy et al., 2015). It is not uncommon that combined products outperform all

individual forecast products for the entire forecast horizon since a blending takes advantage of their synergies and complementaries (Huertas-Tato et al., 2020; Bowler et al., 2006; Wolff et al., 2016). The approaches for blending multiple forecasts are numerous. A common established technique are artificial neural networks (NN) (Mellit and Pavan, 2010; Rehman and Mohandes, 2008; Bosch et al., 2008; Sfetsos and Coonick, 2000; Ghanbarzadeh et al., 2009; Mohandes et al., 1998; Marquez et al., 2013). One reason for the popularity of NN is the opportunity to integrate PV energy yields into the forecast of PV power, without the need to simulate them, e.g. Wolff et al. (2016). Besides that, the resulting hybrid of several NWP models and satellite measurements has the ability to improve the quality of single forecasts of solar surface irradiance (SIS) as Marquez and Coimbra (2011) demonstrated. Other successful techniques for time series prediction approaches are fuzzy models (Boata and Gravila, 2012), adaptive neuro-fuzzy interference systems (Moghaddamnia et al., 2009), autoregressive models (Bacher et al., 2009; Dambreville et al., 2014), multiplicative autoregressive moving-average statistical models (Mora-Lopez and Sidrach-de Cardona, 1998), hidden Markov processes (Hocaoğlu, 2011), multi-dimensional linear prediction filters (Akarslan et al., 2014), multi-model-mix of diverse forecasting approaches (Sanfilippo et al., 2016) and using the Weather Research and Forecasting model (WRF) to advect and diffuse Meteosat Second Generation (MSG) cloud index values (Arbizu-Barrena et al., 2017). Wolff et al. (2016) compared a support vector regression with the linear regression of persistence, nowcasting and NWP by Kühnert (2016) and both methods performed very similarly. Besides that, like most of the blending approaches the combined forecast could outperform each individual forecast product. Kühnert (2016) utilized a combination of the COSMO (Consortium for small-scale Modeling) model from the German Weather Service (DWD) and IFS (integrated forecasting system) from the ECMWF (European Centre for medium-range Weather Forecasts) for the NWP share in his regression. The mean RMSE (root mean square error) of the installed power for all stations in Germany was approximately 3% after 4 h and Kühnert (2016) showed that the quality of the combined forecast can be significantly improved when the weighting parameters are selected day-time-dependent. A similar approach was presented by Lorenz et al. (2012) for solar irradiance where they performed a linear regression of COSMO, IFS and a nowcasting with the aim to develop a seamless transition between those forecasts. For a validation period of 9 months including nights the RMSE was approximately 26 W/m^2 after a forecast horizon of 4 h. Haupt et al. (2016) work on a blending system which performs a bias correction of the utilized models in a first step and after that optimizes the blending weights for each lead time according to their historical performance. This intelligent consensus forecast represents the NWP share which is later blended linearly with a nowcasting for the time period of 3–6 h (Myers et al., 2011; Haupt et al., 2018). The mean absolute error (MAE) of this hybrid method is dependent of the season and it ranges from 30 W/m^2 in January and February up to approximately 90 W/m^2 in May and June after 4 h respectively. Martínez Sánchez and Callado (2019) are also using a linear transition for the combination of the nowcasting and the NWP model of the Spanish Weather Service between 0–4 h. After 4 h the relative RMSE for the global horizontal irradiance (GHI) equals 22% and 46% for the direct normal irradiance (DNI). With their optimum mix of satellite-derived cloud motion forecasts, the National Digital Forecast Database's (NDFD) cloud cover-derived

irradiance forecasts and several operational numerical weather prediction models, Perez et al. (2014) reported a relative RMSE of approximately 22% for GHI after a lead time of 5 h.

However, the methods discussed so far are driven by optimization of blending techniques instead of meteorology. Thus, in this study we investigate a method which allows a blending depending on the regional weather situation aiming for a seamless temporal and spatial prediction. For this purpose, a novel approach for blending an satellite-based nowcasting with two NWP models, namely ICON (Icosahedral non-hydrostatic model) and IFS (Reinert et al., 2018; ECMWF, 2019), using a software tool called ANAKLIM++ (Adjustment of Assimilation Software for the Reanalysis of Climate Data). It combines methods from data assimilation with Gaussian weights thus it can be extremely helpful for blending purposes in the scope of seamless forecasting. Originally ANAKLIM++ was designed for the efficient assimilation of two-dimensional data sets using a variational approach (Groß et al., 2014a,b). The aim of ANAKLIM++ was to assimilate NWP data, satellite data and ground measurements to obtain climate data sets of solar surface irradiance without data gaps. As for the nowcasting of solar surface irradiance presented in Urbich et al. (2019) the region of interest for the combined forecast is central Europe. ANAKLIM++ combines the nowcasting of solar surface irradiance presented in Urbich et al. (2019) with two NWP models for the forecast horizon of 1–5 h aiming for seamless temporal and spatial transition. The resulting integrated forecasts are validated with SARAH-2 data from the Satellite Application Facility on Climate Monitoring (CM SAF). As error measures the bias, MAE and RMSE are calculated for a series of selected cases in August, September and October 2017. These cases were selected due to their different weather situation over central Europe because clouds play a dominant role in solar irradiance forecasts. Further, the performance of the blending with ANAKLIM++ is compared to a simple approach with a weighted mean.

In the following section, the utilized data which serves as input for the software tool ANAKLIM++ will be described. The data of both NWP models will be described in section 5.2.1, while more information about the nowcasting can be found in section 5.2.2. A description of the used reference data will follow in section 5.2.3. The methodology of ANAKLIM++ (section 5.3.1), a simple blending approach (section 5.3.2) and the error measures used for the validation (section 5.3.3) are explained in section 5.3. After that, in section 5.4, the results of the blending and the corresponding validation of the forecast are displayed and discussed.

5.2 Data

In the following the data utilized for ANAKLIM++ are described in more detail. For a blending with ANAKLIM++ N different two-dimensional data sets can be used as input. In order to be consistent with earlier publications (Urbich et al., 2018, 2019) we examined a set of fifteen cases based on different weather situations for the months of August, September and October 2017. A list of these cases can be found in the Appendix in Table A.7. The diversity of the selected weather situations in this study

cover the relevant cloud types for PV forecasting in Central Europe.

Product	Method	Operator	Horizontal Resolution	Temporal Resolution
NWC	Short-term Forecast	DWD	5 km	15 min
ICON	Numerical Weather Prediction	DWD	13 km	1 h
IFS	Numerical Weather Prediction	ECMWF	9 km	1 h
SESORA	Blended Forecast	DWD	5 km	1 h

Table 5.1: Information on the forecasted solar surface irradiance data used in this study.

5.2.1 Numerical Weather Prediction

For the blending with ANAKLIM++ two state of the art global NWP models, the ICON from the DWD and the IFS from the ECMWF were selected.

ICON is the global and regional model of the DWD. The horizontal grid consists of a set of spherical triangles that seamlessly span the entire globe (Reinert et al., 2018). The horizontal resolution equals 13 km for the global and 6.5 km for the regional nest. Main runs are initialized four times a day at 00, 06, 12 and 18 UTC for the whole region up to 120 h and additional four times at 03, 09, 15 and 21 UTC with the EU (Europe) nest up to 30 h (Reinert et al., 2018). The runtime of ICON is approximately 3 h. SIS is given as accumulated solar radiation over several hours depending on the time of initiation in W/m^2. These accumulated values of SIS are recalculated as hourly averaged values to be similar to the other utilized forecasts. For this study, the global version of ICON is used because the higher resolved ICON-EU did not lead to better validation results in particular compared to IFS (Arndt, 2019; Urbich et al., 2019). A detailed list of all used forecasting products can be found in Table 5.1.

IFS is the global NWP model of the European Center for Medium Weather Forecast (ECMWF). The deterministic run of the IFS comes with a horizontal resolution of 9 km and is performed twice daily with initial times 00 and 12 UTC (ECMWF, 2019). The runtime of the IFS is approximately 6 h. The solar surface irradiance is given in hourly accumulated values in J/m^2. However, for this study all results were recalculated into hourly averages in W/m^2 to be comparable with ICON and the nowcasting.

For this study only used those model runs are used that would be actually available in an operational service. Hence, the different runtimes of IFS (6 h) and ICON (3 h) were considered for the selection of the forecast. A complete ICON run is available every 3 hours whereas IFS runs are available at 06 and 18 UTC. Thus, for this study the 06 UTC run from ICON and the 00 UTC run from IFS are taken since the blending of all example cases will always start at 10 UTC.

Since the horizontal resolution of the NWP models does not equal the resolution of the nowcasting both NWP models are interpolated into spacial grids of 0.05° before blending all data sets as it was also done by Mathiesen and Kleissl (2011). The interpolation is performed with a nearest-neighbor-method. By doing this we take the maximum advantage out of the higher resolved nowcasting and besides that it is well known that

grid spacing employed by NWP alone does not have a significant impact on the accuracy of solar irradiance forecasts (Huang and Thatcher, 2017).

5.2.2 Nowcasting

The solar surface irradiance nowcasting used for this study has already been presented and validated in two previous publications as SESORA (seamless solar radiation forecast) (Urbich et al., 2018, 2019). It is based on the optical flow of the effective cloud albedo derived from the visible channel of MSG. The utilized method TV-L^1 from the open source library OpenCV (2020) (Open Source Computer Vision Library) uses a multi-scale approach to capture cloud motions on various spatial scales. After the clouds are displaced solar surface irradiance is being calculated by SPECMAGIC NOW (Spectrally-resolved mesoscale atmospheric global Irradiance Code for Nowcasting). This algorithm by Müller et al. (2012) calculates global irradiation spectrally resolved from satellite imagery. As the effective cloud albedo, the nowcasting of the solar surface irradiance is available every 15 min with a horizontal resolution of 0.05°.

As a preparation for the blending with ANAKLIM++ the hourly means were calculated. A very specific feature of the optical flow is the inward moving edge upstream of the cloud movement. Due to the fact that the method works without any kind of boundary conditions the area behind the displacement contains no data. Like all pixels without data this area is marked in white (Figure 5.2(c) and 5.2(d)). However, this area can be filled again with values in the process of the blending with ANAKLIM++.

5.2.3 Reference Data

For the validation of all forecasts used in this study data from the CM SAF were used. Their solar surface irradiance data from the SARAH-2 data set is the latest CM SAF climate data record of surface radiation based on the geostationary Meteosat satellite series (Pfeifroth et al., 2018). The area covered by SARAH-2 spans from -65° to +65° in latitude and longitude with a spatial resolution of 0.05°. The high quality of SARAH-2 in reference to the Baseline Surface Radiation Network (BSRN, 2020) data is documented in Pfeifroth et al. (2017).

5.3 Method

In this section a brief overview of the blending method ANAKLIM++ and of the configurations utilized for this study is given. Moreover the method of validation is described in this section.

5.3.1 ANAKLIM++

The aim of ANAKLIM++ is to assimilate multiple two-dimensional data sets to get a result that is closest to reality and has no missing data (Groß et al., 2014b). A general

solution for a combination of N two-dimensional data fields e.g. weather forecasts is to build the mean of these forecasts. A more sophisticated combination can be obtained by calculating a weighted mean

$$z(x) = \frac{\sum_l^N G_l(x) p_l(x)}{\sum_l^N G_l(x)} \tag{5.1}$$

with a real-valued function $p_l(x)$ and a weighting function $G_l(x)$ where $l \in [0, N-1]$ (Groß et al., 2014a). To find a new data set $z(x)$ which is similar to the input data $p_l(x)$ the minimum of

$$L(z(x)) = \sum_{l=0}^{N-1} G_l(x)(p_l(x) - z(x))^2 \tag{5.2}$$

has to be found. This further leads to solving the following equation:

$$0 \stackrel{!}{=} \frac{\partial}{\partial z(x)} L(z(x)) = \sum_{l=0}^{N-1} G_l(x) p_l(x) - z(x) \sum_{l=0}^{N-1} G_l(x). \tag{5.3}$$

This condition can be expanded with an additional term to penalize artifacts and large gradients and yielding smoother results. With λ being a Lagrangian multiplier this finally leads to

$$L(z(x), \nabla z(x)) = \sum_{l=0}^{N-1} G_l(x)(z(x) - p_l(x))^2 + \lambda \left\| \nabla z(x) \right\|^2. \tag{5.4}$$

By using the Euler-Lagrange-formalism the minimization of the above can be transformed into a sparse system of linear equations, which can further be solved by a conjugate gradient solver (Groß et al., 2014b).

As stated in section 5.2.1, only those SIS forecasts are used for a blending, which would also be available for the operational service. For a better overview over the available data a scheme of the temporal procedure can be found in Figure 5.1. The required input data for ANAKLIM++ are the hourly averaged solar surface irradiance of ICON, IFS, nowcasting and a reference, respectively. Since the reference is the analysis of our nowcasting both are available every 15 min. They are being recalculated into hourly averaged values for the blending. Thus, the first blending will be done after 1 h of nowcasting. Both NWP models are available every hour. The lead time of them depends on the initiation time and the runtime (section 5.2.1).

A simple blending with a weighted mean can only use the same weighting for each pixel in the data. A more sophisticated meteorological approach should be able to consider local weighting dependent on the regional weather, which in turn defines the quality of the forecasts. In order to meet this issue a key feature of ANAKLIM++ can be used. ANAKLIM++ was originally intended to fill gaps of missing satellite data. To make use of this feature, regions with rapid error growth can be detected in the analysis and the respective regions can be cut out of the nowcasting if the errors exceed a certain threshold. To locate those regions the analysis of the nowcasting hence the 0-min-forecast is compared to the 60-min nowcasting and the absolute difference between these data

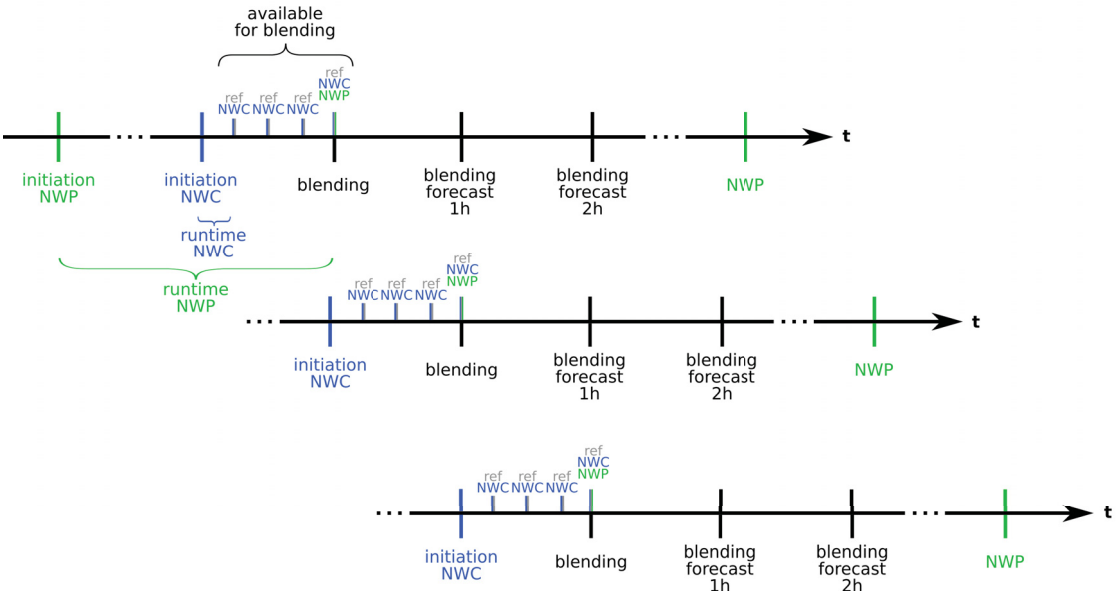

Figure 5.1: Scheme of the temporal availability of the input data for a blending with ANAKLIM++. The distance of the depicted forecasts is proportional to the time range in which they are available. The dots on the line mark a break in the time line due to a changing temporal availability and differing runtimes of the utilized NWP models. For each blending 1 h of NWP, NWC and reference need to be available. The procedure can be repeated every hour.

fields is calculated. For the first blending all values over the 90th percentile of the absolute difference are cut out and filled by ANAKLIM++ with data from ICON and IFS. For further blending forecasts the percentile becomes lower and the cropped area becomes larger. In this manner, the weight of the nowcasting is depressed for e.g. convective weather situations which cannot be captured by pure advection of TV-L^1 but still used with full weight for weather situation characterized by pre-dominantly advective cloud movements. For these advective weather situations a nowcasting outperforms NWP for several hours. See Urbich et al. (2019) for further discussions on the relation between weather and nowcasting errors. This approach is used to allow a conservative forecast of the cut out areas since we will never exactly know where errors of the nowcasting will occur. So far we know that especially regions with forming or dissolving clouds e.g. convection cause problems to the optical flow method (Urbich et al., 2018, 2019). However, to not just ignore the cut out values they are utilized in an additional lower weighted layer in ANAKLIM++ from here on called inverse layer. This way, potential errors will be penalized but valuable pixels can still have their impact on the resulting product. In the remaining area ANAKLIM++ builds a weighted mean between all possible data sets thus nowcasting, IFS and ICON.

Under all possible configurations in ANAKLIM++ we think that the Lagrangian weights are the most practicable adjusting screw for our purpose. ANAKLIM++ provides the opportunity to choose Lagrangian weights for the similarity operator itself and for its first and second derivative (Groß et al., 2014a). Thus, only weights for the similarity operator itself were chosen and varied for each forecast time. A list of the chosen Lagrangian

Product	Lead Time (h)				
	1	2	3	4	5
SIS NWC with gaps	0.75	0.55	0.35	0.15	0
SIS NWC inverse	0.05	0.10	0.15	0.20	0.25
IFS	0.15	0.25	0.35	0.45	0.50
ICON	0.05	0.10	0.15	0.20	0.25

Table 5.2: Lagrangian weights for the blending with ANAKLIM++ for the nowcasting with gaps and its corresponding inverse layer (only content of gaps) and for the NWP models IFS and ICON respectively.

weights for ANAKLIM++ can be found in Table 5.2. The blending starts with a large share of nowcasting and fades out slowly while the shares of IFS and ICON slowly increase. The inverse layer of the nowcasting with gaps thus only the content which was cut out is used, also. However, the inverse layer is utilized with lower weights so that the sum of the Lagrangian weights of both layers slowly decreases. As a result, areas where errors are more likely to rise are penalized but the information of the troubled areas can be still used.

5.3.2 Simple Blending

To be able to evaluate the quality of a blending of NWP and nowcasting by the means of ANAKLIM++ a simple blending is performed for comparison. For this purpose the original nowcasting without holes and the IFS is used. With those two data sets a weighted mean of SIS is built for up to 4 h of forecast time. For the first hour the nowcasting gets weighted with 80% and the weight decreases further until it reaches 0% while for IFS it is the other way around.

5.3.3 Error Measures

The solar surface irradiance of all forecast products was verified in the same manner. In a first step the absolute difference between the forecast and SARAH-2 was determined. After that, the bias

$$\text{bias} = \frac{1}{n}\sum_{i=1}^{n}(x_i - y_i)\,, \tag{5.5}$$

mean absolute error (MAE)

$$\text{MAE} = \frac{1}{n}\sum_{i=1}^{n}|x_i - y_i|, \tag{5.6}$$

and root mean square error (RMSE)

$$\text{RMSE} = \sqrt{\frac{1}{n}\sum_{i=1}^{n}(x_i - y_i)^2} \tag{5.7}$$

were calculated. We decided to work with these error metrics since they are used most commonly in the scope of energy meteorology and solar irradiance forecasting (Sengupta et al., 2015). The spread of the mean error metrics of all investigated cases is captured by means of the empirical or sample variance v

$$v = \frac{s^2}{\bar{x}}. \tag{5.8}$$

Here, $\bar{x}$ is the mean

$$\bar{x} = \frac{1}{n}\sum_{i=1}^{n} x_i \tag{5.9}$$

and s represents the standard deviation

$$s = \sqrt{\frac{1}{n-1}\sum_{i=1}^{n}(x_i - \bar{x})^2} \tag{5.10}$$

of x_i.

5.4 Results

15 cases with different weather situations were examined for the months of August, September and October 2017 (section 2). For the sake of clarity the effect of the blending on the SIS structures is discussed based on two vivid examples in Figure 5.2 and Figure 5.3. The overall results, showing the average of the bias, MAE and RMSE for all cases will be presented in Figure 5.4.

Figure 5.2 shows the hourly averaged solar surface irradiance for 7 August 2017 11 UTC. In Figure 5.2(a) the result from the ANAKLIM++ blending with a lead time of 60 min is presented and Figure 5.2(b) shows the respective result of the reference data SARAH-2. An example of the hourly averaged nowcasting with and without data gaps where regions with high potential of significant error growths were detected is shown in Figure 5.2(c) and 5.2(d). Figures 5.2(e) and 5.2(f) depict the results from the NWP models IFS and ICON.

The resulting blending in Figure 5.2(a) still shows the large structures from the nowcasting with a slight adaption of the amplitude of the solar surface irradiance. In this case ANAKLIM++ led to a better forecast of solar surface irradiance according to the reference data. Further changes also appeared in the area around the Mediterranean sea where the nowcasting shows quite high values of SIS (> 900 W/m^2) in the forecast. Especially IFS has lower values of SIS throughout a larger region. A blending which is more or less a weighted mean therefore leads to a medium result which for this example lies closer to the reference data as well. A further advantage of ANAKLIM++ is that it refills the missing data of the inward moving edge in our nowcasting with appropriate data of the NWP models.

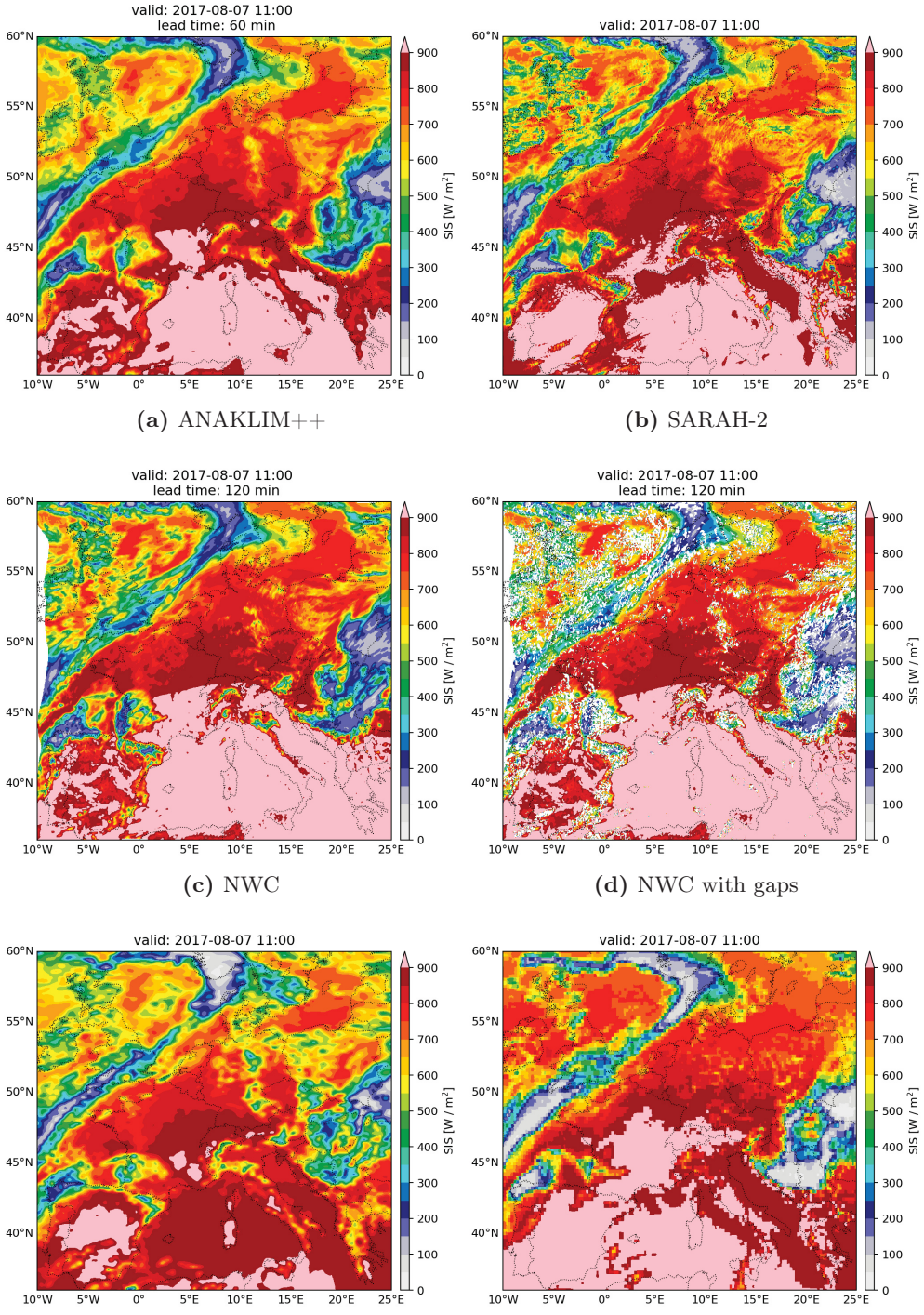

(a) ANAKLIM++ **(b)** SARAH-2

(c) NWC **(d)** NWC with gaps

(e) IFS **(f)** ICON

Figure 5.2: Hourly averaged solar surface irradiance of (a) the blending with ANAKLIM++, (b) SARAH-2, (c) NWC, (d) NWC with data gaps, (e) IFS and (f) ICON for 2017-08-07 11 UTC, respectively.

Another example of a blending of NWP and nowcasting utilizing ANAKLIM++ is presented in Figure 5.3 for 30 September 2017 11 UTC. The results of the blending are depicted in Figure 5.3(a) with a lead time of 60 min while Figure 5.3(b) shows the solar irradiance of the reference data from SARAH-2. The corresponding input data (nowcasting, IFS and ICON) can be seen in the Figures 5.3(c)–(e).

A very similar behavior as for the other case can be recognized in the example of 30 September 2017 in Figure 5.3(a). The overall structure of the frontal region looks very much like the structure of the front in the SIS nowcasting. Both NWP models predict a smaller shape of the front. Nevertheless, the SARAH-2 data in Figure 5.3(b) shows a frontal structure just like the one of the blended forecast. Here, the outer structure of the front is taken from the nowcasting while the inner structure is a result of all the input data. Over the North Sea behind this front there is a small region where SARAH-2 shows optically thinner clouds. This feature cannot be recognized in the nowcasting since this area shows thicker clouds, however it is visible in the blending. This seems to be a result of the impact of ICON and IFS.

After discussing the effect of the ANAKLIM++ blending on the SIS structures based on for two illustrative cases the validation results for all examined cases will be discussed. Further, the ANAKLIM++ blending will be contrasted with a simple blending approach (section 5.3.2), with persistence, with the nowcasting, and with ICON and IFS. The results of this validation are displayed in Figure 5.4.

Figure 5.4(b) and 5.4(c) show the mean RMSE and mean absolute bias of all examined cases in dependency of the time of day. However, the time of day does not equal the lead time of these forecasts. As already mentioned in section 5.2.1 only those model runs were used that would be available for a blending at 10 UTC, therefore the 06 UTC run from ICON and the 00 UTC run from IFS are used. Moreover, the nowcasting and the persistence started at 09 UTC because one hour of solar surface irradiance is needed as input. For better understanding the reader may want to look at the scheme of the temporal availability of the different data sets in Figure 5.1. Figure 5.4(b) and 5.4(c) show the error measures for a version of the blending where the nowcasting with data gaps is used. Both look quite similar because the RMSE and MAE of the blending with ANAKLIM++ are the lowest of all forecasts throughout the entire validation horizon. It is also similar in both figures that ICON shows the highest errors at the beginning and towards the end of the blending the persistence forecast has the highest errors. Moreover, the performance of both NWP models is slightly improving with forecast time while the errors of the nowcasting and persistence slowly increase. A little surprise is that a simple blending approach can outperform the other forecasts. After a forecast time of 4 h the difference between ANAKLIM++ and the simple approach becomes slightly larger but all in all both blendings improved the quality of each forecast before the blending. Another similar behavior is that both error measures show a decrease for all forecasts towards longer lead times which is owed to the sunset. In Urbich et al. (2019), it was already proved that this behavior is related to the sunset since relative error measures did not decrease in the same manner. Figure 5.4(a) also depicts the RMSE of all examined cases. In addition, this figure shows the results of a blending utilizing ANAKLIM++ where the nowcasting data was used completely therefore no regions were cut out, see

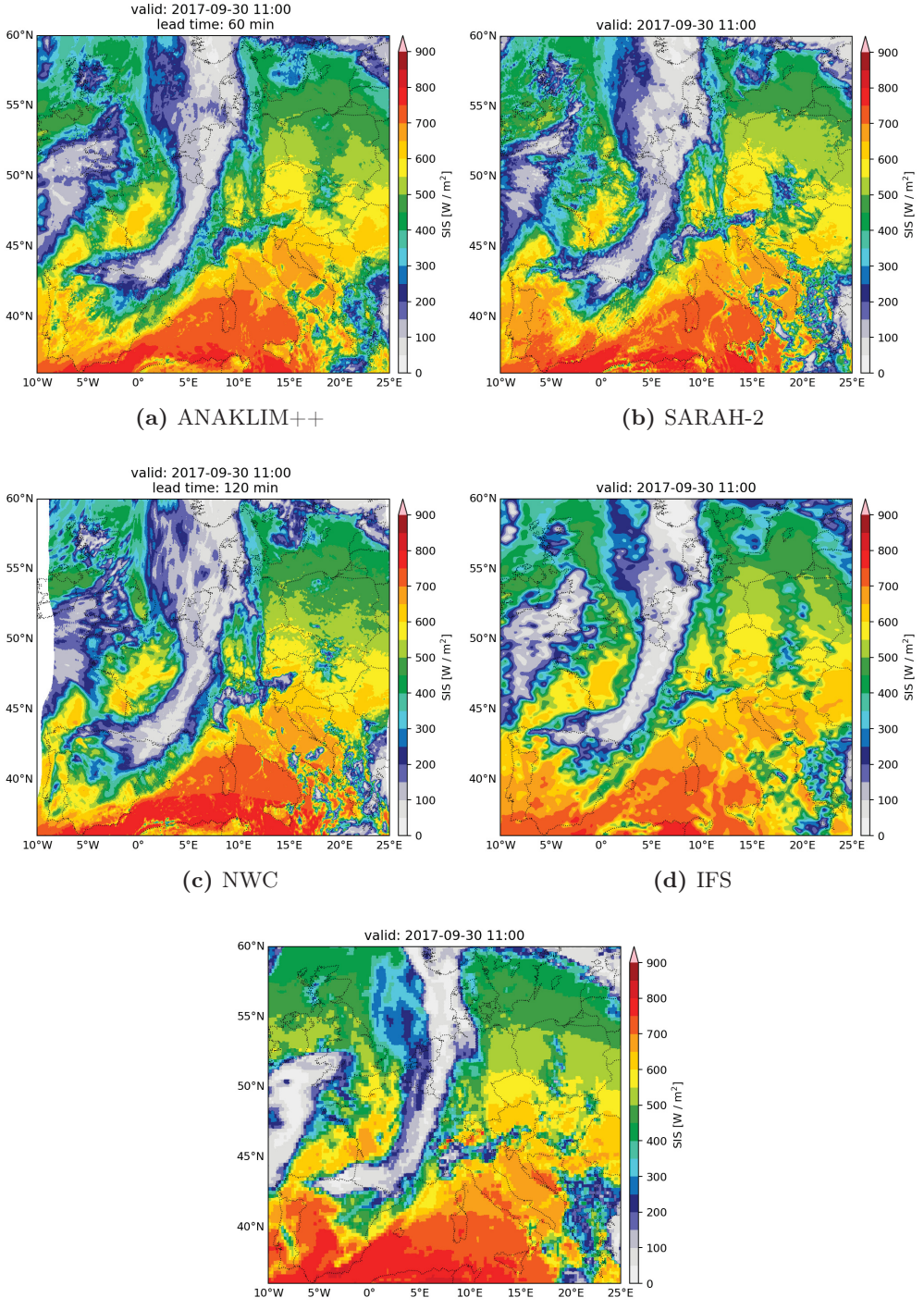

(a) ANAKLIM++ **(b)** SARAH-2

(c) NWC **(d)** IFS

(e) ICON

Figure 5.3: Hourly averaged solar surface irradiance of (a) the blending with ANAKLIM++, (b) SARAH-2, (c) NWC, (d) IFS and (e) ICON for 2017-09-30 11 UTC, respectively.

Figure 5.2(c) in comparison to Figure 5.2(d) for further details. This comparison shows that the approach of error filtering leads to a significant improvement (lower RMSE) after approximately 2 h forecast time when errors in the nowcasting get bigger and larger parts are being cut out in the version with data gaps. Simultaneously the quality of the NWP models increases especially in comparison to the nowcasting. Therefore a blending with gaps in the nowcasting data in regions with high potential of errors can lead to lower error measures. To assess the quality of forecasts in the scope of energy meteorology it is crucial to consider the error spread as well. A low error can be misleading that the overall forecast quality is high for all weather situations. However, a misinterpretation of the forecast due to lack of information can affect grid stability. The error bars in Figures 5.4(a)–(c) depict the empirical variance v (Equation (5.8)) thus it represents the spread of the error measures of the investigated cases. Since the simple blending utilizes only IFS for a lead time of 5 h both forecasts will always have the same size of error and variance. All forecasts show a rising spread with increasing lead time. Further, the spread of ANAKLIM++ is smaller than that of the simple blending for all presented error metrics.

Another error measure is presented in Figure 5.4(d). Here, the mean bias of all cases is plotted against time for the version with gaps. The bias of the shown solar surface irradiance forecasts reveals among other things why both blendings which where analyzed in this study performed better than all other forecasts individually. After calculating the weighted mean in both blendings the chosen input data has such an impact on the results that both lie closer to the reference data SARAH-2. Due to an overestimation of SIS in ICON and an underestimation of SIS in IFS and the nowcasting even a simple blending of those three forecasts can improve the quality of the blended forecast from the first hour. Figure 5.4(d) can also deliver a deeper understanding of the individual shares of each forecast for the blending method. For the nowcasting a bias was found which was already discussed in Urbich et al. (2019). Together with the knowledge that the RMSE of the nowcasting grows with increasing forecast time (Figure 5.4(b)) it seems reasonable to reduce the share of the nowcasting with time. Moreover, it appears that for a successful blending the share of IFS has to be larger than the one of the ICON model and that both shares should increase with time. Further, a smaller bias was found for the ANAKLIM++ blending than for the simple blending for each lead time. For the mean bias of the investigated cases the empirical variance is inadequate since the absolute values of the bias are much smaller which leads to larger results of the variance (Equation (5.8)).

5.5 Summary and Conclusions

Since weather and power forecasts always contain a part of uncertainty there will be balancing costs for TSOs related to forecast errors. However, these costs can be decreased by the reduction of the respective forecast errors (Lenzi et al., 2013). An example from the Dutch electricity market shows that sophisticated forecasts are able to improve the average profit from electricity which was generated by wind power plants. An advanced forecast model (24.7 EUR/MWh) is superior over persistence (22.4 EUR/MWh) by 10%

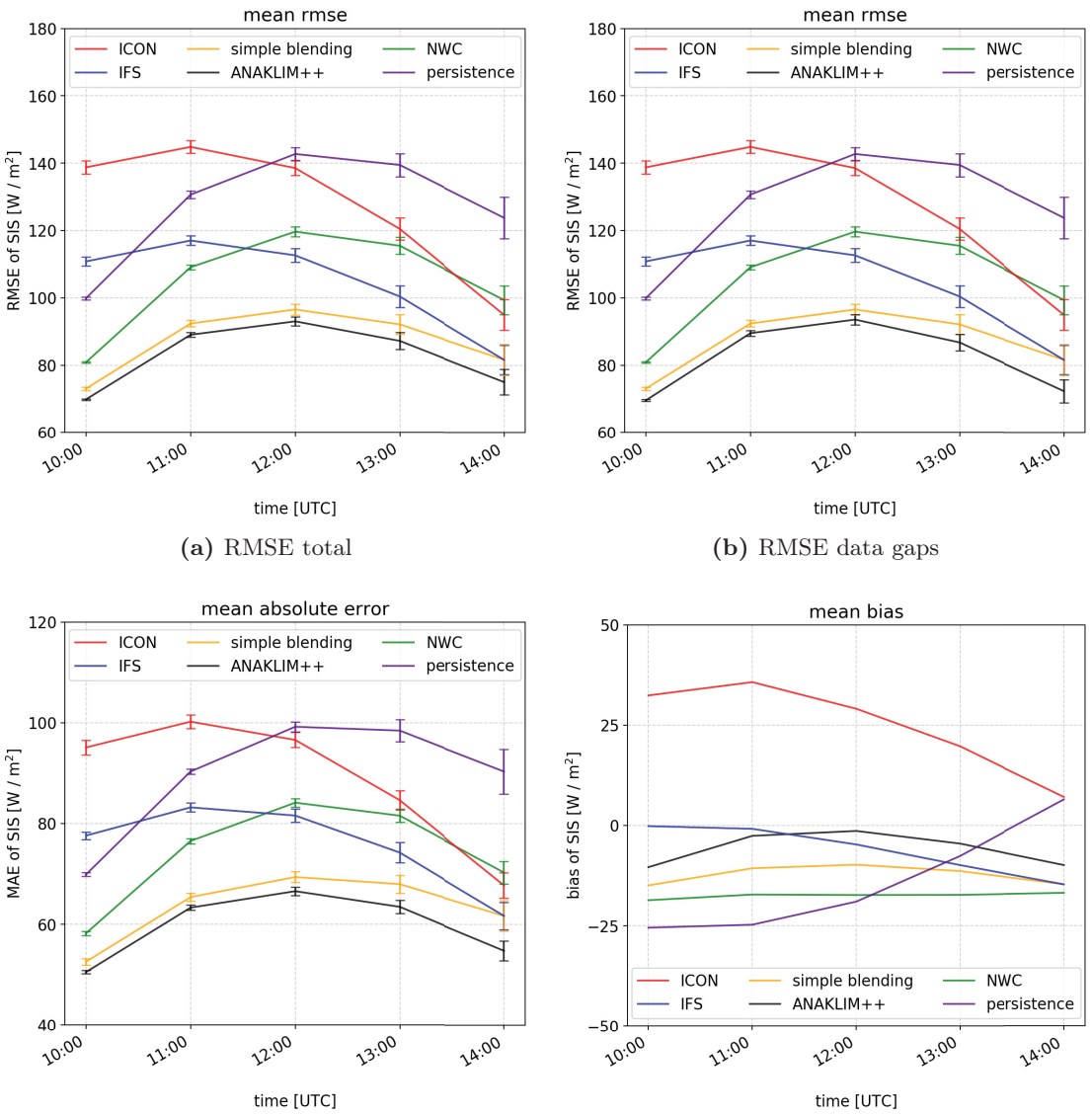

(a) RMSE total

(b) RMSE data gaps

(c) MAE data gaps

(d) bias data gaps

Figure 5.4: Mean error measures of all cases against day time for (a) RMSE with total NWC, (b) RMSE with gaps in NWC, (c) MAE with gaps in NWC and (d) bias with gaps in NWC. The empirical variance is depicted by error bars for (a)–(c). The validation of the solar surface irradiance for all forecasts was performed with SARAH-2 data and the region of interest is Europe.

and a perfect forecast (28.4 EUR/MWh) could lead to an increased income of 15% (Pinson, 2006).With regard to the rising share of renewable energies as a source of electricity the need for more accurate forecasts is growing rapidly.

In this study, a novel approach for a blending of a nowcasting and two NWP models, namely ICON from the DWD and IFS from the ECMWF, was presented. The aim of this combination is a seamless forecast of solar surface irradiance for a forecast horizon of 0–12 h. Further, this forecast should benefit from the higher temporal and spatial resolution from the nowcasting as well as from the reliable prediction of NWP on larger time scales. The blending of these forecast products is done between 1–5 h with a software tool called ANAKLIM++. Its original purpose was the efficient assimilation of two-dimensional data sets using a variational approach (Groß et al., 2014b). In this study ANAKLIM++ has been optimized and applied to a blending of NWP and nowcasting. The nowcasting of solar irradiance is based on the optical flow of the effective cloud albedo derived from the visible channel of MSG (Urbich et al., 2018, 2019). Furthermore, we applied a simple blending as a benchmark for ANAKLIM++. Both blendings and all input data were validated with SARAH-2 data from the CM SAF and further the bias, MAE and RMSE were calculated for each lead time respectively. In this study, 15 cases were examined from August, September and October 2017 due to their different weather situation and cloud patterns over central Europe (Table A.7). A special feature of ANAKLIM++ is that is was designed to fill data gaps for assimilation purposes. Thus, we took advantage of this feature and decided to cut out areas of potential error growth in the nowcasting to fill it with NWP data instead. The affected areas are still used for the blending but with a lower weight. That way, the areas of potential error growth are being penalized but they are still able to deliver additional information to the blending.

Due to the fact that regions with fast growing errors are cut out the overall look of the blended forecast shows large structures from the nowcasting while overestimated and underestimated values of SIS are corrected towards a medium state. Figure 5.4(d) depicts the bias of all forecast products for the time period of the blending. It becomes clear that a combined forecast of nowcasting, IFS and ICON has to result in medium state which in this case lies closer to the reference. As was already discussed in Urbich et al. (2019), SPECMAGIC NOW which is used for calculating solar surface irradiance produces a bias of about -25 W/m^2 for all lead times. This finding motivated the development of an improved version of SPECMAGIC NOW. ICON seems to overestimate solar surface irradiance which is a common fact for most NWP models while IFS only shows a small underestimation compared to SARAH-2 (Mathiesen et al., 2013; Huang et al., 2018). The quality of each forecast can be better assessed by regarding the MAE or RMSE which can be found in Figures 5.4(b) and 5.4(c). Both plots show a similar behavior of the results. ICON seems to be troubling a bit more with the prediction of SIS than IFS. Moreover, it is a proven fact that IFS from the ECMWF is a high quality forecast which usually performs better than other NWP models concerning solar surface irradiance (Perez et al., 2013, 2014; Remund et al., 2008). The ANAKLIM++ blending as well as the simple approach deliver better results than each individual forecast product for up to 4 h. Especially after 13 UTC the blending with ANAKLIM++ might have a small advantage over the simple approach. The RMSE and MAE of all forecasts decrease towards the evening because of the sunset. This effect can be canceled out by calculating relative error measures

instead of absolute ones as can be seen in Urbich et al. (2019). Relative error measures are of course important to evaluate the quality of forecasts however for the end users an absolute error is simply more useful. The users of the seamless solar irradiance forecast are transmission and distribution system operators as well as direct marketers, and they may use this forecast for trading and grid security. In this case, absolute errors are more useful since they are more direct. For this study the ANAKLIM++ blending has a RMSE of 72 W/m^2 and MAE of 55 W/m^2 after 4 h and the maximum is reached after 2 h, respectively. For a lead time of 2 h the RMSE equals 94 W/m^2 and the MAE is 67 W/m^2. After a forecast horizon of 4 h the ANAKLIM++ blending shows an improvement of 13% regarding the RMSE and 11% regarding the MAE in comparison to the simple blending. Haupt et al. (2016) report the maximum value of MAE for September and October after 7 h when the initialization lies between 09 and 12 UTC. In that case the MAE is approximately 70–75 W/m^2. All in all, the maximum MAE ranges between 60–125 W/m^2 for the whole validation period in 2015. Due to different regions of interest, error measures, validation periods or initialization times a comparison with other studies is complicated. Nevertheless, the results of this study show that ANAKLIM++ performs well as a blending tool in order to obtain a seamless prediction of solar surface irradiance. The errors are in the same order of magnitude as those of Haupt et al. (2016), Lorenz et al. (2012), Martínez Sánchez and Callado (2019) or Perez et al. (2014). Furthermore, the weight of the nowcasting can be defined regionally taking into account errors induced by different weather situations. This is a strong feature, but also a challenge for a seamless prediction since large regional differences in weights are a source for breaks and inhomogeneities. However, the spatial and temporal development of structures and patterns of SIS show no break. This in turn is an essential basis for a seamless prediction of solar irradiance. Further, the concept enables to take full benefit from improvements in the nowcasting method as well as NWP methods. This results in an enhancement of the quality of the seamless forecast up to 13% and 31% compared to IFS and ICON and 37% in contrast to the nowcasting after 4 h. Thus, ANAKLIM++ is well suited for the accurate and seamless forecast of solar surface irradiance from 0–12 h.

Acknowledgments

This research was funded by Gridcast, a project by the Federal Ministry for Economic Affairs and Energy (Bundesministerium für Wirtschaft und Energie, BMWi). We want to thank Jörg Trentmann and Uwe Pfeifroth for providing the SARAH-2 data for our validation. Thanks to Michael Mott, Manuel Werner and Nils Rathmann for the introduction and support regarding the POLARA framework which was used for the nowcasting of solar surface irradiance. POLARA was developed by the department of radar meteorology at the German Weather Service.

Chapter 6

Conclusion and Outlook

A fundamental transition of the power supply system is happening in Germany due to an increasing use of renewable energies as a source of electricity. The integration of fluctuating weather-dependent energy sources like wind and solar irradiance into the grid poses a big challenge for transition and distribution system operators. To maintain grid stability and to enable an efficient and sustainable use of solar energy a temporally and spatially high resolved, accurate forecast of solar surface irradiance for 0–12 h is essential. Neither a short-term forecast nor NWP can fulfill these requirements individually, thus a seamless forecast for solar irradiance has to be developed.

In the presented thesis a unique combination of three methods was presented which leads to an improved forecast quality and a seamless transition between nowcasting and NWP for solar surface irradiance. These methods were each introduced in one of the work packages. Their results will be summarized in the following section.

6.1 Conclusion

A first step of this thesis was the development of a nowcasting of the effective cloud albedo which can be derived from the visible channel of MSG. For this purpose, an algorithm called TV-L^1 by Zach et al. (2007) available from OpenCV was used to estimate the optical flow between two consecutive images of CAL. Within this thesis, TV-L^1 has been initially utilized and optimized for the effective cloud albedo. A big advantage of the TV-L^1 method is the free access and the comprehensive documentation of the method as well as its multi-scale approach. Within this context, the first research question can be answered:

- **Q1** By estimating the optical flow of the satellite derived effective cloud albedo the basis for the nowcasting of solar surface irradiance is formed.

Due to high spatial and temporal resolution of satellite measurements, the nowcasting of the effective cloud albedo and thus solar surface irradiance is available every 15 min with a horizontal resolution of 0.05°. A comparison between two popular methods for the estimation of the optical flow could show that TV-L^1 performs better than the method by Farnebäck (2003) for the use of CAL. An essential step of the implementation of the

optical flow algorithm was the optimization of its parameters with regard to the usage of CAL. The choice of these parameter values can affect the accuracy of the forecast as well as the optical structure of clouds. Thus, the optimization of these parameters represents the basis of the seamless prediction of SIS. Because of the usage of the effective cloud albedo all sorts of clouds will be forecasted including fog and low stratus. The optical flow is based on two major assumptions, (1) the pixel intensities of an object do not change between consecutive frames and (2) neighboring pixels have similar motion. The first assumption is responsible for the fact that the formation and dissipation of clouds cannot be resolved in an optical flow based nowcasting. This leads to errors for example due to convection. The second assumption leads to the characteristic behavior of the inward moving edge because optical flow methods usually do not use boundary conditions. This results in a no-data-area upstream of the pixel movement. However, since convection is a small-scale phenomenon the errors usually appear very locally and after 1 h of nowcasting the blending with ANAKLIM++ will cut out the regions of the highest errors compared with the analysis. The mean MAE and RMSE for the 135-min nowcasting of CAL from all examined cases equal 13% and 19%, respectively.

After the estimation of the optical flow of CAL, solar surface irradiance is computed for every forecast step by means of SPECMAGIC NOW to create a nowcasting of SIS. Within the scope of this thesis, SPECMAGIC NOW was used for the first time for a nowcasting. An extensive validation of this nowcasting was performed including two different kinds of reference data, namely pyranometer measurements from DWD and BSRN as well as satellite-derived data from CM SAF. Further, absolute and relative error measures were determined for both reference data sets for a forecast time up to 480 min. As expected, relative errors rise with increasing forecast time, independent of day time while absolute errors decrease towards the evening due to sun set. The behavior of relative and absolute error measures against the forecast time is very similar for SARAH-2 and the ground stations. A bias of about -25 W/m^2 was found in the validation of the nowcasting of SIS. Since this bias was detected after the combination of the nowcasting of CAL with SPECMAGIC NOW it appears that this bias results from the SPECMAGIC NOW algorithm. This negative bias represents an underestimation of solar surface irradiance which is a consequence of a miscalculation of the clear sky reflectance ρ_{cs}. Furthermore, an underestimation of ρ_{cs} leads to an overestimation of the optical depth of clouds. This finding motivated the development of an updated version of SPECMAGIC NOW. Furthermore, different methods of evaluation were done like a linear regression and a graphical mapping of the elements of the contingency table. For the contingency table, cloudy and clear sky pixels were separated by means of a threshold of CAL $= 0.025$. This separation of pixels revealed that errors can occur due to wrong advection or missing formation and dissipation of clouds. It was shown that the errors resulting from wrong advection are rather small while the neglect of intensity changes in the optical flow method is responsible for the largest deviations. In general, after 135 min of nowcasting of solar surface irradiance it was found a MAE of 93 W/m^2 and a RMSE of 136 W/m^2. The respective relative MAE of SIS amounts 19% and the relative RMSE equals 28%. The comparison with the relative errors of the CAL nowcasting reveals a slight increase of errors after the combination with SPECMAGIC NOW. This increase is most probably a consequence of the mentioned miscalculation of ρ_{cs} which has been

fixed in an updated version of SPECMAGIC NOW. At the end of WP 2 it is possible to answer the second research question:

- **Q2** In comparison to other forecast approaches like NWP or persistence the presented nowcasting leads to smaller errors for the first hours while it is available faster. Furthermore, forecast errors are in the same order as those of recently published nowcastings for solar surface irradiance (section 4.4).

In a final step of developing a seamless prediction system, a blending of the presented nowcasting and two NWP models, namely the IFS and the ICON, is performed. Before blending, these forecasts need to be evaluated concerning their error growth over time to determine the point of intersection between nowcasting and NWP. For this purpose, ICON, IFS and the nowcasting were validated with SARAH-2 data for different weather situations. One of the findings of this evaluation was the point of intersection between nowcasting and NWP which answers the third research question:

- **Q3** The point of intersection is approximately after 2.5 h for IFS and 4.5 h for ICON regarding the RMSE. The point of intersection between IFS and the nowcasting is slightly later with regard to the MAE. After this intersection the quality of NWP is higher compared to nowcasting with regard to SIS.

This finding can be affirmed by Arndt (2019) who stated the intercept after 2.75 ± 0.28 h for IFS and after 4.53 ± 0.97 h for ICON regarding the RMSE. However, these results are dependent on the time of initialization of the forecasts and of the day time. A second finding was the fact that IFS performs better than ICON for the whole investigated time horizon regarding solar surface irradiance.

WP 3 delivers the answer to the fourth research question:

- **Q4** The utilized software tool for the blending of nowcasting and NWP is called ANAKLIM++. It was originally designed for the efficient assimilation of two-dimensional data sets.

Hence, ANAKLIM++ is used for the first time for a combination of SIS forecasts within this thesis. Originally, ANAKLIM++ was developed to fill data gaps for assimilation purposes. Thus, it was an aim of this thesis to take advantage of this feature by cutting out areas of potential error growth in the nowcasting to fill these with NWP data instead. For every blending a new analysis of potentially problematic areas is done which supports a well fitted blending for every possible weather situation. As a result, large structures from the nowcasting will be transfered to the combined forecast while the amplitude of SIS values is adapted to a medium state. ANAKLIM++ works well in filling the data gaps of the nowcasting since no breaks or distinctive gradients are visible in the resulting forecast. This technique of cutting out regions of rapid error growth positively effects the quality of the forecast and additionally it makes the seamless prediction more reliable. Furthermore, a simple merging approach was developed to better assess the quality of

ANAKLIM++ as a blending tool. Both blending approaches are able to improve the forecast quality and deliver more accurate forecasts up to 4 h of lead time whereby ANAKLIM++ represents the superior blending approach. After a forecast horizon of 4 h the ANAKLIM++ blending shows an improvement of 13% regarding the RMSE and 11% regarding the MAE of SIS in comparison to the simple approach. Additionally, the improvement of the seamless forecast using ANAKLIM++ in contrast to the other forecasts amounts to 13% for IFS, 31% for ICON and 37% for nowcasting after 4 h. Due to the dependency of SIS on the position of the sun a decrease of absolute errors towards the evening can be recognized in all of the analyzed forecasts. For a lead time of 2 h the RMSE of the seamless prediction of SIS equals 94 W/m^2 and the MAE is 67 W/m^2 which is the maximum error of the analyzed forecast horizon.

Within the scope of this thesis multiple methods were used for the first time regarding their field of application. This concerns the optical flow method TV-L^1, the algorithm for the computation of solar surface irradiance SPECMAGIC NOW and ANAKLIM++. TV-L^1 was initially utilized and optimized for the effective cloud albedo and SPECMAGIC NOW was used for the first time as a part of a short-term forecast. Another novelty of the presented forecast system is the successful application of ANAKLIM++ for a seamless combination of nowcasting and NWP. The approach of applying ANAKLIM++ as a blending tool for forecasts is novel since the algorithm was originally designed for assimilation purposes of climate data.

The results show that ANAKLIM++ is well suited for the seamless prediction of solar surface irradiance. The spatial and temporal development of the cloud structures and patterns of solar surface irradiance transition seamlessly without any signs of a break. Moreover, ANAKLIM++ is capable of improving the forecast quality of NWP and nowcasting throughout the entire investigated forecast horizon by up to 37%. All in all, the forecast system for solar surface irradiance which was developed within this thesis is able to combine the advantages of nowcasting and NWP, respectively, resulting in a seamless and reliable forecast for 0–12 h.

6.2 Outlook

Usually the point of transition between a nowcasting and a NWP model lies between 2–3 h of forecast time. Therefore, in this thesis the blending is performed for 1–5 h and afterwards the nowcasting has no more impact on the forecast. Alternative opportunities would be to just use IFS after 5 h since it has the highest accuracy regarding solar irradiance prediction or to continue using ANAKLIM++ for a blending of several NWP models. If ANAKLIM++ will be utilized, the Lagrangian weights would probably need a re-adjustment and perhaps areas of fast error growths could be detected in the IFS in a similar manner as it was done for the nowcasting. Of course, all settings need to be evaluated in detail to obtain the optimal forecast for 5–12 h and further on.

The presented seamless forecast system was developed for solar surface irradiance with the aim of an application in the scope of energy meteorology. However, with small adjustments most of the already developed methods could be used in other fields of

meteorological forecasts. The solar irradiance product of the satellite department of the German Weather Service has been used for several years as a consulting product in the department of agricultural meteorology. Hence, a seamless prediction of SIS might also support the work in this field of research. Another possible adaption of the existing forecast system would be the calculation of the sunshine duration which could for example be used for touristic reasons. One of the perks of the herein developed forecast system is the element-wise composition of several methods. Thus, the nowcasting and the seamless prediction can not only be computed for solar surface irradiance but also for UV radiation which is an important forecast product in the scope of biometeorology and human health. For this calculation SPECMAGIC NOW could be utilized after small changes in its algorithm. Since UV radiation can be obtained as a result of NWP models an adaption of the presented blending methods would be possible.

With regard to future developments of numerical weather prediction, the point of transition and thus the procedure of a blending has to be reconsidered. With the accuracy of NWP models improving continuously, the point of interception will move towards smaller lead times. One possible outcome would be that a sophisticated blending like the one performed with ANAKLIM++ will be unnecessary and a simple blending approach would suffice. The aim of a blending is not only a seamless forecast without a break but also a higher forecast accuracy for each lead time noticeable in smaller errors. Even if the forecast quality of a simple approach is not as high as that of more sophisticated approaches nowadays like neural networks or ANAKLIM++, these differences might get smaller over time when NWP models improve their accuracy for shorter time horizons. Another consideration might be the development of even better nowcastings. By the means of hybrid nowcastings using radar, satellite and ground-based data combined different weather situations will be covered. Due to different measuring techniques, spatial and temporal resolutions and geometrical viewing angles a combination of various data sources might be the way to achieve more reliable short-term forecasts for longer time horizons. The launch of MTG which is expected for 2022 could lead to further improvement of a satellite-based nowcasting as well. With a higher spatial resolution a more accurate retrieval of the effective cloud albedo will be supported and the higher temporal resolution might improve the results of the optical flow estimation. With all these considerations the development of a seamless solar radiation forecast could look a lot different in a couple of years hence a blending between NWP and nowcasting would need to be re-evaluated.

Chapter 7

Zusammenfassung

In Deutschland vollzieht sich ein grundlegender Wandel des Stromversorgungssystems durch die zunehmende Nutzung erneuerbarer Energien als Stromquelle. Die Integration fluktuierender wetterabhängiger Energiequellen wie Wind und solare Einstrahlung in das Netz stellt die Übertragungs- und Verteilnetzbetreiber vor eine große Herausforderung. Zur Aufrechterhaltung der Netzstabilität und der effizienten und nachhaltigen Nutzung solarer Energie ist eine zeitlich und räumlich hoch aufgelöste Prognose der solaren Einstrahlung am Boden für 0–12 h unerlässlich. Weder eine Kurzfristprognose, noch die numerische Wettervorhersage kann diese Anforderungen allein erfüllen, sodass die Entwicklung einer nahtlosen Prognose der Sonneneinstrahlung unumgänglich ist.

Ein erster Schritt dieser Arbeit war die Entwicklung eines Nowcastings der effektiven Wolkenalbedo, die aus dem sichtbaren Kanal von MSG abgeleitet wurde. Zu diesem Zweck wurde ein Algorithmus namens TV-L^1 von Zach et al. (2007) verwendet, der in der OpenCV Bibliothek erhältlich ist. Im Rahmen dieser Arbeit wurde TV-L^1 erstmals für die effektive Wolkenalbedo verwendet und optimiert. Ein großer Vorteil des TV-L^1-Verfahrens, das in dieser Arbeit für die effektive Wolkenalbedo optimiert wurde, ist der freie Zugang und die umfassende Dokumentation des Verfahrens, sowie sein Multi-Skalen-Ansatz. In diesem Zusammenhang kann die erste Forschungsfrage beantwortet werden:

- **Q1** Durch die Schätzung des optischen Flusses der von Satelliten abgeleiteten effektiven Wolkenalbedo wird die Basis für das Nowcasting der solaren Einstrahlung gebildet.

Aufgrund der hohen räumlichen und zeitlichen Auflösung von Satellitenmessungen ist das Nowcasting der effektiven Wolkenalbedo und damit der solaren Einstrahlung alle 15 min mit einer horizontalen Auflösung von 0,05° verfügbar. Ein Vergleich zwischen zwei populären Methoden zur Abschätzung des optischen Flusses konnte zeigen, dass TV-L^1 unter der Verwendung von CAL präzisere Vorhersagen ermöglicht, als die Methode von Farnebäck (2003). Ein wesentlicher Schritt bei der Implementierung des Optical-Flow-Algorithmus war die Optimierung seiner Parameter im Hinblick auf die Verwendung von CAL. Die Wahl dieser Parameterwerte kann nicht nur die Genauigkeit der Vorhersage, sondern auch die optische Struktur der Wolken beeinflussen. Die Optimierung dieser Parameter stellt somit die Grundlage für die nahtlose Vorhersage von SIS dar. Durch

die Verwendung der effektiven Wolkenalbedo werden alle Arten von Wolken vorhergesagt einschließlich Nebel und tiefem Stratus. Der optische Fluss basiert auf zwei Hauptannahmen, (1) Pixelintensitäten eines Objekts zwischen aufeinanderfolgenden Bildern ändern sich nicht und (2) benachbarte Pixel weisen eine ähnliche Bewegung auf. Die erste Annahme ist für die Tatsache verantwortlich, dass die Bildung und Auflösung von Wolken bei einem auf dem optischen Fluss basierenden Nowcasting nicht aufgelöst werden kann. Dies führt zu Fehlern z.B. aufgrund von Konvektion. Die zweite Annahme führt zu dem charakteristischen Verhalten des einwärts laufenden Rands, da Optical-Flow-Methoden normalerweise keine Randbedingungen verwenden. Dies führt zu einem datenfreien Bereich stromaufwärts der Pixelbewegung. Da es sich bei Konvektion jedoch um ein kleinskaliges Phänomen handelt, treten die Fehler in der Regel sehr lokal auf, und nach 1 h Nowcasting schneidet das Blending mit ANAKLIM++ die Bereiche mit den höchsten Fehlern im Vergleich zur Analyse aus. Der mittlere MAE und RMSE für das 135-minütige Nowcasting von CAL aus allen untersuchten Fällen beträgt 13% bzw. 19%.

Nach der Abschätzung des optischen Flusses von CAL wird die solare Einstrahlung für jeden Prognoseschritt mit Hilfe von SPECMAGIC NOW berechnet, um ein Nowcasting von SIS zu erstellen. Im Rahmen dieser Arbeit wurde SPECMAGIC NOW zum ersten Mal für ein Nowcasting verwendet. Eine umfassende Validierung dieses Nowcastings wurde durchgeführt, wobei zwei verschiedene Arten von Referenzdaten einbezogen wurden, nämlich Pyranometermessungen vom DWD und BSRN sowie satellitengestützte Daten von CM SAF. Außerdem wurden absolute und relative Fehlermaße für beide Referenzdatensätze für eine Vorhersagezeit von bis zu 480 min bestimmt. Wie erwartet, nehmen die relativen Fehler mit zunehmender Vorhersagezeit unabhängig von der Tageszeit zu, während die absoluten Fehler gegen Abend aufgrund des Sonnenuntergangs abnehmen. Das Verhalten der relativen und absoluten Fehlermaße gegenüber der Vorhersagezeit ist für SARAH-2 und die Bodenstationen sehr ähnlich. Bei der Validierung des Nowcasting von SIS wurde eine Unterschätzung von etwa -25 W/m^2 gefunden. Da dieser Bias nach der Kombination des Nowcastings von CAL mit SPECMAGIC NOW festgestellt wurde, scheint dieser aus dem SPECMAGIC NOW-Algorithmus zu resultieren. Diese negative Abweichung stellt eine Unterschätzung der Globalstrahlung dar, die eine Folge einer Fehlberechnung der clear-sky-Reflexion ρ_{cs} ist. Darüber hinaus führt eine Unterschätzung von ρ_{cs} zu einer Überschätzung der optischen Dicke von Wolken. Diese Erkenntnis motivierte die Entwicklung einer überarbeiteten Version von SPECMAGIC NOW. Darüber hinaus wurden verschiedene Auswertungsmethoden, wie eine lineare Regression und eine grafische Abbildung der Elemente der Kontingenztabelle, durchgeführt. Für die Kontingenztabelle wurden wolkige und wolkenfreie Pixel durch einen Schwellenwert von CAL = 0.025 getrennt. Diese Trennung der Pixel ergab, dass Fehler durch falsche Advektion oder fehlende Bildung und Auflösung von Wolken auftreten können. Es zeigte sich, dass die Fehler aufgrund falscher Advektion relativ gering sind, während die Vernachlässigung von Intensitätsänderungen bei der Optical-Flow-Methode für die größten Abweichungen verantwortlich ist. Im Allgemeinen wurde nach 135 min Nowcasting der Globalstrahlung ein MAE von 93 W/m^2 und ein RMSE von 136 W/m^2 gefunden. Der jeweilige relative MAE von SIS beträgt 19% und der relative RMSE 28%. Der Vergleich mit den relativen Fehlern des CAL-Nowcastings zeigt einen leichten Anstieg der Fehler

nach der Kombination mit SPECMAGIC NOW. Dieser Anstieg ist höchstwahrscheinlich eine Folge der erwähnten Fehlberechnung von ρ_{cs}, die in einer überarbeiteten Version von SPECMAGIC NOW korrigiert wurde. Am Ende von WP 2 ist es möglich, die zweite Forschungsfrage zu beantworten:

- **Q2** Im Vergleich zu anderen Vorhersageansätzen wie NWV oder Persistenz führt das vorgestellte Nowcasting zu kleineren Fehlern für die ersten Stunden und ist gleichzeitig schneller verfügbar. Des Weiteren liegen die Prognosefehler in der gleichen Größenordnung wie bei den kürzlich veröffentlichten Nowcastings für die solare Einstrahlung (Abschnitt 4.4).

In einem letzten Schritt der Entwicklung eines nahtlosen Vorhersagesystems wird eine Kombination aus dem vorgestellten Nowcasting und zwei NWV-Modellen, nämlich dem IFS und dem ICON, durchgeführt. Vor der Kombination müssen diese Vorhersagen hinsichtlich ihres Fehlerwachstums im Laufe der Zeit bewertet werden, um den Schnittpunkt zwischen Nowcasting und NWV zu bestimmen. Zu diesem Zweck wurden ICON, IFS und Nowcasting mit SARAH-2-Daten für verschiedene Wettersituationen validiert. Eines der Ergebnisse dieser Auswertung war der Schnittpunkt zwischen Nowcasting und NWV, welches die dritte Forschungsfrage beantwortet:

- **Q3** Der Schnittpunkt ist ungefähr nach 2,5 h für IFS und 4,5 h für ICON bezüglich des RMSE. Der Schnittpunkt zwischen IFS und Nowcasting liegt etwas später in Bezug auf den MAE. Nach diesem Punkt ist die Qualität der NWV im Vergleich zum Nowcasting in Bezug auf die Globalstrahlung höher.

Dieser Befund kann von Arndt (2019) bestätigt werden, der bezüglich des RMSE den Schnittpunkt nach $2,75 \pm 0,28$ h für IFS und nach $4,53 \pm 0,97$ h für ICON angab. Diese Ergebnisse sind jedoch vom Zeitpunkt der Initialisierung der Vorhersagen und von der Tageszeit abhängig. Eine zweite Erkenntnis war die Tatsache, dass IFS für den gesamten untersuchten Zeithorizont hinsichtlich der solaren Einstrahlung besser abschneidet als ICON.

WP 3 liefert die Antwort auf die vierte Forschungsfrage:

- **Q4** Die verwendete Software für die Kombination von Nowcasting und NWV heißt ANAKLIM++. Sie wurde ursprünglich für die effiziente Assimilation von zweidimensionalen Datensätzen entwickelt.

ANAKLIM++ wird daher im Rahmen dieser Arbeit zum ersten Mal für eine Kombination von SIS-Prognosen eingesetzt. Ursprünglich wurde ANAKLIM++ entwickelt, um Datenlücken für Assimilierungszwecke zu füllen. Daher war es ein Ziel dieser Arbeit, dieses Feature zu nutzen, indem Bereiche mit potentiellem Fehlerwachstum im Nowcasting herausgeschnitten wurden, um diese stattdessen mit NWV-Daten zu füllen. Für jede Kombination wird eine neue Analyse der potentiell problematischen Bereiche durchgeführt, die eine gut angepasste Mischung für jede mögliche Wettersituation unterstützt.

Als Ergebnis werden große Strukturen aus dem Nowcasting in die kombinierte Prognose übertragen, während die Amplitude der SIS-Werte an einen mittleren Zustand angepasst wird. ANAKLIM++ ergänzt die Datenlücken des Nowcasting optimal, da in der resultierenden Prognose keine Brüche oder ausgeprägten Gradienten sichtbar sind. Diese Technik des Ausschneidens von Regionen mit raschem Fehlerwachstum wirkt sich positiv auf die Qualität der Prognose aus und macht darüber hinaus die nahtlose Vorhersage zuverlässiger. Außerdem wurde ein einfacher Merging-Ansatz entwickelt, um die Qualität von ANAKLIM++ als Blending-Tool besser beurteilen zu können. Beide Kombinationsansätze sind in der Lage, die Prognosegüte zu verbessern und genauere Prognosen mit einer Vorlaufzeit von bis zu 4 h zu liefern, wobei ANAKLIM++ den überlegenen Ansatz darstellt. Nach einem Prognosehorizont von 4 h zeigt der ANAKLIM++ Blending-Ansatz eine Verbesserung von 13% beim RMSE und 11% beim MAE der Globalstrahlung im Vergleich zum einfachen Ansatz. Zusätzlich beträgt die Verbesserung der nahtlosen Prognose mit ANAKLIM++ im Vergleich zu IFS 13%, zu ICON 31% und zum Nowcasting 37% nach 4 h. Aufgrund der Abhängigkeit von SIS vom Sonnenstand ist in allen analysierten Prognosen eine Abnahme der absoluten Fehler gegen Abend zu erkennen. Bei einer Laufzeit von 2 h beträgt der RMSE der nahtlosen Vorhersage von SIS 94 W/m^2 und der MAE 67 W/m^2, was dem maximalen Fehler des analysierten Vorhersagehorizonts entspricht.

Im Rahmen dieser Arbeit wurden mehrere Methoden erstmals hinsichtlich ihres Anwendungsbereichs eingesetzt. Dies betrifft die Optical-Flow-Methode TV-L^1, den Algorithmus zur Berechnung der Globalstrahlung SPECMAGIC NOW und ANAKLIM++. TV-L^1 wurde erstmals für die effektive Wolkenalbedo verwendet und optimiert und SPECMAGIC NOW wurde zum ersten Mal im Rahmen einer Kurzzeitprognose eingesetzt. Eine weitere Neuheit des vorgestellten Vorhersagesystems ist die erfolgreiche Anwendung von ANAKLIM++ für eine nahtlose Kombination von Nowcasting und NWV. Der Ansatz der Anwendung von ANAKLIM++ als Kombinationswerkzeug für Vorhersagen ist neuartig, da der Algorithmus ursprünglich für Assimilationszwecke von Klimadaten entwickelt wurde.

Die Ergebnisse zeigen, dass ANAKLIM++ gut für die nahtlose Vorhersage der solaren Einstrahlung geeignet ist. Die räumliche und zeitliche Entwicklung der Wolkenstrukturen und Muster der Globalstrahlung gehen nahtlos und ohne Anzeichen eines Bruchs ineinander über. Darüber hinaus ist ANAKLIM++ in der Lage, die Vorhersagequalität von NWV und Nowcasting über den gesamten untersuchten Vorhersagehorizont um bis zu 37% zu verbessern. Insgesamt ist das im Rahmen dieser Arbeit entwickelte Vorhersagesystem für die Globalstrahlung in der Lage, die Vorteile von Nowcasting und NWV zu kombinieren, sodass eine nahtlose und zuverlässige Vorhersage für 0–12 h entsteht.

Appendix A

Additional Tables

A.1 A Novel Approach for the Short-Term Forecast of the Effective Cloud Albedo

Day	Time	Weather Situation	Bias (%)	Abs. Bias (%)	RMSE (%)
7 August 2017	09:00	high pressure	-0.61	3.06	5.49
11 August 2017	14:00	stratiform precipitation	0.82	4.32	7.76
	15:00	stratiform precipitation	0.06	4.31	7.69
	16:00	stratiform precipitation	-0.21	4.80	8.21
15 August 2017	14:00	convection	0.51	3.66	6.86
	15:00	convection	0.07	3.63	6.78
28 August 2017	15:00	high pressure	0.04	4.77	8.23
29 August 2017	12:00	high pressure	0.08	3.90	7.03
1 September 2017	12:00	stratiform precipitation	0.10	3.52	6.40
7 September 2017	15:00	broken clouds	0.53	4.61	7.19
17 September 2017	12:00	broken clouds	0.24	4.71	8.24
19 September 2017	14:00	broken clouds	1.69	5.73	9.37
22 September 2017	09:00	broken clouds	0.36	3.92	6.65
26 September 2017	12:00	convection	0.44	4.67	7.68
	13:00	convection	0.31	4.80	7.82
30 September 2017	13:00	front & convection	0.10	4.08	6.67
1 October 2017	09:00	front	0.41	4.13	6.48
2 October 2017	12:00	stratiform precipitation	0.33	4.83	8.06
3 October 2017	13:00	broken clouds	0.21	5.28	8.35
4 October 2017	12:00	stratiform precipitation	0.44	4.22	9.57
7 October 2017	10:00	stratiform precipitation	-0.31	4.47	7.78

Table A.1: List of investigated cases for the settings of the parameters in the TV-L^1 method for the optical flow estimation of the effective cloud albedo. The error measures were calculated for a 15-min-forecast over the area of Europe.

Forecast Time (Min)	Bias (%)	Absolute Bias (%)	RMSE (%)
30	0.41	6.35	10.47
60	0.41	9.10	14.28
90	0.57	11.12	16.87
120	0.43	12.78	18.83

Table A.2: Mean values of the bias, absolute bias and RMSE for all investigated cases. The basis for the calculation is the area of Europe.

A.2 The SESORA Forecast for Solar Surface Irradiance– Method and Validation

Event	Label	Location	Latitude (°)	Longitude (°)	Elevation (m)
Cabauw	CAB	Netherlands	51.9711	4.9267	0.0
Carpentras	CAR	France	44.0830	5.0590	100.0
Cener	CNR	Spain	42.8160	−1.6010	471.0
Palaiseau	PAL	France	48.7130	2.2080	156.0

Table A.3: List of BSRN pyranometer stations in the region of Europe. The stations that did not measure the radiation or deliver the data for the period of our study were not listed.

Location	DWD-ID	Latitude (°)	Longitude (°)	Elevation (m)
Arkona	183	54.6791	13.4342	42.0
Braunlage	656	51.7233	10.6021	607.3
Braunschweig	662	52.2914	10.4464	81.4
Bremen	691	53.0445	8.7985	4.3
Chemnitz	853	50.7912	12.8719	418.0
Dresden	1048	51.1279	13.7543	227.0
Fichtelberg	1358	50.4283	12.9535	1213.0
Geisenheim	1580	49.9859	7.9548	110.2
Görlitz	1684	51.1621	14.9505	238.0
Hamburg	1975	53.6331	9.9880	14.1
Hohenpeissenberg	2290	47.8009	11.0108	977.0
Konstanz	2712	47.6774	9.1900	442.5
Leipzig	2928	51.3150	12.4462	138.0
Lindenberg	3015	52.2084	14.1179	98.0
Bad-Lippspringe	3028	51.7854	8.8387	157.0
Lüdenscheid	3098	51.2451	7.6424	386.7
Meiningen	3231	50.5611	10.3771	450.0
Norderney	3631	53.7123	7.1519	11.5
Nuremberg	3668	49.5030	11.0549	314.0
Potsdam	3987	52.3812	13.0622	81.0
Rostock	4271	54.1801	12.0805	4.0
Saarbrücken	4336	49.2128	7.1077	320.0
Sankt-Peter-Ording	4393	54.3279	8.6029	4.9
Schleswig	4466	54.5275	9.5486	42.7
Seehausen	4642	52.8911	11.7296	21.0
Stuttgart	4928	48.8281	9.2000	314.3
Trier	5100	49.7478	6.6582	265.0
Weihenstephan	5404	48.4024	11.6945	477.1
Weissenburg	5440	49.0113	10.9319	439.3
Würzburg	5705	49.7702	9.9577	268.0
Zugspitze	5792	47.4208	10.9847	2964.0
Fürstenzell	5856	48.5451	13.3530	476.4
Mannheim	5906	49.5090	8.5540	98.0
Schneefernerhaus	7325	47.4167	10.9794	2650.0

Table A.4: List of DWD pyranometer stations.

Date	Forecast Time (Min)							
	45	**105**	**165**	**225**	**285**	**345**	**405**	**465**
7 August 2017	9.10	11.52	13.62	15.28	17.08	17.77	19.67	23.43
	58.64	79.25	93.11	97.01	93.38	79.13	61.58	40.78
11 August 2017	11.52	14.32	16.26	17.70	19.36	20.76	23.32	27.17
	66.73	89.09	101.11	102.40	95.17	82.92	64.72	59.63
15 August 2017	8.98	11.93	13.59	15.73	17.60	18.04	19.86	23.04
	58.41	82.36	92.62	98.72	94.24	77.21	58.65	54.92
28 August 2017	11.70	16.25	19.48	21.93	24.44	26.46	28.83	32.95
	66.24	96.75	113.62	117.03	108.83	91.3	92.82	51.57
29 August 2017	10.59	13.58	16.20	17.64	19.67	21.69	24.21	30.17
	60.23	81.35	95.03	94.51	87.79	73.67	51.14	47.41
1 September 2017	10.47	14.91	17.00	18.51	20.21	20.84	22.39	23.86
	59.55	90.18	101.61	101.11	92.97	75.20	52.62	31.11
7 September 2017	14.60	20.20	23.52	24.48	26.33	27.21	28.16	25.55
	65.20	94.47	107.60	102.78	91.44	73.71	46.93	22.76
17 September 2017	12.59	18.04	21.43	22.63	23.31	23.77	25.32	26.72
	59.18	88.51	102.30	98.81	83.44	63.65	38.11	22.92
19 September 2017	14.26	19.87	23.15	24.63	26.12	26.36	26.77	23.74
	64.52	94.35	106.79	103.11	88.90	66.95	38.74	20.08
22 September 2017	11.67	15.23	-	19.47	21.14	23.48	24.47	26.24
	52.09	71.82	-	80.67	70.85	57.53	33.92	20.08
26 September 2017	15.13	19.79	22.65	24.32	26.26	27.90	27.83	25.71
	64.69	89.15	98.55	96.67	83.70	63.01	35.77	17.62
30 September 2017	12.79	17.30	20.62	22.14	25.03	26.79	31.07	31.91
	53.20	74.10	82.72	78.56	67.87	47.80	29.88	15.29
1 October 2017	16.76	21.20	23.70	25.71	28.12	32.62	38.52	37.42
	65.97	87.08	91.81	87.65	73.45	57.72	37.50	18.60
2 October 2017	18.10	23.08	26.33	28.05	30.56	32.27	35.01	35.59
	73.02	97.73	105.55	99.08	81.54	59.67	38.27	19.53
3 October 2017	16.49	20.51	22.96	24.58	26.91	28.97	30.11	31.52
	67.94	89.16	95.75	92.08	78.98	57.96	35.44	17.39
4 October 2017	16.46	19.63	21.55	22.70	23.71	25.37	25.80	25.83
	66.59	84.74	87.86	82.82	67.34	48.45	29.22	13.76
7 October 2017	17.26	20.26	21.60	22.52	23.32	24.32	23.22	22.59
	63.81	79.09	80.57	77.10	62.80	44.35	26.26	11.87

Table A.5: Error measures of SARAH-2 validation for all cases up to 465 min of forecast time. These values were calculated for the area of Europe. The upper row of each date represents the relative absolute bias in % and the lower one shows the absolute bias in W/m^2 respectively.

Date	Forecast Time (Min)							
	45	**105**	**165**	**225**	**285**	**345**	**405**	**465**
7 August 2017	8.59	15.07	20.71	23.51	26.39	27.54	30.82	37.92
	83.88	117.61	140.33	147.39	142.00	120.23	94.27	64.14
11 August 2017	17.66	22.45	25.29	27.17	29.80	31.91	35.54	41.20
	101.97	138.38	154.88	153.84	142.45	123.20	94.82	59.63
15 August 2017	16.62	20.29	22.98	24.67	27.92	28.90	31.51	36.30
	89.69	128.84	143.23	151.98	145.85	120.17	89.71	54.92
28 August 2017	17.19	24.15	28.91	32.73	24.44	39.61	44.28	52.94
	96.96	142.22	165.55	170.24	157.76	131.24	92.82	51.57
29 August 2017	16.17	20.99	25.42	28.22	31.73	35.53	42.24	53.14
	91.63	124.27	146.14	146.92	136.38	115.26	82.46	47.41
1 September 2017	16.09	23.25	26.42	28.82	31.33	31.70	33.50	35.64
	91.46	140.16	156.92	156.03	142.43	112.87	77.40	41.14
7 September 2017	21.42	29.39	33.93	35.58	38.06	38.21	39.12	36.04
	95.26	135.83	152.04	144.92	127.03	98.48	61.37	25.36
17 September 2017	20.03	28.11	32.94	34.00	34.68	34.54	37.74	38.04
	94.01	137.29	156.01	146.83	122.36	90.85	55.61	23.88
19 September 2017	21.35	29.26	33.55	35.35	37.79	37.46	38.94	32.85
	96.31	137.75	152.47	144.86	123.69	91.85	53.48	19.26
22 September 2017	17.59	23.31	-	29.91	32.47	35.32	38.31	37.71
	78.26	108.74	-	120.81	105.42	83.23	49.92	19.45
26 September 2017	21.47	28.35	32.46	34.35	36.85	38.65	39.78	35.48
	91.53	126.61	139.11	133.64	114.23	84.33	46.76	15.44
30 September 2017	18.72	25.98	30.79	32.50	36.57	40.17	47.02	43.47
	77.60	110.16	121.39	112.39	95.85	68.69	38.54	11.15
1 October 2017	22.15	29.35	33.22	35.94	39.22	45.75	57.08	58.69
	86.68	118.58	125.20	117.78	97.28	75.99	46.10	14.51
2 October 2017	24.11	31.23	35.61	37.91	41.33	44.22	48.51	45.29
	96.87	130.68	139.94	130.20	106.39	78.32	43.98	12.90
3 October 2017	22.61	28.89	32.40	34.27	37.21	40.00	42.31	43.30
	92.80	123.99	132.34	124.65	105.10	76.32	40.53	12.11
4 October 2017	22.87	28.26	30.59	31.55	32.55	34.27	35.76	35.71
	92.29	119.76	122.95	112.75	89.92	63.21	33.25	9.84
7 October 2017	25.41	30.05	31.78	32.05	32.13	32.39	31.94	28.01
	92.53	115.66	115.80	106.17	82.92	56.12	28.07	6.67

Table A.6: Error measures of SARAH-2 validation for all cases up to 465 min of forecast time. These values were calculated for the area of Europe. The upper row for each date represents the relative RMSE in % and the lower one shows the RMSE in W/m^2 respectively.

A.3 Development of a seamless forecast for solar surface irradiance using ANAKLIM++

Date	Weather Situation / Cloud Type	Day Time (UTC)				
		10	11	12	13	14
7 August 2017	high pressure	48.30	61.64	67.92	70.94	67.22
	cirrus	68.14	91.35	101.81	101.65	91.38
11 August 2017	stratiform precipitation	49.12	60.80	63.21	62.88	59.19
	stratus	72.66	91.68	94.60	90.85	81.76
15 August 2017	convection	47.19	61.08	68.48	73.96	69.32
	cumulus nimbus	70.99	94.97	104.18	107.58	96.68
28 August 2017	high pressure	51.01	67.50	73.41	71.34	65.25
	cirrus	70.78	96.63	106.4	101.67	89.50
29 August 2017	high pressure	48.05	61.97	66.57	67.04	61.18
	cirrus	70.22	92.45	99.91	98.03	86.24
1 September 2017	stratiform precipitation	50.61	67.90	73.91	73.13	64.57
	stratus	73.75	100.72	106.94	102.02	86.28
7 September 2017	broken clouds	52.58	70.20	75.34	70.30	59.89
	cumulus	72.75	95.96	100.94	92.28	75.54
17 September 2017	broken clouds	48.19	67.19	72.16	66.35	53.82
	cumulus	71.23	99.70	104.32	91.82	70.97
26 September 2017	convection	51.18	66.56	71.07	65.65	52.12
	cumulus nimbus	68.50	90.47	95.84	86.40	66.54
30 September 2017	front & convection	41.83	54.12	56.35	51.44	41.38
	stratus & cumulus	59.28	77.83	79.33	69.97	54.94
1 October 2017	front & convection	56.31	66.78	67.82	62.36	53.00
	stratus & cumulus	70.67	85.74	86.00	76.57	62.67
2 October 2017	stratiform precipitation	60.52	73.19	74.20	67.50	54.72
	stratus	76.69	95.71	97.24	87.35	69.68
3 October 2017	broken clouds	53.53	60.70	60.93	55.04	45.34
	cumulus	68.14	79.91	79.89	69.93	55.97
4 October 2017	stratiform precipitation	51.49	58.76	58.12	52.19	41.70
	stratus	65.95	77.37	76.85	68.89	55.14
7 October 2017	stratiform precipitation	47.81	51.14	49.07	41.82	33.14
	stratus	63.50	72.03	68.84	56.10	41.51

Table A.7: List of investigated cases with corresponding main weather situation and cloud type over Germany. The upper row shows the MAE and the lower row shows the RMSE, respectively. The unit for the error measures is W/m^2.

Bibliography

AGEB (2020): Homepage of the ag energiebilanz e.v. `https://www.ag-energiebilanzen.de/`. Accessed: 2020-08-28.

Aguiar, L.M., Pereira, B., Lauret, P., Díaz, F., and David, M. (2016): Combining solar irradiance measurements, satellite-derived data and a numerical weather prediction model to improve intra-day solar forecasting. *Renewable Energy*, 97, 599–610.

Akarslan, E., Hocaoğlu, F.O., and Edizkan, R. (2014): A novel md (multi-dimensional) linear prediction filter approach for hourly solar radiation forecasting. *Energy*, 73, 978–986.

Aksakal, S. (2013): Geometric accuracy investigations of seviri high resolution visible (hrv) level 1.5 imagery. *Remote Sensing*, 5, 2475–2491.

Albadi, M. and El-Saadany, E. (2009): Wind turbines capacity factor modeling—a novel approach. *IEEE Transactions on Power Systems*, 24(3), 1637–1638.

Aliberti, A., Bottaccioli, L., Cirrincione, G., Macii, E., Acquaviva, A., and Patti, E. (2018): Forecasting short-term solar radiation for photovoltaic energy predictions. In *SMARTGREENS*, Seiten 44–53.

Amillo, A., Huld, T., and Müller, R. (2014): A new database of global and direct solar radiation using the eastern meteosat satellite, models and validation. *Remote Sensing*, 6, 8165–8189.

Antonanzas, J., Osorio, N., Escobar, R., Urraca, R., Martinez-de Pison, F., and Antonanzas-Torres, F. (2016): Review of photovoltaic power forecasting. *Solar Energy*, 136(78-111).

Arbizu-Barrena, C., Ruiz-Arias, J.A., Rodríguez-Benítez, F.J., Pozo-Vázquez, D., and Tovar-Pescador, J. (2017): Short-term solar radiation forecasting by advecting and diffusing msg cloud index. *Solar Energy*, 155, 1092–1103.

Arndt, E. (2019): *Vergleich von Kurzfrist-Strahlungsvorhersagen (Nowcasting) mit Vorhersagen aus numerischen Wettermodellen im Kontext der nahtlosen Strahlungsvorhersage*. Masterarbeit, Johann Wolfgang Goethe-University Frankfurt am Main.

Bacher, P., Madsen, H., and Nielsen, H.A. (2009): Online short-term solar power forecasting. *Solar energy*, 83(10), 1772–1783.

Baker, S., Scharstein, D., Lewis, J., Roth, S., Black, M.J., and Szeliski, R. (2011): A database and evaluation methodology for optical flow. *International Journal of Computer Vision*, 92(1), 1–31.

Baldauf, M., Gebhardt, C., Theis, S., Ritter, B., and Schraf, C. (2018): Beschreibung des operationellen kürzestfristvorhersagemodells cosmo-d2 und cosmo-d2-eps und seiner ausgabe in die datenbanken des dwd.(2018).

Barbieri, F., Rajakaruna, S., and Gosh, A. (2017): Very short-term photovoltaic power forecasting with cloud modeling: A review. *Renewable and Sustainable Energy Reviews*, 75, 242–263.

Barron, J.L., Fleet, D.J., and Beauchemin, S.S. (1994): Performance of optical flow techniques. *International journal of computer vision*, 12(1), 43–77.

Beauchemin, S.S. and Barron, J.L. (1995): The computation of optical flow. *ACM computing surveys (CSUR)*, 27(3), 433–466.

Bellouin, N., Quaas, J., Morcrette, J.J., and Boucher, O. (2013): Estimates of aerosol radiative forcing from the macc re-analysis. *Atmospheric Chemistry and Physics*, 13(4), 2045–2062.

Berenguer, M., Sempere-Torres, D., and Pegram, G.G. (2011): Sbmcast–an ensemble nowcasting technique to assess the uncertainty in rainfall forecasts by lagrangian extrapolation. *Journal of Hydrology*, 404(3-4), 226–240.

Beyer, H., Costanzo, C., and Heinemann, D. (1996): Modifications of the heliosat procedure for irradiance estimates from satellite images. *Solar Energy*, 56, 207–212.

Boata, R.S. and Gravila, P. (2012): Functional fuzzy approach for forecasting daily global solar irradiation. *Atmospheric Research*, 112, 79–88.

Bosch, J., Lopez, G., and Batlles, F. (2008): Daily solar irradiation estimation over a mountainous area using artificial neural networks. *Renewable Energy*, 33(7), 1622–1628.

Bosch, J.L., Zheng, Y., and Kleissl, J. (2013): Deriving cloud velocity from an array of solar radiation measurements. *Solar Energy*, 87, 196–203.

Bowler, N.E., Pierce, C.E., and Seed, A.W. (2006): Steps: A probabilistic precipitation forecasting scheme which merges an extrapolation nowcast with downscaled nwp. *Quarterly Journal of the Royal Meteorological Society: A journal of the atmospheric sciences, applied meteorology and physical oceanography*, 132(620), 2127–2155.

Brown, J.F., Loveland, T.R., Merchant, J.W., Reed, B.C., and Ohlen, D.O. (1993): Using multisource data in global land-cover characterization: Concepts, requirements, and methods. *Photogrammetric Engineering and Remote Sensing*, 59(6), 977–987.

BSRN (2020): Homepage of the baseline surface radiation network. `https://bsrn.awi.de/`. Accessed: 2020-07-23.

Bundesnetzagentur (2020): Homepage of the federal grid agency. `https://www.bundesnetzagentur.de/`. Accessed: 2020-07-30.

Burton, A. and Radford, J. (1978): *Thinking in Perspective: Critical Essays in the Study of Thought Processes.* Psychology in progress. Methuen.

Cano, D., Monget, J., Albuisson, M., Guillard, H., Regas, N., and Wald, L. (1986): A method for the determination of the global solar radiation from meteorological satellite data. *Solar Energy*, 37, 31–39.

Chambolle, A. (2004): An algorithm for total variation minimization and applications. *Journal of Mathematical Imaging and Vision*, 20(1), 89–97.

Cheng, H.Y. (2017): Cloud tracking using clusters of feature points for accurate solar irradiance nowcasting. *Renewable Energy*, 104, 281 – 289.

Cros, S., Liandrat, O., Sébastien, N., and Schmutz, N. (2014): Extracting cloud motion vectors from satellite images for solar power forecasting. In *2014 IEEE Geoscience and Remote Sensing Symposium*, Seiten 4123–4126. IEEE.

Dambreville, R., Blanc, P., Chanussot, J., and Boldo, D. (2014): Very short term forecasting of the global horizontal irradiance using a spatio-temporal autoregressive model. *Renewable Energy*, 72, 291–300.

Dürrschmidt, D.W. and van Mark, D.M. (2007): Hintergrundinformationen zum eeg-erfahrungsbericht 2007. *Bundesministerium für Umwelt, Naturschutz und Reaktorsicherheit (BMU).* `http://erneuerbare-energien.de/files/pdfs/allgemein/application/pdf/eeg_kosten_nutzen_hintergrund.pdf`.

ECMWF (2019): IFS Documentation. `https://www.ecmwf.int/en/publications/ifs-documentation`.

ECMWF (2019): Homepage of the European Centre for Medium-Range Weather Forecasts. `https://www.ecmwf.int/`. Accessed: 2019-10-18.

EIA (2019): Homepage of the U.S. Energy Information Administration. International Energy Outlook 2019. `https://www.eia.gov/outlooks/ieo/`. Accessed: 2020-07-22.

Energy Transition (2019): The Global Energiewende. Homepage of the German Energy Transition. `https://energytransition.org/legal/`. Accessed: 2020-06-29.

Escrig, H., Batlles, F., Alonso, J., Baena, F., Bosch, J., Salbidegoitia, I., and Burgaleta, J. (2013): Cloud detection, classification and motion estimation using geostationary satellite imagery for cloud cover forecast. *Energy*, 55, 853–859.

Farnebäck, G. (2003): Two-frame motion estimation based on polynomial expansion. *Image analysis*, Seiten 363–370.

Fraunhofer ISE (2020): Homepage of the fraunhofer institute for solar energy systems. `https://www.ise.fraunhofer.de/`. Accessed: 2020-08-24.

Gallucci, D., Romano, F., Cersosimo, A., Cimini, D., Di Paola, F., Gentile, S., Geraldi, E., Larosa, S., Nilo, S.T., Ricciardelli, E., and Viggiano, M. (2018): Nowcasting surface solar irradiance with amesis via motion vector fields of msg-seviri data. *Remote Sensing*, 10(6).

Germann, U. and Zawadzki, I. (2002): Scale-dependence of the predictability of precipitation from continental radar images. part i: Description of the methodology. *Monthly Weather Review*, 130(12), 2859–2873.

Ghanbarzadeh, A., Noghrehabadi, A., Assareh, E., and Behrang, M. (2009): Solar radiation forecasting based on meteorological data using artificial neural networks. In *2009 7th IEEE International Conference on Industrial Informatics*, Seiten 227–231. IEEE.

Gridcast (2020): Homepage of gridcast. `http://gridcast.iee.fraunhofer.de/`. Accessed: 2020-07-30.

Groß, A., Fränkel, S., Seelge, M., and Schömer, E. (2014a): ANAKLIM-plus plus Projektdokumentation.

Groß, A., Müller, R., Schömer, E., and Trentmann, J. (2014b): Terrestrial cross-calibrated assimilation of various datasources. In *EGU General Assembly Conference Abstracts*, Volume 16.

Guillot, E.M., Vonder Haar, T.H., Forsythe, J.M., and Fletcher, S.J. (2012): Evaluating satellite-based cloud persistence and displacement nowcasting techniques over complex terrain. *Weather and Forecasting*, 27(2), 502–514.

Hamill, T.M. and Nehrkorn, T. (1993): A short-term cloud forecast scheme using cross correlations. *Weather and Forecasting*, 8(4), 401–411.

Hammer, A., Heinemann, D., Hoyer, C., Kuhlemann, R., Lorenz, E., Müller, R., and Beyer, H. (2003): Solar energy assessment using remote sensing technologies. *Remote Sens. Environ.*, 86(3), 423–432.

Harty, T.M., Holmgren, W.F., Lorenzo, A.T., and Morzfeld, M. (2019): Intra-hour cloud index forecasting with data assimilation. *Solar Energy*, 185, 270–282.

Haupt, S.E., Kosović, B., Jensen, T., Lazo, J.K., Lee, J.A., Jiménez, P.A., Cowie, J., Wiener, G., McCandless, T.C., Rogers, M., et al. (2018): Building the sun4cast system: Improvements in solar power forecasting. *Bulletin of the American Meteorological Society*, 99(1), 121–136.

Haupt, S.E., Kosovic, B., Jensen, T., Lee, J., Jimenez, P., Lazo, J., Cowie, J., McCandless, T., Pearson, J., Weiner, G., et al. (2016): The suncast solar-power forecasting system: the results of the public-private-academic partnership to advance solar power forecasting. *National Center for Atmospheric Research (NCAR), Boulder (CO): Research Applications Laboratory, Weather Systems and Assessment Program (US).*

Hocaoğlu, F.O. (2011): Stochastic approach for daily solar radiation modeling. *Solar Energy*, 85(2), 278–287.

Horn, B.K. and Schunck, B.G. (1981): Determining optical flow. *Artificial intelligence*, 17(1-3), 185–203.

Huang, J., Rikus, L.J., Qin, Y., and Katzfey, J. (2018): Assessing model performance of daily solar irradiance forecasts over australia. *Solar Energy*, 176, 615–626.

Huang, J. and Thatcher, M. (2017): Assessing the value of simulated regional weather variability in solar forecasting using numerical weather prediction. *Solar Energy*, 144, 529–539.

Huertas-Tato, J., Aler, R., Galván, I.M., Rodríguez-Benítez, F.J., Arbizu-Barrena, C., and Pozo-Vázquez, D. (2020): A short-term solar radiation forecasting system for the iberian peninsula. part 2: Model blending approaches based on machine learning. *Solar Energy*, 195, 685–696.

IAEA (2020): Homepage of the international atomic energy agency. `https://www.iaea.org/`. Accessed: 2020-07-29.

Inman, R.H., Pedro, H.T., and Coimbra, C.F. (2013): Solar forecasting methods for renewable energy integration. *Progress in Energy and Combustion Science*, 39(6), 535 – 576.

Islam, M.A., Merabet, A., Beguenane, R., and Ibrahim, H. (2013): Modeling solar photovoltaic cell and simulated performance analysis of a 250w pv module. In *2013 IEEE Electrical Power & Energy Conference*, Seiten 1–6. IEEE.

Kilambi, A. and Zawadzki, I. (2005): An evaluation of ensembles based upon maple precipitation nowcasts and nwp precipitation forecasts. In *Preprints, 32nd Conf. on Radar Meteorology, Albuquerque, NM, Amer. Meteor. Soc., P3R*, Volume 4.

Kühnert, J. (2016): *Development of a photovoltaic power prediction system for forecast horizons of several hours*. Dissertation, Universität Oldenburg.

Kurz, C. (2018): From nowcasting to day ahead forecasting: Application of combinational pv power forecasts. icem. `http://www.wemcouncil.org/wp/wp-content/uploads/2016/12/icem_20180524_room1_0950_kurz.pdf`. Accessed: 2020-07-22.

Kusiak, A. and Verma, A. (2012): Monitoring wind farms with performance curves. *IEEE Transactions on Sustainable Energy*, 4(1), 192–199.

Lalouni, S., Rekioua, D., Rekioua, T., and Matagne, E. (2009): Fuzzy logic control of stand-alone photovoltaic system with battery storage. *Journal of power Sources*, 193(2), 899–907.

Lenzi, V., Ulbig, A., and Andersson, G. (2013): Impacts of forecast accuracy on grid integration of renewable energy sources. In *2013 IEEE Grenoble Conference*, Seiten 1–6. IEEE.

Lin, C., Vasić, S., Kilambi, A., Turner, B., and Zawadzki, I. (2005): Precipitation forecast skill of numerical weather prediction models and radar nowcasts. *Geophysical research letters*, 32(14).

Lorenz, E., Hammer, A., Heinemann, D., et al. (2004): Short term forecasting of solar radiation based on satellite data. In *EUROSUN2004 (ISES Europe Solar Congress)*, Seiten 841–848.

Lorenz, E., Kühnert, J., and Heinemann, D. (2012): Short term forecasting of solar irradiance by combining satellite data and numerical weather predictions. In *Proceedings of the 27th European PV Solar Energy Conference (EU PVSEC), Frankfurt, Germany*, Volume 2428, Seite 44014405.

Loveland, T.R. and Belward, A.S. (1997): The igbp-dis global 1km land cover data set, discover: First results. *International Journal of Remote Sensing*, 18(15), 3289–3295.

Marquez, R. and Coimbra, C.F. (2011): Forecasting of global and direct solar irradiance using stochastic learning methods, ground experiments and the nws database. *Solar Energy*, 85(5), 746–756.

Marquez, R., Pedro, H.T., and Coimbra, C.F. (2013): Hybrid solar forecasting method uses satellite imaging and ground telemetry as inputs to anns. *Solar Energy*, 92, 176–188.

Martínez Sánchez, M. and Callado, A. (2019): nowcradiation seamless-nowcasting solar radiation using satellite and high resolution numerical model output.

Mathiesen, P., Collier, C., and Kleissl, J. (2013): A high-resolution, cloud-assimilating numerical weather prediction model for solar irradiance forecasting. *Solar Energy*, 92, 47–61.

Mathiesen, P. and Kleissl, J. (2011): Evaluation of numerical weather prediction for intra-day solar forecasting in the continental united states. *Solar Energy*, 85(5), 967–977.

Matsuoka, A., Babin, M., and Devred, E.C. (2016): A new algorithm for discriminating water sources from space: A case study for the southern beaufort sea using modis ocean color and smos salinity data. *Remote Sensing of Environment*, 184, 124–138.

Mellit, A. and Pavan, A.M. (2010): A 24-h forecast of solar irradiance using artificial neural network: Application for performance prediction of a grid-connected pv plant at trieste, italy. *Solar Energy*, 84(5), 807–821.

Moghaddamnia, A., Remesan, R., Kashani, M.H., Mohammadi, M., Han, D., and Piri, J. (2009): Comparison of llr, mlp, elman, nnarx and anfis models—with a case study in solar radiation estimation. *Journal of Atmospheric and Solar-Terrestrial Physics*, 71(8-9), 975–982.

Mohandes, M., Rehman, S., and Halawani, T. (1998): Estimation of global solar radiation using artificial neural networks. *Renewable energy*, 14(1-4), 179–184.

Mora-Lopez, L. and Sidrach-de Cardona, M. (1998): Multiplicative arma models to generate hourly series of global irradiation. *Solar Energy*, 63(5), 283–291.

Mueller, R., Pfeifroth, U., and Traeger-Chatterjee, C. (2015): Towards optimal aerosol information for the retrieval of solar surface radiation using heliosat. *Atmosphere*, 6(7), 863–878.

Müller, R., Pfeifroth, U., Träger-Chatterjee, C., Trentmann, J., and Cremer, R. (2015): Digging the meteosat treasure—3 decades of solar surface radiation. *Remote Sensing*, 7(6), 8067–8101.

Myers, W., Wiener, G., Linden, S., and Haupt, S. (2011): A consensus forecasting approach for improved turbine hub height wind speed predictions. *Proc. WindPower 2011*.

Müller, R., Behrendt, T., Hammer, A., and Kemper, A. (2012): A new algorithm for the satellite-based retrieval of solar surface irradiance in spectral bands. *Remote Sensing*, 4, 622–647.

Müller, R., Trentmann, J., Träger-Chatterjee, C., Posselt, R., and Stöckli, R. (2011): The role of the effective cloud albedo for climate monitoring and analysis. *Remote Sensing*, 3, 2305–2320.

Nikitidou, E., Zagouras, A., and Salamalikis, V.and Kazantzidis, A. (2019): Short-term cloudiness forecasting for solar energy purposes in greece, based on satellite-derived information. *Meteorology and Atmospheric Physics*, 131(2), 175–182.

Nonnenmacher, L. and Coimbra, C.F. (2014): Streamline-based method for intra-day solar forecasting through remote sensing. *Solar Energy*, 108, 447 – 459.

Ohmura, A., Dutton, E.G., Forgan, B., Fröhlich, C., Gilgen, H., Hegner, H., Heimo, A., König-Langlo, G., McArthur, B., Müller, G., et al. (1998): Baseline surface radiation network (bsrn/wcrp): New precision radiometry for climate research. *Bulletin of the American Meteorological Society*, 79(10), 2115–2136.

OpenCV (2020): Homepage of opencv. `http://opencv.org/`. Accessed: 2020-04-21.

Pachauri, R.K., Allen, M.R., Barros, V.R., Broome, J., Cramer, W., Christ, R., Church, J.A., Clarke, L., Dahe, Q., Dasgupta, P., et al. (2014): *Climate change 2014: synthesis report. Contribution of Working Groups I, II and III to the fifth assessment report of the Intergovernmental Panel on Climate Change*. IPCC.

Pereda, J.G. (2016): Algorithm theoretical basis document for the wind product processors of the nwc/geo. SAF-ATBD: NWC/CDOP2/GEO/AEMET/SCI/ATBD/Wind, NWC-SAF.

Perez, R., Kankiewicz, A., Schlemmer, J., Hemker, K., and Kivalov, S. (2014): A new operational solar resource forecast model service for pv fleet simulation. In *2014 IEEE 40th Photovoltaic Specialist Conference (PVSC)*, Seiten 0069–0074. IEEE.

Perez, R., Kivalov, S., Schlemmer, J., Hemker Jr, K., Renné, D., and Hoff, T.E. (2010): Validation of short and medium term operational solar radiation forecasts in the us. *Solar Energy*, 84(12), 2161–2172.

Perez, R., Lorenz, E., Pelland, S., Beauharnois, M., Van Knowe, G., Hemker Jr, K., Heinemann, D., Remund, J., Müller, S.C., Traunmüller, W., et al. (2013): Comparison of numerical weather prediction solar irradiance forecasts in the us, canada and europe. *Solar Energy*, 94, 305–326.

Peura, M. and Hohti, H. (2004): Optical flow in radar images. In *Proceedings of ERAD*, Volume 454.

Pfeifroth, U., Kothe, S., Müller, R., Trentmann, J., Hollmann, R., Fuchs, P., and Werscheck, M. (2017): Surface radiation data set–heliosat (sarah)–edition 2, satellite application facility on climate monitoring. `https://doi.org/10.5676/EUM_SAF_CM/SARAH/V002`. Accessed: 2020-07-22.

Pfeifroth, U., Sanchez-Lorenzo, A., Manara, V., Trentmann, J., and Hollmann, R. (2018): Trends and variability of surface solar radiation in europe based on surface-and satellite-based data records. *Journal of Geophysical Research: Atmospheres*, 123(3), 1735–1754.

Pinson, P. (2006): *Estimation of the uncertainty in wind power forecasting.* Dissertation, École Nationale Supérieure des Mines de Paris. `https://pastel.archives-ouvertes.fr/pastel-00002187`.

Raza, M.Q., Nadarajah, M., and Ekanayake, C. (2016): On recent advances in pv output power forecast. *Solar Energy*, 136, 125 – 144.

Rehman, S. and Mohandes, M. (2008): Artificial neural network estimation of global solar radiation using air temperature and relative humidity. *Energy Policy*, 36(2), 571–576.

Reinert, D., Prill, F., Frank, H., Denhard, M., and Zängl, G. (2018): Database reference manual for icon and icon-eps. *Version*, 1(4), 35.

Remund, J., Perez, R., and Lorenz, E. (2008): Comparison of solar radiation forecasts for the usa. In *Proc. of the 23rd European PV Conference*, Volume 14. Valencia, Spain.

Richard Müller, J.T. (2014): *Algorithm Theoretical Baseline Document Meteosat Solar Surface Radiation and effective Cloud Albedo Climate Data Records – Heliosat SARAH The MAGICSOL method applied for the generation of SARAH.* CM SAF. `https://www.cmsaf.eu/SharedDocs/Literatur/document/2014/saf_cm_dwd_atbd_meteosat_hel_1_3_pdf.html`.

Rosenow, R., Güldner, J., and Spänkuch, D. (2001): The satellite weather of the german weather service – an assimilation procedure with a spectral component. Volume EUM P 33 of *Proceedings of the 2001 EUMETSAT Met. Data User's Conf.*, Seiten 541–545. EUMETSA,Darmstadt.

Sánchez, J., Meinhardt-Llopis, E., and Facciolo, G. (2012): Tv-l1 optical flow estimation.

Sanfilippo, A., Martin-Pomares, L., Mohandes, N., Perez-Astudillo, D., and Bachour, D. (2016): An adaptive multi-modeling approach to solar nowcasting. *Solar Energy*, 125, 77–85.

Schmetz, J., Holmlund, K., Hoffman, J., Strauss, B., Mason, B., Gaertner, V., Koch, A., and Berg, L.V.D. (1993): Operational cloud-motion winds from meteosat infrared images. *Journal of Applied Meteorology*, 32(7), 1206–1225.

Schroedter-Homscheidt, M. and Gesell, G. (2016): Verification of sectoral cloud motion based direct normal irradiance nowcasting from satellite imagery. In *AIP Conference Proceedings*, Volume 1734, Seite 150007. AIP Publishing.

Sengupta, M., Habte, A., Kurtz, S., Dobos, A., Wilbert, S., Lorenz, E., Stoffel, T., Renné, D., Gueymard, C.A., Myers, D., et al. (2015): Best practices handbook for the collection and use of solar resource data for solar energy applications, chapter 7: Forecasting solar radiation.

Sfetsos, A. and Coonick, A. (2000): Univariate and multivariate forecasting of hourly solar radiation with artificial intelligence techniques. *Solar Energy*, 68(2), 169–178.

Simonenko, E., Chudin, A.O., and Davidenko, A. (2017): The differential method for calculation of cloud motion vectors. *Russian Meteorology and Hydrology*, 42(3), 159–167.

Sirch, T., Bugliaro, L., Zinner, T., Möhrlein, M., and Vazquez-Navarro, M. (2017): Cloud and dni nowcasting with msg/seviri for the optimized operation of concentrating solar power plants. *Atmos. Meas. Tech.*, 10, 409–429.

Sonka, M., Hlavac, V., and Roger, B. (2014): *Image Processing, Analysis, and Machine Vision, International Edition*. ISBN-13-978-1-133-59360-7. CENGAGE Learning.

Tascikaraoglu, A. and Uzunoglu, M. (2014): A review of combined approaches for prediction of short-term wind speed and power. *Renewable and Sustainable Energy Reviews*, 34, 243–254.

Trentmann, J. (2014): *Meteosat Solar Surface Irradiance and effective Cloud Albedo Climate Data records METEOSAT HEL The SARAH climate data records*. CM SAF. `https://www.cmsaf.eu/SharedDocs/Literatur/document/2014/saf_cm_dwd_pum_meteosat_hel_1_1_pdf.html`.

Tuohy, A., Zack, J., Haupt, S.E., Sharp, J., Ahlstrom, M., Dise, S., Grimit, E., Mohrlen, C., Lange, M., Casado, M.G., et al. (2015): Solar forecasting: methods, challenges, and performance. *IEEE Power and Energy Magazine*, 13(6), 50–59.

Turner, B., Zawadzki, I., and Germann, U. (2004): Predictability of precipitation from continental radar images. part iii: Operational nowcasting implementation (maple). *Journal of Applied Meteorology*, 43(2), 231–248.

Urbich, I., Bendix, J., and Müller, R. (2018): A novel approach for the short-term forecast of the effective cloud albedo. *Remote Sensing*, 10(6), 955.

Urbich, I., Bendix, J., and Müller, R. (2019): The seamless solar radiation (sesora) forecast for solar surface irradiance—method and validation. *Remote Sensing*, 11(21), 2576.

Velden, C.S., Olander, T.L., and Wanzong, S. (1998): The impact of multispectral goes-8 wind information on atlantic tropical cyclone track forecasts in 1995. part i: Dataset methodology, description, and case analysis. *Monthly Weather Review*, 126(5), 1202–1218.

Voyant, C., Notton, G., Kalogirou, S., Nivet, M.L., Paoli, C., Motte, F., and Fouilloy, A. (2017): Machine learning methods for solar radiation forecasting: A review. *Renewable Energy*, 105, 569 – 582.

Vrettos, E. and Gehbauer, C. (2019): A hybrid approach for short-term pv power forecasting in predictive control applications. In *2019 IEEE Milan PowerTech*, Seiten 1–6. IEEE.

Wolff, B. (2017): *Support vector regression for solar power prediction.* Dissertation, Carl von Ossietzky Universität Oldenburg.

Wolff, B., Kühnert, J., Lorenz, E., Kramer, O., and Heinemann, D. (2016): Comparing support vector regression for pv power forecasting to a physical modeling approach using measurement, numerical weather prediction, and cloud motion data. *Solar Energy*, 135, 197 – 208.

Yang, D., Wu, E., and Kleissl, J. (2019): Operational solar forecasting for the real-time market. *International Journal of Forecasting*, 35(4), 1499–1519.

Zach, C., Pock, T., and Bischof, H. (2007): A duality based approach for realtime tv-l1 optical flow. *Pattern Recognition*, Seiten 214–223.

Zhang, G. and Chanson, H. (2018): Application of local optical flow methods to high-velocity free-surface flows: Validation and application to stepped chutes. *Experimental Thermal and Fluid Science*, 90, 186–199.

Zinner, T., Forster, C., de Coning, E., and Betz, H.D. (2013): Validation of the meteosat storm detection and nowcasting system cb-tram with lightning network data – europe and south africa. *Atmospheric Measurements Techniques*, 6, 1567–1583.

Zinner, T., Mannstein, H., and Tafferner, A. (2008): Cb-tram: Tracking and monitoring severe convection from onset over rapid development to mature phase using multiple-channel meteosat-8 seviri data. *Meteorology and Atmospheric Physics*, 101, 191–210.

Acknowledgements

Without the constant support of several people this work would not have been possible. First of all I would like to thank Dr. Richard Müller who encouraged me to write this thesis and Prof. Dr. Jörg Bendix for supervising it. I am very grateful for the support and feedback of both of them as well as for some fruitful discussions which always brought some new perspective.

This work was developed in the frame of the research project Gridcast at the DWD which was funded by the BMWi. I am thankful for the funding of my publications and for the exchange with all of my colleagues. A special thanks goes to Christine Sgoff for proof reading this work.

I also want to thank Dr. Uwe Pfeifroth and Dr. Jörg Trentmann for providing the reference data for my work. Thanks to Dr. Manuel Werner, Nils Rathmann and Michael Mott for helping me regarding the implementation of my code into the POLARA framework.

Finally, I would like to thank my parents and my boyfriend. They supported my decision of writing this thesis from the beginning and they never stopped encouraging me. I am so grateful for their endless patience and understanding particularly in challenging phases.

Eidesstattliche Erklärung

Hiermit versichere ich, dass ich meine vorliegende Dissertation

Development of a short-term forecast system for solar surface irradiance based on satellite imagery and NWP data

selbstständig, ohne unerlaubte Hilfe Dritter angefertigt und andere als die in der Dissertation angegebenen Hilfsmittel nicht benutzt habe.

Alle Stellen, die wörtlich oder sinngemäß aus veröffentlichten oder unveröffentlichten Schriften entnommen sind, habe ich als solche kenntlich gemacht. Dritte waren an der inhaltlich-materiellen Erstellung der Dissertation nicht beteiligt; insbesondere habe ich hierfür nicht die Hilfe eines Promotionsberaters in Anspruch genommen.

Kein Teil meiner Dissertation wurde und wird in keinem anderen Promotions- oder Habilitationsverfahren verwendet und hat noch keinen sonstigen Prüfungszwecken gedient.

Mit dem Einsatz von Software zur Erkennung von Plagiaten bin ich einverstanden.

Unterschrift:

Ort, Datum:
